N˚d'ordre : 42391

UNIVERSITÉ LILLE - SCIENCES ET TECHNOLOGIES

École Doctorale :

Sciences de la Matière, du Rayonnement et de l'Environnement

THÈSE DE DOCTORAT

présentée en vue d'obtenir le titre de

DOCTEUR EN PHYSIQUE DE L'UNIVERSITÉ LILLE

Mention :

PHYSICO-CHIMIE, ATMOSPHÈRE

Molecular Modeling of Aerosols

par

Josip Lovrić

Thèse dirigée par Stéphane Briquez et Denis Duflot

préparée au

Laboratoire de Physique des Lasers, Atomes et Molécules

Date de soutenance le 16 Juin 2017

Jury :

Présidente du jury: Thérèse Huet, Professeur - Université de Lille

Rapporteurs: Jan Pettersson, Professeur - University of Gothenburg

Sylvain Picaud, Directeur de Recherches CNRS – Université de France- Comté

Examinatrice : Sophie Sobanska, Chargée de Recherches CNRS – Université de Bordeaux

Directeur *de thèse*: Stéphane Briquez, Maître de Conférences HDR - Université de Lille

Co-directeur *de thèse:* Denis Duflot, Maître de Conférences HDR - Université de Lille

Invité : Celine Toubin, Maître de Conférences HDR - Université de Lille

"God made the bulk; surfaces were invented by the devil."

Wolfgang Pauli

"Kick in the ass is still step forward."

Anonymous

"I am always doing what I cannot do yet, in order to learn how to do it"

Vincent Van Gogh

"Kasno je, sjećanja, uzalud se javljate, beskorisne su vaše nemoćne utjehe i podsjećanja na ono što je moglo da bude, jer što nije bilo, nije ni moglo da bude. A uvijek izgleda lijepo ono što se nije ostvarilo."

Meša Selimović

UNIVERSITE DE LILLE

Abstract

Universite de Lille
Laboratory PhLAM

Doctor of Physics

Molecular Modeling of Aerosols

by Josip LOVRIC

In this thesis numerical methods are used to study the properties, described at the molecular level, of organic aerosols, especially marine aerosols, and their interaction with species in the atmosphere. The organisation of the organic matter in these aerosols plays a key role for their optical, chemical properties, and their ability to act as a cloud condensation nuclei.

The first part reviews atmospheric context and the methods (classical molecular dynamics and hybrid quantum/classical approaches) used in this thesis. Then applications to three cases are detailed.

Firstly, the organization, more particularly the orientation, of palmitic acid molecules adsorbed on a salt (NaCl) surface as a function of the fatty acid coverage and temperature has been studied using classical molecular dynamics (Gromacs package). The impact of the humidity on the structuration of this organic coating has been described in details, showing the existence of structured fatty acid island-like monolayers on NaCl surface.

In a second study, the reactivity of NO_2 with these heterogeneous marine aerosols has been investigated by a hybrid quantum/classical method (CP2K package), with taking into account the effect of the humidity.

The last study is a classical molecular dynamics of n-butanol crystal, water accommodation at these surfaces and simulation of water jet collision with n-butanol surface. These simulations, complementary to experiments, were performed to better understand the fundamental role of the water-organic matter interaction on the properties of the aerosols and clouds.

Acknowledgements

Hereby I am pleased first to give special thanks to my beloved wife and her never ending support. Before I started my PhD many people told me that supervisors will be the most important persons in my life and indeed my supervisors played that role very good. Stephane, Denis and Celine were always present for me when I needed something no matter it was personal or professional. Big thanks to all members of PCMT team, Valerie and Florent for making our cluster running, thanks to Daniel for interesting discussions and everyday companionship. Special thanks to Eric, we helped each other working together and thank you for often being a French teacher to me.

Contents

List of Figures

List of Tables

List of Abbreviations

OA	**O**rganic **A**erosol
PBL	**P**lanetary **B**oundary **L**ayer
CCN	**C**loud **C**ondesation **N**uclei
WHO	**W**orld **H**ealth **O**rganization
VOC	**V**olatile **O**rganic **C**ompounds
DMS	**D**i**M**ethyl **S**ulfide
POA	**P**rimary **O**rganic **A**erosols
SOA	**S**econdary **O**rganic **A**erosols
FA	**F**atty **A**cids
SSA	**S**ea **S**alt **A**erosols
RH	**R**elative **H**umidity
PA	**P**almitic **A**cid
QM/MM	**Q**uantum **M**echanical/**M**olecular **M**echanics
MD	**M**olecular **D**ynamics
AIMD	**A**b **I**nitio **M**olecular **D**ynamics
RDF	**R**adial **D**istribution **F**unction
LJ	**L**ennard-**J**ones
OPLS	**O**ptimized **P**arameters for **L**iquid **S**imulation
PBC	**P**eriodic **B**oundary **C**onditions
PME	**P**article **M**esh **E**wald
BO	**B**orn-**O**ppenheimer
DFT	**D**ensity **F**unctional **T**heory
SAM	**S**elf **A**ssembled **M**onolayer
TM	**T**heoretical **M**onolayer
AFM	**A**tomic **F**orce **M**icroscope
EMB	**E**nvironmental **M**olecular **B**eam

Dedicated to my family and friends. My mother and father who supported me through all the years of my education. Endless gratitude to my brother who always supported me and more important helped me to build my character and moral standards. To my wife, without her support I would not be here. My sons, three musketeers (Filip, Mihael, Natanael) also arrived in my life during my entrance in scientific life. Although they gave me sleepless night and been doing god job to attract my attention all this would not be a half fun as with them.

Chapter 1

Introduction

Atmospheric aerosol particles are fundamental constituents of the Earth's atmosphere as they influence the Earth's energy budget and can strongly impact the human health. During the last decade, a huge effort has been done to characterize the effects of these aerosols on climate particularly. Among these aerosols, the organic aerosol (OA) components account for a large fraction of atmospheric particulate matter. Our present understanding of OA physical and chemical properties and transformation is limited, and the estimates of their environmental effects are quite uncertain. The purpose of this thesis was to contribute to the understanding of these mechanisms at the molecular level using numerical methods such as classical molecular dynamics or quantum mechanics/molecular mechanics to model organic aerosols and their properties. This research was supported by the French Laboratory of Excellence CaPPA (Chemical and Physical Properties of the Atmosphere, Programme d'Investissement d'Avenir) and the "Hauts de France" Region. The CaPPA project gathers 7 laboratories to run multidisciplinary research activities in the fields of aerosols properties (www.labex-cappa.fr). This thesis was part of the workpackage 2 (the CaPPA project is organized in 6 workpackages) "Aerosol microphysical, chemical and optical properties from fundamental heterogeneous processes to remote sensing".

In this chaper, I will briefly describe the general properties of the Earth's atmosphere, and emphasize the role of the organic aerosols, and more particularly of the organic marine aerosols.

1.1 Atmosphere

1.1.1 Evolution of the Earth's atmosphere

4.6 billion years ago, the solar system was born from the primordial solar nebula, an interstellar aggregate of gas and dust [1]. Gravitational interactions gave rise to a solid planet by aggregation. The primordial atmosphere on Earth was created with released high volatile compounds such as CO_2, N_2, H_2O and H_2 from volcanic emissions 4.4 billion years ago [1]. The gravitational interactions trapped molecules close to the surface and induced a heterogeneous particle density distribution, leading to a relatively thin gas layer above the surface. From the chemistry point of view, the primordial atmosphere was reductive while present atmosphere is oxidizing. Carbon compounds dissolved, on a long scale time, into the ocean to from carbonate rocks. N_2, being chemically inert, non soluble in water and incondensable, accumulated in the atmosphere and became the most abundant

constituent of the atmosphere. The dramatic increase in oxygen happened about 2.3 billion years ago [2] (Fig 1.1). The scientific community agrees that the origin of this sudden increase could be due to bacteria capable of oxygenic photosynthesis. Today, about 99% of the present atmosphere consists of N_2 (78%), O_2 (21 %) and Ar (1%). The oxygen level is maintained in balance through photosynthesis. Water vapour is the next most abundant and mainly founded in lower troposphere. Trace gases represent less than 1% of the atmosphere but they play an important role in the radiative balance of Earth [1]. For example, it is now well established that the increasing concentration of CO_2 during the last decades is responsible for the climate changes [3].

1.1.2 Chemical composition and physical properties of the present atmosphere

Anaximenes (585–528 BC), a greek philosopher, had suggested that air was the primary substance and the source of all other things. Then, according to Empedocles (ca. 490–430 BC), air was considered as one of the four elements [4]. This conception did not evolve until the 18th century. Indeed the first experimental studies about atmospheric composition were performed in the 1700s, as can be seen in Table 1.1 and 1.2 summarizing the major discoveries in the chemical compositions of air.

TABLE 1.1: List of major chemical discoveries on air composition [5].

Date	Compound	Scientist
1750s	carbon dioxide	Joseph Black
1766	hydrogen	Henry Cavendish
1772	nitrogen	Daniel Rutherford
1774	oxygen	Joseph Priestley and
1772 (published in 1777)		Carl Wilhelm Scheele
1840	ozone	Christian Friedrich Schönbein
1894	argon	Lord Rayleigh and William Ramsay

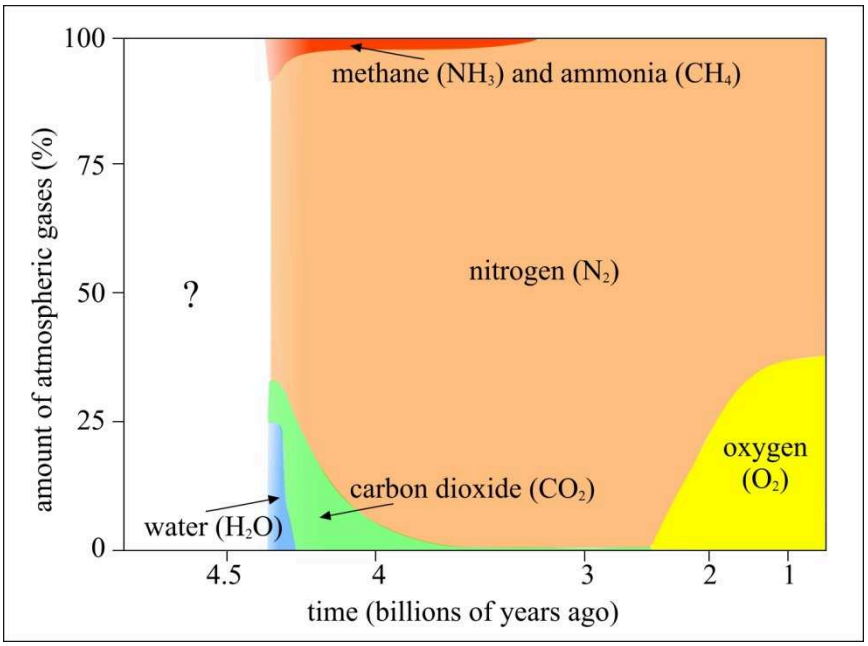

FIGURE 1.1: Evolution of atmospheric chemical composition [5].

TABLE 1.2: List of major achievements in modern atmospheric chemistry [5].

Date	Explorer(s)	Discovery
1924	Gordon Dobson	developed a spectrophotometer and started the regular measurements of total-column ozone
1930	Sydney Chapman	described theory that explains existence of the ozone "layer"
1960	Arie Jan Haagen-Smit	described the emergence of the photochemical smog
1973	James Lovelock	first detected CFC's (Chlorofluorocarbons) in the atmosphere
1995	Paul Crutzen, Mario Molina and Frank Sherwood Rowland	the Nobel Prize in Chemistry was awarded jointly "for their work in atmospheric chemistry, particularly concerning the formation and decomposition of ozone".

The mass of the atmosphere is approximately $5.3{\cdot}10^{18}$ kg, which is a few orders of magnitude lower than the $1.4{\cdot}10^{21}$ kg of the hydrosphere (oceans, sees, lakes, rivers, groundwater, snow and ice) and of the $5.98{\cdot}10^{24}$ kg of the Earth. The large atmospheric mass is pulled toward the Earth due to the gravity. Subsequently, the density of the atmosphere rapidly decreases with the distance from the surface. Atmosphere can be seen as a countless

number of atoms and molecules rapidly moving in a chaotic way. The mean free path of these particles is 10^{-8} m close to the surface whereas at 80 km it increases to 10^{-2} m.

The vertical structure of the atmosphere can be described either by its homogeneity or its physical properties, based mostly upon temperature and pressure evolution with height. By considering its homogeneity, the atmosphere can be divided in two layers (Fig. 1.2 a). First, close to the surface, due to turbulent fluxes and constant mixing, the atmosphere appears homogeneous regarding chemical species with long mean residence times. This first layer is called homosphere. Above it, a thin layer called turbopause, at 80 km from the earth surface, separates the homosphere from the heterosphere where the molecular diffusion is important and the atmosphere stratification is mostly driven by molecular mass.

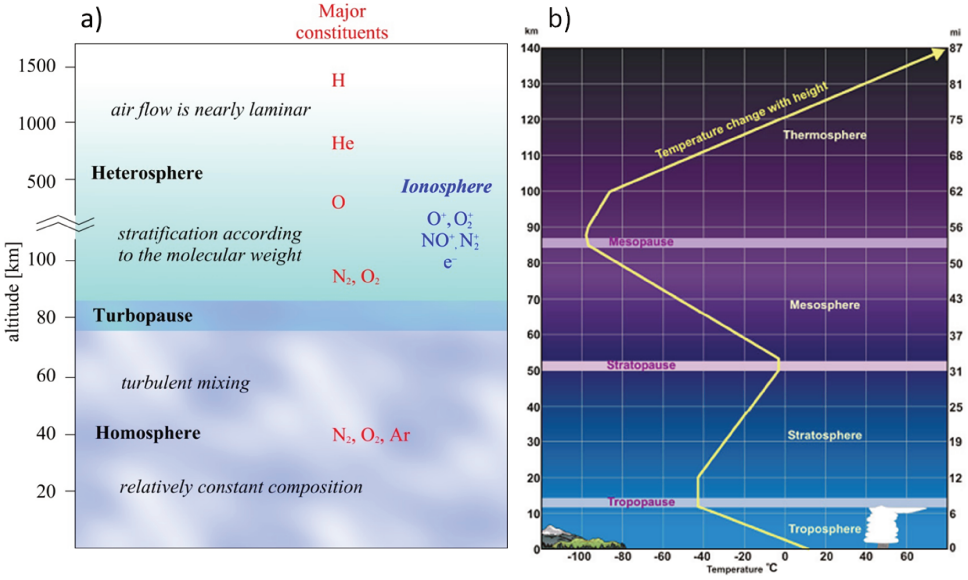

FIGURE 1.2: Atmosphere structure, on the left based on chemical composition and on right on temperature evolution [5].

Considering the evolution of the temperature in the atmosphere (Fig. 1.2 b), the first layer close to surface is called troposphere. Clouds formation and most of the chemistry takes place in the troposphere, making it of special interest. The thickness of the troposphere is around 11-12 km, thicker in the equator region (up to 18 km) and thinner in the polar areas (down to 7 km). More than 80% of the atmosphere mass is located in the troposphere, including all the water vapor and nearly all aerosols. The Earth surface is warmed by solar radiations and consequently the troposphere is heated from the ground. Thereby the temperature is decreasing with altitude, leading to turbulent mixing. This drives water vapour and other particles vertical transfer. The typical range of temperature for the troposphere is from $20°C$ close to the surface down to $-60°C$ near stratosphere.

Above troposphere, the next layer is called stratosphere, spanning between 10 km and 50 km. The stratosphere is marked by a temperature inversion up to 50 km altitude, where the temperature increases to about

0°C on the top of the stratosphere. This inversion is a consequence of high concentration of ozone, in the ozone layer at 25 km, which is an efficient absorbent of UV radiations. The last two layers of atmosphere are called mesosphere and thermosphere. These two layers, less studied than the previous mentioned layers, are sparse and contain mostly light elements such as H and He. The thermosphere is the part of atmosphere where aurora borealis take place.

The bottom layer of troposphere is called Planetary Boundary Layer (PBL). The structure and depth of PBL vary a lot with seasons, weather conditions and time of day. The lowest (about 10%) part of PBL is called surface layer. The thickness of this layer is typically 10–30 m at night, and 50–100 m in day-time. The PBL is the place where exchanges between surface (sources and sinks of aerosols) and the atmosphere take place, due to the turbulent fluxes of heat, water and air pollutants. The PBL has a great impact on the dispersion, dilution and deposition of air pollutants.

Gases concentration in the present atmosphere are shown on Table 1.3. There are different ways to express the quantities of gases or particles in the atmosphere: the concentration ($kg \cdot m^{-3}$), the volume ratio (m^3 gas per m^3 air) or mole fraction ($mol \cdot mol^{-1}$). For trace gases, the mixing ratio is given in parts per million volume ($ppmv$) (billion ($ppbv$) or trillion ($pptv$)).

TABLE 1.3: Atmosphere chemical composition [6].

Gas		Volume[(a)]	
Name	Formula	in ppmv[(b)]	in %
Nitrogen	N_2	780 840	78.084
Oxygen	O_2	209 460	20.946
Argon	Ar	9 340	0.934
Carbon dioxide	CO_2	400	0.04
Neon	Ne	18.18	0.00182
Helium	He	5.24	0.00052
Methane	CH_4	1.79	0.00018
Water vapor[(c)]	H_2O	10–50[(d)]	0.001–5[(d)]

Notes:
(a) volume fraction is equal to mole fraction for ideal gas
(b) ppmv: parts per million by volume
(c) Water vapor is about 0.25% by mass over full atmosphere
(d) Water vapor concentration strongly varies locally

1.2 Aerosols

1.2.1 Physical and chemical properties of aerosols

Aerosols are small solid or liquid particles suspended in the atmosphere with a diameter ranging from a few nm up to the tens of μm. It is well

known that they are one of the most important factors affecting both, natural climate processes and anthropogenic climate changes [3, 7]. Aerosols have an impact on the radiative balance directly by scattering and absorbing terrestrial and solar radiations and indirectly by acting as cloud condensation nuclei (CCN). Nowadays, special attention is paid to the health effects, namely respiratory and cardiovascular problems [8, 9]. According to the World Health Organization (WHO), particle pollution contributes to approximately 7 million premature deaths each year, making it one of the leading causes of mortality [10]. Aerosols can be classified and quantified according to their concentration, size, physical or chemical composition or their origin. Aerosols sources are diverse, and can be from natural or anthropogenic origins. Natural aerosols dominate by number and concentration, and can be estimated to 13-14000 Tg. yr^{-1} (see Table 1.4), while the total anthropogenic contribution is, on the best estimation, 460 Tg. yr^{-1} [11]. Natural aerosols, from biogenic sources, dust or sea-salt are known as a large part of uncertainty in present day aerosol forcing, the response of the climate system to anthropogenic aerosol perturbations depending strongly on the natural aerosol background [3, 12, 13, 14] (Fig. 1.5). The main sources of anthropogenic aerosols are fossil fuel combustion (transport, heating) or biomass burning. Even a small concentration of anthropogenic aerosols can cause significant changes in the properties of the atmosphere, not only by direct influence on radiations but also through interactions with other aerosols [12, 15]. The concentration, size distribution and composition of atmospheric aerosol particles vary significantly with time and space. In the lower troposphere, the aerosol mass concentration is in a range of 1-100 $\mu g.m^{-3}$, and particles number typically varies from 10^2 to $10^5 cm^{-3}$ [16]. Deserts and urban areas are rich in aerosols, while polar atmosphere and alpine air contains fewer aerosols. Aerosols concentration also decreases with altitude. Fig. 1.4 represents the aerosols distribution according to different physical characteristics. Particle size is an important parameter which affects their lifetime, physical and chemical properties. Particles in nucleation mode with size reaching 10's of nm are of particular interest in this thesis, since classical molecular dynamics, the main tool used in this thesis, allows us to study systems of this size. Fig. 1.3 is a schematic representation of the aerosol life cycle. In this thesis, we are especially interested in secondary aerosols formation and aggregation mode. Once primary aerosols, either natural or anthropogenic, are released in the atmosphere, they exhibit some physical and chemical changes. One of the typical example is water condensation on aerosol nuclei. In the same way, if we expose organic aerosols to air and sun light, oxidation processes will occur, and thereby optical properties and condensation potential will change as well. Finally, aerosols have their typical life time. In the range of hours to months, aerosols are submitted to wet or dry deposition, which are the main types of removing processes of aerosol particles.

Aerosols are important players in the complicated climate system. It is therefore necessary for the scientific community to understand all the chemical and physical processes related to the aerosols in the atmosphere. One of the first steps is to understand aerosols formation. Despite extensive research, there are still open questions, especially regarding aerosols creation in the nucleation mode. But also topics such as the role of aerosols as CCN, the interaction of the aerosols with water, the influence of organic matter

present in aerosols on water accommodation and reactivity are more and more in the focus of the scientific community. Hygroscopic properties of aerosols are indeed of special interest due to their direct link with precipitations. In order to describe these phenomena, different models based on equilibrium thermodynamics have been developed, such as Kohler theory which efficiently describes the hygroscopic growth of soluble particles in humid air [17]. This theory incorporates Kelvin effect, which models saturation vapor pressure variation due to a curved surface, and Raoult's Law, which relates the vapor pressure to the solute concentration. But a more detailed description, i.e. at the atomic level, is required to correctly assess the hygroscopic properties of aerosols. Aerosols represent a large quantity of solid or aqueous surfaces, enhancing heterogeneous chemistry. Chemical processes at the surface of these aerosols drive the concentration of traces gases and then directly influence air quality. For example, it is known that NOx species, pollutants due to combustion processes, are precursors of tropospheric ozone, which affects health and leads to reduced crop and forest yields[18]. But aerosols containing NaCl can serve as NOx sinks [19], leading to a reduction of the ozone concentration.

The present thesis deals with part of these questions, with a special attention paid to humidity effects. More specifically, we have focused on the interaction of water with fatty acids and butanol.

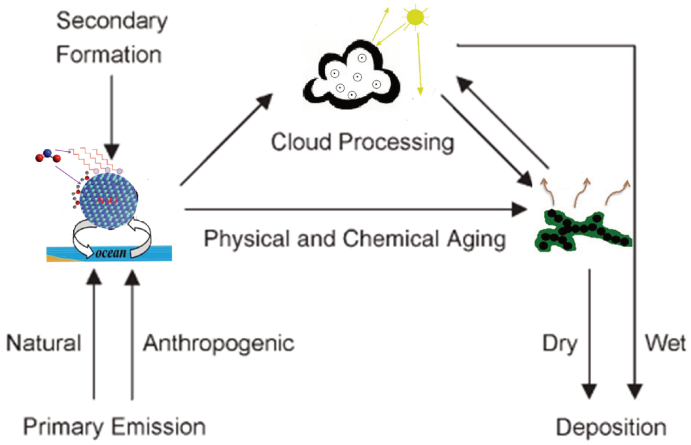

FIGURE 1.3: Schematic representation of aerosols life cycle, sources and aerosols formation to deposition.

Natural particles	Annual global emission flux (Tg· yr^{-1})
Sea salt (total, sizes <16 μm)	3344 [6]
Sea salt (sizes <1 μm)	54 [6])
Sea salt (1−16 μm size range)	3290 [6]
Sea salt (overall)	10 100 [20], 3300 [21], 7804 [22], ranging from 3000 to 20 000 Tg y^{-1} [23]
Mineral (soil) dust (total, sizes <20 μm)	2150 [6]

Mineral (soil) dust (sizes <1 μm)	110 [6]
Mineral (soil) dust total (1−2 μm size range)	290 [6]
Mineral (soil) dust total (2−20 μm size range)	1750 [6]
Mineral dust (0.1−10 μm size)	1000−2150 (average = 1490) [24]
Mineral dust (overall)	2000 [21], 1704 [22], ranging from 1000 to 2150 Tg. y^{-1} [23]
Volcanic dust (coarse particles only)	30 [1]
Sulfates from volcanic SO_2	10 [25]
Volcanic sulfates (as $NH_4\ HSO_4$)	21 [6]
Volcanic SO_2	9.2 [22]
Cosmic dust in the upper mesosphere	3×10^{-2} to 1.1×10^{-1} [26]
Cosmic dust in the middle atmosphere	2×10^{-3} to 2×10^{-2} [26], 1.5×10^{-4} to 4×10^{-2}[27]
Biogenic aerosols	1000 [21]
Biogenic sulfate (as NH_4HSO_4)	57 [6]
Biogenic carbonaceous aerosols (sizes > 1 μm)	56 [6]
Biogenic primary organic aerosols	15−70 [23]
Biogenic Volatile organic compounds (VOC) compounds	16 [6]
Secondary organic aerosols from biogenic VOC	11.2 [28]
Secondary organic aerosols	2.5−83 [23]
Sulfates (from all the natural primary and secondary sources)	107−374 [23]
Nitrates (overall, from natural primary and secondary sources)	12−27 [23]
Secondary sulfates from dimethyl sulfide (DMS)	12.4 [29], 18.5 [22]
Carbonaceous aerosols from biomass burning (sizes < 2 μm)	54 [6]
Primary organic aerosols	44.4 [22]
Biomass burning organic	26−70 [23]
Total natural particles over the whole size range	5875 [6] 4200−22 800 [23], including the United Nations (1979) estimate of volcanic debris

TABLE 1.4: Estimates of the annual emission fluxes (measured in teragram per year (1 Tg. yr^{-1} = 10^6 ton. yr^{-1})) of natural aerosols from various sources, as found in the literature over the past 15 years [30].

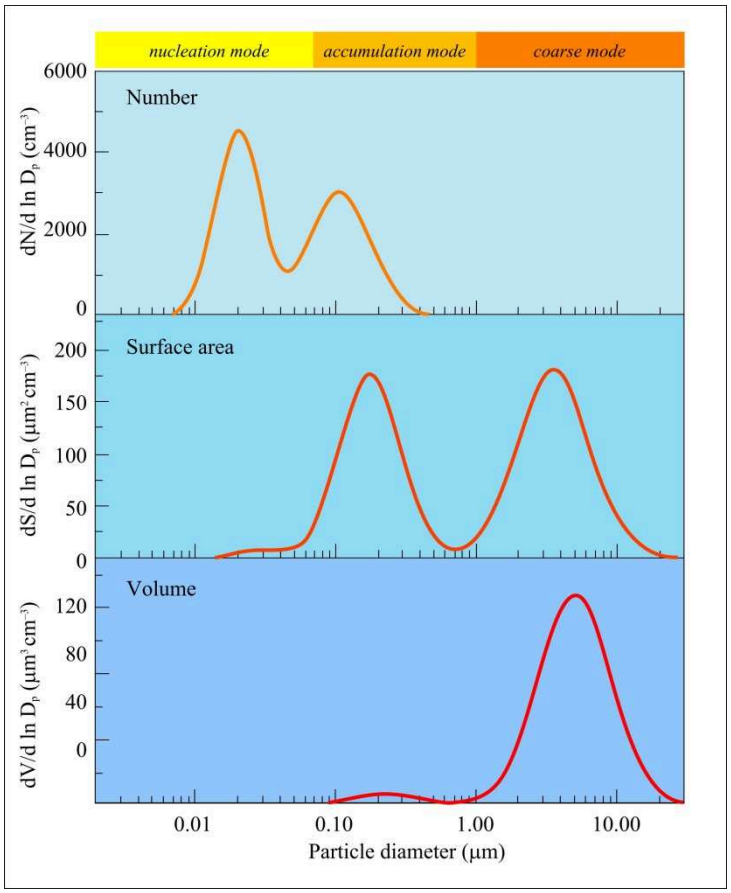

FIGURE 1.4: Distribution of aerosols by number, surface and volume. Surface area under curve represents total number of aerosols [5]

1.2.2 Organic marine aerosols

Primary aerosols are emitted mostly from the sea (1000 – 6000 Tg/year), big dry lands (deserts) (1000 – 3000 Tg/year) and from combustion processes of anthropogenic or biogenic origin (66 – 217 Tg/year) [6]. The organic fraction comprises dissolved and particulate organic matter: lipids, amino and fatty acids, mono and poly-saccharides, humic substances and phytoplankton cell fragments. Their spatial distribution varies with location and season [12, 31, 32]. Once primary organic marine aerosols (POA) (emission of 105 Tg/year) [12] are released in the atmosphere, they form heterogeneous organic compounds which can then undergo transformations and give rise to secondary organic aerosols (SOA). Mixing state, hygroscopicity, cloud droplet activation potential and atmospheric ageing of marine POA remain poorly quantified. Studies have found that marine POA can cause large local increases in the cloud condensation nuclei concentration

and have a non-negligible influence on the assessment of the anthropogenic aerosol forcing of climate [12].
In the last decades, field measurements [12] and experimental investigations in laboratory, have revealed that oceans represent an important source of organic matter. Even if the organic mass in total aerosol mass can be small [19, 33, 34], the [Fatty Acids (FA)]/[sea salt] ratio in autumn, winter, spring and summer seasons being 1.8 ($\pm$1.3) x 10^{-4}, 2.1 ($\pm$1.3) x 10^{-4}, 3.7 ($\pm$2.9) x 10^{-4}, and 4.6 ($\pm$1.8) x 10^{-4}, respectively [35], the organic part actually influences strongly the optical and aggregation properties through structural organization such as creation of surface self-assembled layers. Moreover, organic matter can undergo different physical and chemical processes in the atmosphere, leading to dramatic changes of the hygroscopic properties. For instance, McNeill and co-workers [36] observed that oxidation of oleic acid decreases the CCN activity of the aerosols. Organic molecules present in the aerosols are typically polycarbonate chains (polysaccharides, carboxylic acids, etc...). The carbon chain size and the interaction with ions, which governs the molecular organization in/on the aerosols, are particularly important but have not yet been fully revealed. These heterogeneous and complex particles represent challenging cases of study for theoreticians.
Marine aerosols, which are dominated by sea salt aerosols (SSA), are among the most important sources of natural aerosols and participate to the global aerosol mass with more than 50% [37]. Pure SSA, and their physical properties, namely hygroscopicity and optical properties have been extensively studied [19, 34, 38]. But SSA are not pure crystals but rather mixtures of inorganic species like K^+, Mg^{2+}, Ca^{2+}, SO_4^{2+} ions and organic matter. Indeed, the composition of the marine aerosols is very diverse and depends on the location, time of the year, local weather conditions, etc. [32, 35]. The composition of nanometers sized (i.e. nucleation mode) sea spray particles is difficult to experimentally monitor due to the small size [39, 40]. They are often described as purely organic or purely sea-salt, while it is a mixture of both [41]. Typical organic molecules are fatty acids, polysaccharides and other hydrocarbons molecules. Although the sources of fatty acids can be terrestrial or from some anthropogenic activities like combustion processes, cooking [42], marine areas represent the most important source [35]. The process of creation of organically doped SSA has been studied both through experimental studies [34] and theoretical modeling [43]. Once created, aerosols evolve in the atmosphere, either continue aggregation with organic and inorganic species or undergo reactive processes with radicals (NO_x, O_3, HCl, Cl,...). The interaction of these aerosols with biogenic or anthropogenic species in the atmosphere is influenced by this organic coating. The accommodation coefficients (adsorbed fraction of incoming molecules), which are included in global models, are highly dependent on the aerosols composition and structuralization. A better molecular understanding of marine aerosol can then help to reduce uncertainties connected with SOA impact on radiative balance (Fig. 1.5), for example hygroscopic properties of aerosols aged in polluted environment can be estimated. It is expected that new ship routes will be opened in the Arctic region due to the ice melting. An understanding of organic doped marine aerosol at the molecular level could give prediction how this source of pollutants would impact this fragile and isolated ecosystem. Fig. 1.5 represents the results

from the IPCC effort in which they collect data and estimate the influence of human activities on radiative forcing according to pre-industrial era. It is important to notice the large uncertainties bars connected to these radiative forcing especially for the case of aerosols and precursors. Subsequently, getting more informations about the properties of these aerosols and their properties is very important. This was also one of the motivations for my thesis.

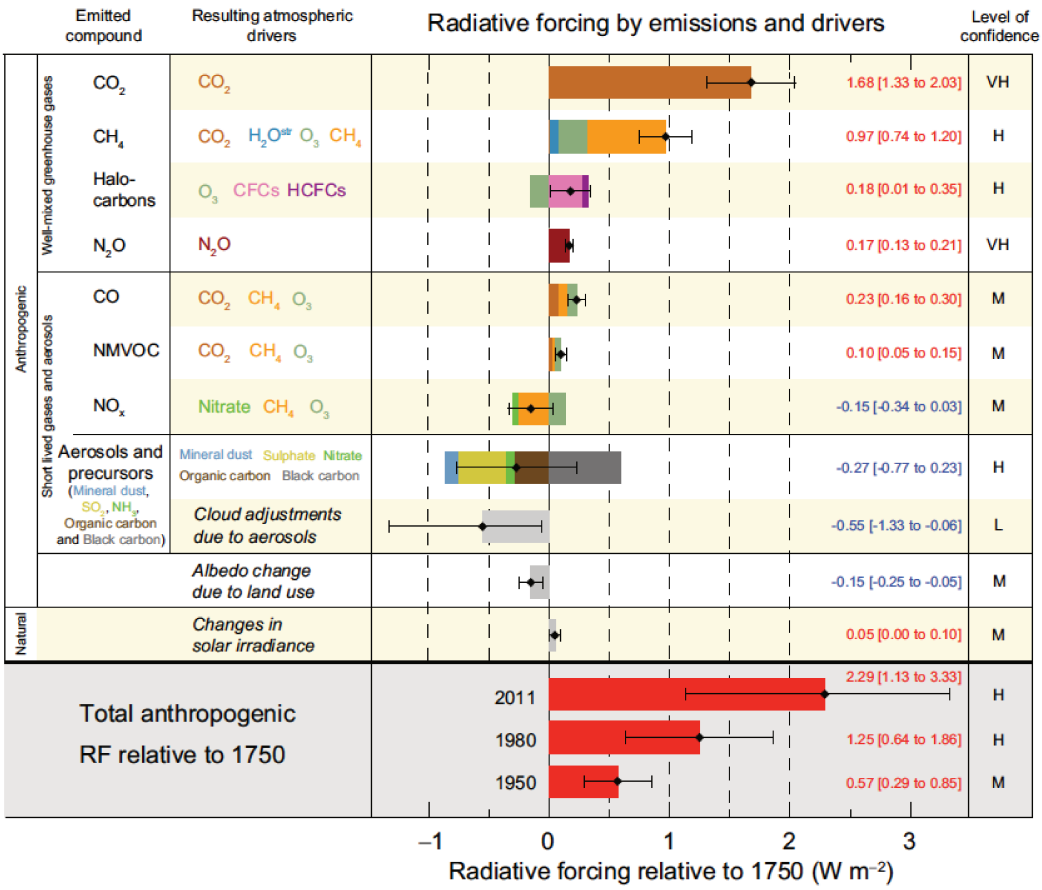

FIGURE 1.5: Radiative forcing relative to 1750 for different components and associated uncertainties [3]

Figure 1.6 illustrates processes leading to organic marine aerosols creation. We can divide this process in two stages: firstly, the bubble film breaks, releasing drops in the atmosphere, and a jet drop of ocean water is produced. All these processes are happening at the organic enriched surface layer of the ocean.

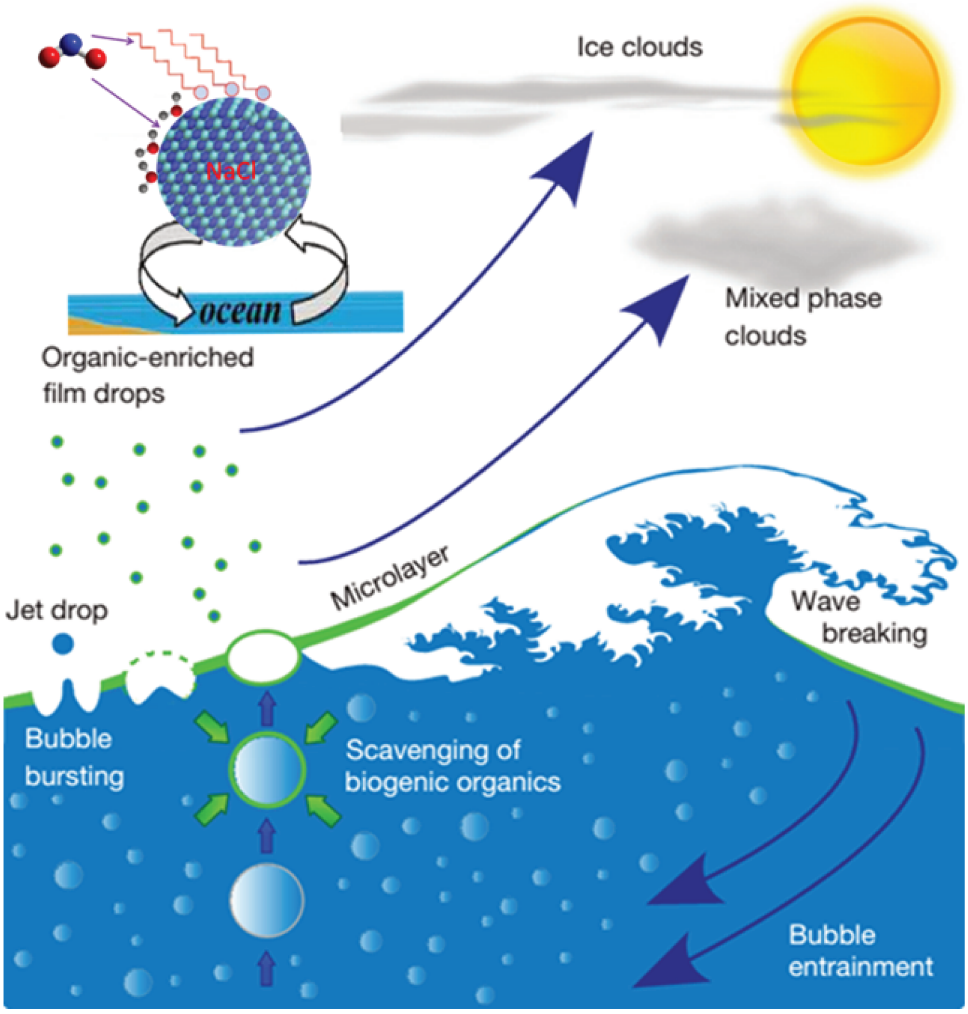

FIGURE 1.6: Creation of marine aerosol, organic from surface microlayer [38].

1.3 State of the art

MD simulations are invaluable tool to remplace or to support experimental data when it becomes difficult to perform experiments. Many examples of successful use of MD can be found in literature. Few MD calculations have been performed to model sea salt particles with organic molecules[44, 45, 46, 47, 48]. Previous studies have mostly focused on Langmuir monolayer at the air - water interface[44, 46], on water droplets[45, 47], nanoparticles[48] or in ionic solutions. For instance, Chakraborty and Zachariah [47] have investigated the effect of fatty acids, especially of their chain length, on the morphology and properties of water nanodroplets coated with these organics. Their results indicate that, for particles coated with long surfactants, the fatty acid chains tend to align parallel to each other, lowering the sticking coefficient of water vapor on such particles, whereas particles coated with shorter chains are more hydrophilic. Moreover, Takahama and Russell [46] have simulated impinging water vapor molecules on a slab of bare water and a slab of water coated by monomolecular organic films. The

mechanism of sticking is shown to depend on the compound, packing density, and resulting surface structure. In addition, MD simulations of water vapor interacting with Sodium Dodecyl Sulfate (SDS)/NaCl slabs[48] indicate that SDS kinetically hinders the initial water uptake partly due to the ordering of the SDS chains as the coverage increases. Most of the studies have focused on the effect of a full organic coated water slab or a nanodroplet on the sticking of incoming water molecules. As a complement to these studies, one of the purpose of the present thesis was to understand the effect of humidity on the organization of the coating for a partial coverage of the salt surface. MD manage also to reproduce models of some atmospheric mechanisms, such as surface activity and surface tension of CCN [49], stability of clusters [50], nucleation of particles[51], reactivity at the aerosol surface which combined some QM calculations [52, 53].

Also MD is a useful tool to get data which are either not reachable or complicated to get with experiments. To determine thermodynamics data, as liquid vapor pressure, enthalpy of vaporization and heats of sublimation, a quantum mechanic study combined with molecular dynamics made by Tong et al. in 2004 was done [54].

Concerning the uptake theory, many studies of mass accommodation coefficient were done onto planar surface or slab (mainly aqueous aerosol) [55, 56, 57, 58, 59] and mass accommodation coefficient is often close to 1 for aqueous aerosol. Chakraborty and Zachariah modelled water droplet coated with fatty acid of radius to investigate water molecule sticking coefficient [43]. They showed that the sticking coefficient for fatty acid coated water nano droplets is almost a constant (11-16%) for incident speeds around the most probable speed as opposed to 100% for water vapor incident on a pure water droplet. From other hand the equilibrium vapor pressure of water over these inverted micelles was considerably lower due to the surface tension effects of the fatty acid layer.

To model NO_2 reactivity on NaCl surface QM/MM methods are used in this thesis. This kind of method is an elegant way to introduce a quantum subsystem inside a big system which is described by classical MD. The QM/MM approach was introduced in 1976 in the the paper of Warshel and Levitt [60]. They, along with Martin Karplus, won the 2013 Nobel Prize in Chemistry for "the development of multiscale models for complex chemical systems". These methods are often used successfully in biology. Latest achievements are summarized in review article [61].

Recently QM/MM approach has been also used in aerosol modelisation. Nice combination of classical dynamical study and quantum mechanics tools has been introduced in the group of Kurt V Mikkelsen, to describe interaction between a phenol molecule and water cluster (aerosol). They have constructed PES between phenol and aerosol using parametrized interaction. From the PES, reaction pathways are determined. The QM/MM method is used to calculate a potential energy curve for each reaction path. Coupled cluster methods are used for the part of the system described by quantum mechanics, while the part described by molecular mechanics is represented by a polarizable force field. Furthermore, mass accommodation coefficients using the QM/MM and a quantum-statistical (QM-ST) model is calculated [62].

In the group of prof. Hans Agren molecular dynamic studies of aerosols are performed; they have also used QM/MM methods to model absorption

of light by nanoaerosol cluster [63]. They have use a multiscale integrated approach based on molecular dynamics and the QM/MM method to model the optical property, black carbon soot represented by fluoranthene with cis-pinonic acid, immersed in nanosized aerosol particles. Optical properties dependent on mixing state of mentioned molecules are studied. The small subsystem consisting of fluoranthene is described at the QM level (TD-DFT) and rest of the cluster, namely cis-pinonic acid and water are described classically.

Prof. Manolo Ruiz-Lopez has worked on the development of QM/MM methods and applications in the atmospheric chemistry. Nice example is the work done on reactivity of small radicals on air-water interface [64]. They have employed technique that combines molecular dynamics simulations together with a quantum/classical description of the formaldehyde-water system. They have shown that formaldehyde exhibits a preference for the air/water interface with respect to the bulk, roughly by 1.5 kcal/mol. Another important finding in these simulations is that frontier orbitals HOMO and LUMO undergo substantial stabilization at the interface due to surface water reorientation, which induces a local positive electrostatic potential.

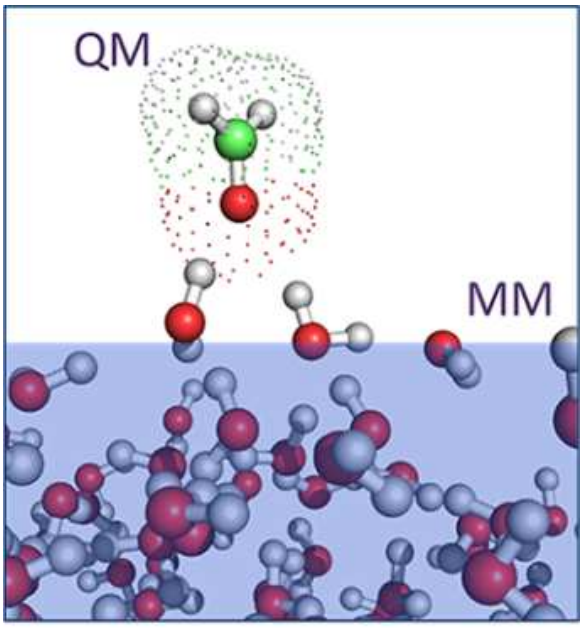

FIGURE 1.7: Snapshot of formaldehyde over water, formaldehyde is described on B3LYP level and water with molecular mechanics force-field [64].

1.4 Objectives of this thesis

As can be seen from the previous sections, organic compounds can clearly have a significant impact on aerosol physical and chemical properties, but our understanding of OA composition, physical and chemical properties, transformation characteristics is still limited. Indeed their impact is not presently described adequately in chemical transport and climate models. Among the mechanisms impacted by the properties of OA, the water uptake under diverse humidity conditions is one of the most important. It is important to determine if the organic compounds enhance or inhibit the

water uptake by aerosols, in particular at low relative humidity (RH). These open questions require fundamental studies to explain the phenomena and to model predictions for future conditions. The main objectives of this thesis is to use theoretical methods to give insights on these processes at the molecular level. These data are currently missing and we hope it can contribute in a better understanding of atmospheric chemistry.

We want to answer the following general questions:

1. What are the molecular mechanisms and kinetics of the chemical and physical processes involved?
2. How do organics influence the hygroscopic properties of the aerosols? How do they participate in nucleation? To which extent?
3. How do ageing processes influence the physicochemical properties of OA components, in particular their hygroscopicity ? How does the chemical transformation of OA by air pollutants influence the properties of the aerosols ?

More precisely, during this thesis, we have focused on:

1. The structuration of an organic coating on a sea salt under diverse physical conditions (humidity, temperature, quantity of organic compounds in the aerosol composition).
2. The heterogeneous reactivity of oxidant molecule with a sea salt aerosol containing organic aerosols.
3. The interaction of water molecules with organic matter.

This manuscript is divided in 6 chapters, including this introduction (Chapter 1) and the conclusion (Chapter 6). In the Chapter 2, I describe the numerical methods I have used during this thesis to model the aerosols and their interaction with water and other reactive atomospheric species. This chapter includes a description of the fundamental basis of classical molecular dynamics and of the quantum mechanics/molecular mechanics approach, but also a description of the force fields describing the interactions in the system. In the following chapters, I describe the application of these methods to three cases. Chapter 3 is dedicated to the modeling by means of classical molecular dynamics (GROMACS Package), of a NaCl(100) surface coated with palmitic acid (PA) molecules with varying the PA coverage and the humidity at two different temperatures. In chapter 4, I present a study of the uptake and reactivity of incoming NO_2 molecules at the previously modeled sea salt aerosol surface. To describe the reactive processes, a hybrid Quantum Mechanical/Molecular Mechanics (QM/MM) approach has been used. These QM/MM studies were performed with the CP2K package. The last study, detailed in chapter 5, corresponds to a molecular dynamics modeling of n-Butanol aerosol and aggregation by water uptake near the melting temperature.

Chapter 2

Methodology and tools

2.1 Classical molecular dynamics

2.1.1 Why we are using molecular dynamics

In the middle of the 20th century, the introduction of computers made feasible to exploit physical models and to simulate physical properties. Thereby, after successful Monte Carlo simulations in the 40s of the 20th century, Alder and Wainwright in late 50s [65] and Rahman in the 60s [66], independently, managed to simulate elastic collisions between idealized hard spheres. Rahman published milestone simulations of liquid argon using a Lennard-Jones potential. The calculated properties, such as the self-diffusion coefficient, compared well with experimental data [66]. Since the pioneering paper of Metropolis and Ulam [67], Monte Carlo methods has been widely used until nowadays. The first computer simulation of a liquid [68] was done in Los Alamos National laboratories using a computer named MANIAC. MANIAC had a memory of 600 words, storage of 80 KB, 11 KHz speed, and had 2,400 vacuum tubes. This means it was possible to calculate 10^3 operations in one second. Today personal computers can do over 10^{12} operations per second. During my PhD, most of the calculations were performed on the local cluster named SAKURA (https://wikis.univ-lille1.fr/phlam-pcmt/accueil), able to proceed hundreds of GHz operation in one second. Since first computers appeared, Monte Carlo (MC) and Molecular Dynamics (MD) became two important families of computer simulations. One of the interest of MD is that real trajectories are accessible, trajectories from which we can calculate physical quantities like time-dependent responses to perturbations, rheological properties and spectra. Concerning MC simulations, they are in principle more simple and computationally less demanding. Before going into the details of the method, it is interesting to explain why we use this method. Basically each MD simulation is like an experiment itself. We need to define the system and the interactions between the atoms and then propagate the system for sufficiently long time to have insight in the molecular processes. The resolution of experiments is limited in time and space, i.e. experimentalists often have access only to macroscopic quantities. MD simulations can bridge the gap between microscopic world and macroscopic quantities. For example, we can connect infrared spectrum with the electric dipole moment of the molecule. Surface tension (macroscopic value) can be connected with pressure tensor. It is also often too expensive or even not feasible to do experiments, especially in extreme conditions of temperature and pressure. In these cases, simulations are becoming inevitable.

For most of the physical quantities, it is sufficient to stay in the framework of classical MD. But with this method, it is not possible to describe the chemical reactivity and quantum effects. Subsequently, in the second phase of the my thesis, I have used ab initio MD (AIMD). This family of methods can provide quantum treatment of the system or of a part of the system, description of charge transfer, bond breaking, electronic structure properties, etc. for relatively large systems. However AIMD is much more computationally demanding than classical MD.
MD appeared to be the logical solution to model systems like submicrometer aerosol particles. On one hand, it gives enough details at the atomistic level with sufficiently good accuracy, on the other hand, it is capable to handle relatively large systems, in our studies typically 10's of nanometers evolving over few tens of nanoseconds. During the last decades, thanks to close collaborations between computer experts on one hand and between physicists and chemists on the other hand, extremely efficient softwares were developed. These softwares made possible to study bigger systems on larger time scales. Among these softwares, we used GROMACS [69] for the classical MD calculations. In order to perform quantum mechanical and AIMD calculations, the CP2K package [70] has been employed. Both are open source and free packages.

2.1.2 Statistical mechanics and molecular dynamics

In this section, I will not go in the details of statistical mechanics, my goal being rather to briefly present the connections between MD simulations and macroscopic quantities.

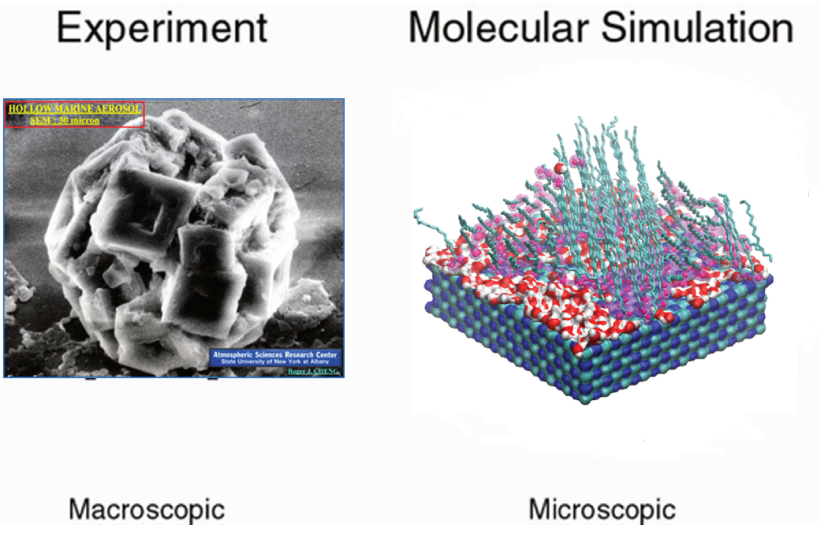

FIGURE 2.1: Illustration of macro and micro system. On the left: image of the sea salt aerosol, 10's of micron. On the right: modeled marine aerosol, 5 nm.

With laboratory techniques, one can measure macroscopic values such as pressure, density, structure, etc. Statistical mechanics enables us to connect the microscopic and macroscopic scale.
An ensemble is a concept introduced in statistical mechanics which can be

considered as a set of all possible microscopic states (configurations) of the system. We can imagine a system of particles distributed in a confined chamber. A set of all possible arrangements of particles is called ensemble[1]. A statistical ensemble is defined by the probability function of the different configurations.
In statistical mechanics, average values are defined as ensemble averages. The ensemble average is given by

$$< A >_{ensemble} = \int \int d\mathbf{p}^N d\mathbf{r}^N A(\mathbf{p}^N, \mathbf{r}^N) \rho(\mathbf{p}^N, \mathbf{r}^N) \tag{2.1}$$

Where $A(\mathbf{r}, \mathbf{p})$ is a physical observable depending on position $\mathbf{r}$ and momenta $\mathbf{p}$ vectors. The probability $\rho(\mathbf{p}^N, \mathbf{r}^N)$ of the states is defined as:

$$\rho(\mathbf{p}^N, \mathbf{r}^N) = \frac{1}{Q} exp[-H(\mathbf{p}^N, \mathbf{r}^N)/k_B T] \tag{2.2}$$

with H is the Hamiltonian, T is the temperature, k_B Boltzmann's constant and Q the partition function:

$$Q = \int \int d\mathbf{p}^N d\mathbf{r}^N exp[-H(\mathbf{p}^N, \mathbf{r}^N)/k_B T] \tag{2.3}$$

The evaluation of the integrals given previously is a very tedious job since it is necessary to calculate all possible states. In practice, a solution is to take time average of A. This equivalence is due to a fundamental axiom of statistical mechanics: the ergodic theorem [71], which states:

$$< A >_{ensemble} = < A >_{time} \tag{2.4}$$

then we can write:

$$< A >_{time} = \lim_{\tau \mapsto \infty} \frac{1}{\tau} \int_{t=0}^{\tau} A(\mathbf{p}^N(t), \mathbf{r}^N(t)) dt \approx \frac{1}{M} \sum_{it=1}^{M} A(\mathbf{p}^N(it), \mathbf{r}^N(it)) \tag{2.5}$$

where t is the simulation time, M is the number of time steps (it) in the simulation and $A(\mathbf{p}^N(t), \mathbf{r}^N(t))$ is the instantaneous value of A. For example, the average potential energy of system can be expressed as:

$$V = < V > = \frac{1}{M} \sum_{it=1}^{M} V_{it} \tag{2.6}$$

In a MD simulation, when the system has reached its equilibrium , if we let it evolve over an infinite period of time, the system will explore all possible states.
The radial distribution function (RDF) is a quantity which gives a lot of information about structural data. It is directly comparable with experiments since the structure factor (calculated as the Fourier transform of RDF) is directly comparable to diffraction patterns. The features of the RDF can give us informations about the structural properties of the sytem, for example its liquid or crystal character.

[1] Apart from position, this concept applies equally to velocities. Combining position and velocity, we can introduce the concept of phase space.

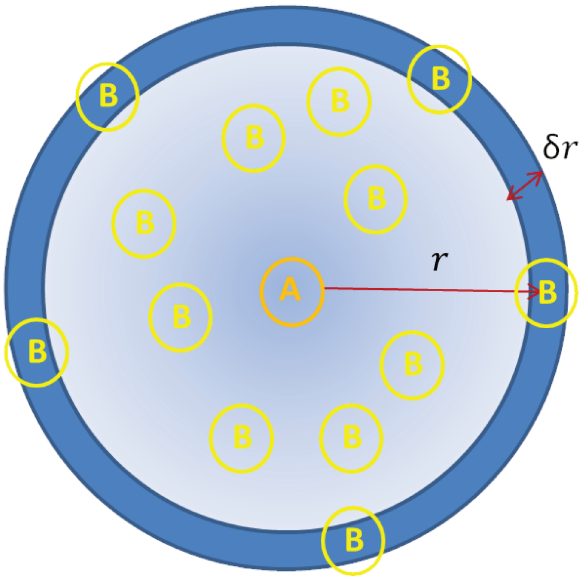

FIGURE 2.2: Spherical element used for the evaluation of the RDF.

Fig. 2.2 represents a sphere element of thickness $\delta \mathbf{r}$ used to calculate the RDF. The RDF $g_{AB}(r)$ gives the probability of finding a particle B at the distance r from a particle A. To calculate a RDF, the number of particles of type B comprised in the range $[r, r + \delta r]$ from particle A is counted:

$$g_{AB}(r + \delta r) = \frac{\rho_{AB}(r + \delta r)}{\rho_{Buniform}(r)} \tag{2.7}$$

where the functions $\rho_{AB}(r + \delta r)$ gives the density of particles B within a distance range $[r, r + \delta r]$ from particle A. $\rho_{Buniform}(r)$ is introduced to normalize the density obtained by averaging over all spheres around particles A.

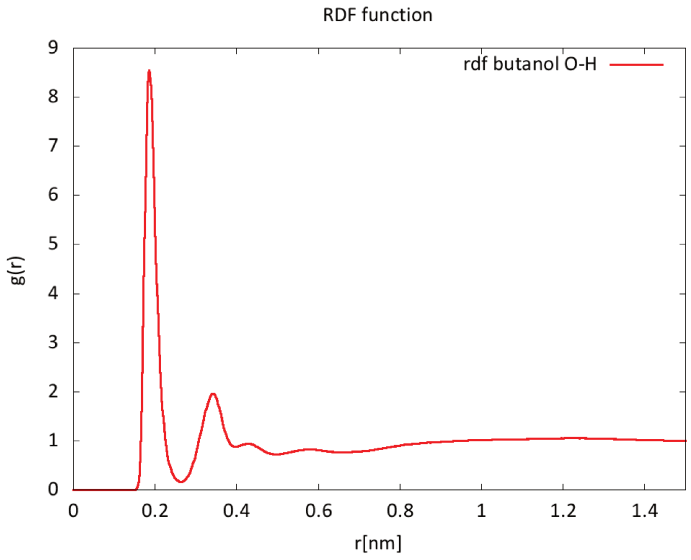

FIGURE 2.3: RDF function characterizing the O and H pair for liquid butanol

Fig. 2.3 represents a typical example of RDF function between oxygen and hydrogen in the liquid butanol. The first peak corresponds to the most probable distance between an O and an H atom of different molecules. In the next section, parametrization of particles interactions will be represented.

2.1.3 Force Fields

To properly define the physics of the system, one needs to define the interactions between particles which will drive the dynamics and consequently the ensemble distribution. Generally, interatomic potential can be written as a series expansion:

$$V_{TOT} = \sum_{i}^{N} V_1(\mathbf{r}_i) + \sum_{i,j>i}^{N} V_2(\mathbf{r}_i, \mathbf{r}_j) + \sum_{i>j>k}^{N} V_3(\mathbf{r}_i, \mathbf{r}_j, \mathbf{r}_k)... \tag{2.8}$$

V_1 corresponds to the one body terms, for example the interaction of a charged particle with an external electric field, V_2 corresponds to two-bodies terms, V_3 three-bodies terms, etc. N stands for the number of atoms (i, j, k) in the system.
The interaction energy of the system can often be written as a sum of pair potentials. This approximation is widely used and had many successes in theoretical modelisation even if 3-bodies effects are not included. For example, a common and well-known way to represent the dispersion-repulsion interaction is the Lennard-Jones (LJ) function. In the LJ formulation (eq. 2.9), the repulsion term is represented by the r^{-12} term and the dispersion by the r^{-6} part of potential. The repulsion corresponds to Pauli repulsion

at short ranges due to overlapping electron orbitals, and the long range dispersion term corresponds to interaction between "instantaneous" dipoles.

$$V_{LJ}(r_{ij}) = 4\epsilon((\frac{\sigma}{r_{ij}})^{12} - (\frac{\sigma}{r_{ij}})^{6}) \tag{2.9}$$

where ϵ is the depth of the potential, σ is the distance for which $V = 0$ and r_{ij} is defined as $r_{ij} = r_j - r_i$. Characteristic values are shown on Fig. 2.4

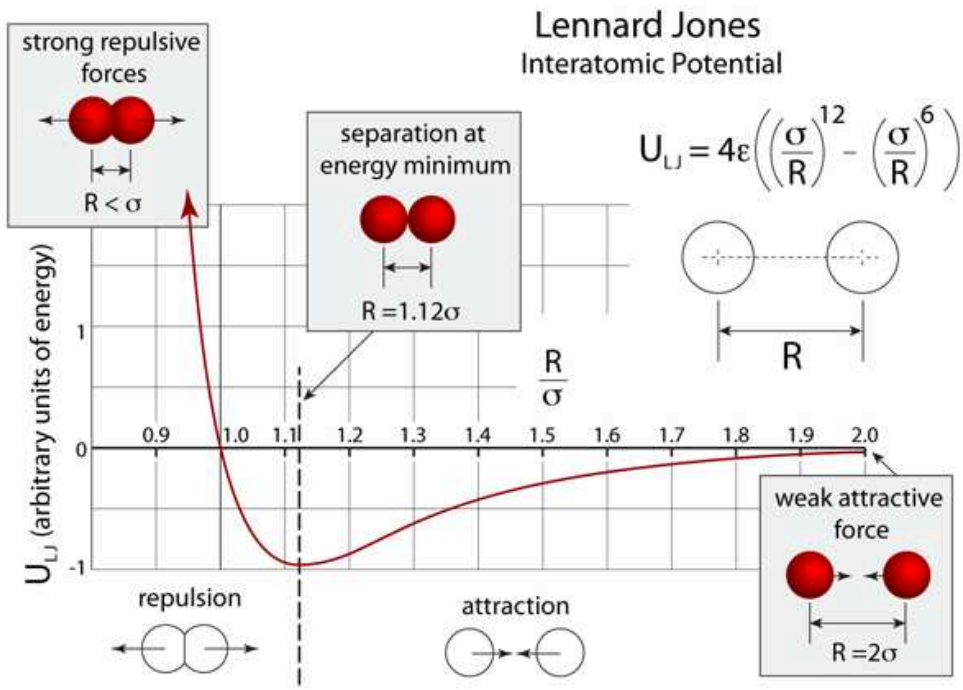

FIGURE 2.4: LJ potential and characteristic parameters. Figure taken from [72].

The Buckingham form represents another alternative to parametrize the dispersion-repulsion interaction, with the Pauli repulsion described by an exponential term whereas the van der Waals dispersion is still represented by a r^{-6} term.

$$V_{nb}(r_{ij}) = A\exp\left(-B(r_{ij})\right) - \frac{C}{(r_{ij})^6} \tag{2.10}$$

where A, B, and C are the suitable constants.
Similarly, the electrostastic interactions can be described by a charge-charge interaction term (first term in the Eq. 2.11). The total non-bonded interaction term writes:

$$V_{nb} = \sum_{i>j}(\frac{q_i q_j}{r_{ij}} + 4\varepsilon(\frac{\sigma_{ij}}{r_{ij}})^{12} - 4\varepsilon(\frac{\sigma_{ij}}{r_{ij}})^{6}) \tag{2.11}$$

It is then necessary to define intramolecular bonded interactions. Typically bonds are described by harmonic oscillators and periodic function for torsion angle (Fig. 2.5).

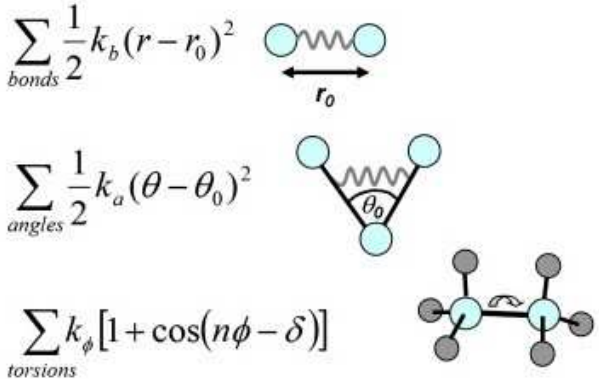

FIGURE 2.5: Intramolecular potential. Picture adapted from [73].

Then we can write the total potential energy of our system as:

$$V = V_{bonded} + V_{nonbonded} = \sum_{\text{bonds}} \frac{1}{2} k_r (r - r_0)^2 + \sum_{\text{angles}} \frac{1}{2} k_\theta (\theta - \theta_0)^2 + \\ + \sum_{\text{dihedrals}} k_\phi \left[1 + \cos(n\phi - \delta)\right] + \sum_{\text{atom } i} \sum_{j \neq i} \left[4\epsilon_{i,j} \left(\left(\frac{\sigma_{i,j}}{r_{i,j}} \right)^{12} - \left(\frac{\sigma_{i,j}}{r_{i,j}} \right)^{6} \right) + \frac{q_i q_j}{r_{ij}} \right] \tag{2.12}$$

The total energy of the system is then calculated as the sum of the intramolecular bonded interactions and pairwise additive nonbonded interactions described with Lennard-Jones and charge-charge coulombic interactions (Eq.2.12).

In Eq. 2.12, r corresponds to chemical bond length (described as a simple 'spring'); the bond angle θ is the angle between two chemical bonds at its equilibrium value, involving three atoms. The third term is for the dihedrals (a.k.a. torsion angles ϕ) where k_ϕ is the dihedral force constant, n is the multiplicity of the function, ϕ is the dihedral angle and δ is the phase shift.

The force fields, which are commonly used in molecular modeling such as biomolecular modeling or computer-aided drug design, are nowadays derived directly from quantum mechanical calculations, fitting charges and Lennard-Jones parameters to ab initio data. The group of Dr. Jorgensen used an other strategy to derive the Optimized Parameters for Liquid Simulation (OPLS) parameter set [74]. A initial set of parameters was guessed for the van der Waals parameters. Then some Monte Carlo simulations of pure liquids were performed and the van der Waals parameters were adjusted to reproduce experimental values of thermodynamic quantities such as density and heats of vaporisation. This OPLS force field has been used in this thesis since it has reproduced good results on biological system [75].

2.1.4 Trajectory propagation

An elegant way to formulate Newtonian mechanics is to combine kinetic and potential energy within the lagrangian formalism.

$$\mathcal{L}(\dot{\mathbf{r}}, \mathbf{r}) = \sum_{i=1}^{N} \frac{1}{2} m_i \dot{\mathbf{r}}_i^2 + V(\mathbf{r}_i) \tag{2.13}$$

where the summation is over the N particles in the considered system. The derived equations of motion are the Euler-Lagrange equations:

$$\frac{\partial}{\partial t}\left(\frac{\partial \mathcal{L}}{\partial \dot{\mathbf{r}}_i}\right) - \frac{\partial \mathcal{L}}{\partial \mathbf{r_i}} = 0 \tag{2.14}$$

$$\frac{\partial \mathcal{L}}{\partial \mathbf{r}_i} = \frac{\partial V}{\partial \mathbf{r_i}} = \mathbf{f}_i \tag{2.15}$$

$$\frac{\partial}{\partial t}\left(\frac{\partial \mathcal{L}}{\partial \dot{\mathbf{r}}_\mathbf{i}}\right) = m\ddot{\mathbf{r}}_i \tag{2.16}$$

By combining Eq. 2.15 and Eq. 2.16 into Eq. 2.14, we obtain the second Newton law.

$$\mathbf{f}_i = m\ddot{\mathbf{r}}_i = m\mathbf{a}_i \tag{2.17}$$

Basically, the algorithms generally used in MD simulations approximate the positions, velocities and accelerations using a Taylor series expansion:

$$\mathbf{r}(t+\delta t) = \mathbf{r}(t) + \mathbf{v}(t)\delta t + \frac{1}{2}\mathbf{a}(t)\delta t^2 + ... \tag{2.18}$$

$$\mathbf{v}(t+\delta t) = \mathbf{v}(t) + \mathbf{a}(t)\delta t + \frac{1}{2}\mathbf{b}(t)\delta t^2 + ... \tag{2.19}$$

$$\mathbf{a}(t+\delta t) = \mathbf{a}(t) + \mathbf{b}(t)\delta t + ... \tag{2.20}$$

We can write $\mathbf{r}(t-\delta t)$ and $\mathbf{r}(t+\delta t)$ separately. By addition of these two equations, we get:

$$\mathbf{r}(t+\delta t) = 2\mathbf{r}(t) - \mathbf{r}(t-\delta t) + \mathbf{a}(t)\delta t^2 + ... \tag{2.21}$$

The Verlet algorithm [76] uses the positions and accelerations at the time t and the positions at the time $(t-\delta t)$ to predict the positions at time $(t+\delta t)$, where δt is the integration step. The acceleration is obtained from Eq. 2.16. Velocities in the original Verlet algorithm are not explicitly calculated but they can be deduced from the eq. 2.22:

$$\mathbf{v}(t) = \frac{\mathbf{r}(t+\delta t) - \mathbf{r}(t-\delta t)}{2\delta t} \tag{2.22}$$

The evaluation of the velocity at time step t gives an error in order of δt^2. This can be significant if we want to calculate the energy at time step t and especially for controlling dynamics through barostat and thermostat. To obtain more accurate velocities, the leapfrog algorithm is generally preferred

using the velocities at half time step according to:

$$\mathbf{v}(t+\frac{\delta t}{2}) = \mathbf{v}(t-\frac{\delta t}{2}) + \mathbf{a}(t)\delta t. \tag{2.23}$$

and then positions are calculated:

$$\mathbf{r}_i(t+\delta t) = \mathbf{r}_i(t) + \mathbf{v}_i(t+\frac{\delta t}{2})\delta t. \tag{2.24}$$

Figure 2.6 presents the standard MD procedure in a simplified block diagram. One starts the simulation by defining the atoms, the force field, the atomic positions and velocities. Assuming that we have defined the potential, forces are calculated as the negative gradient of the potential. Particles are propagated and trajectories are stored in memory. The procedure is repeated until equilibrium is reached and the configurations are sampled. From equilibrated trajectories, we can deduce thermodynamical and structural properties as explained in section 2.1.2.

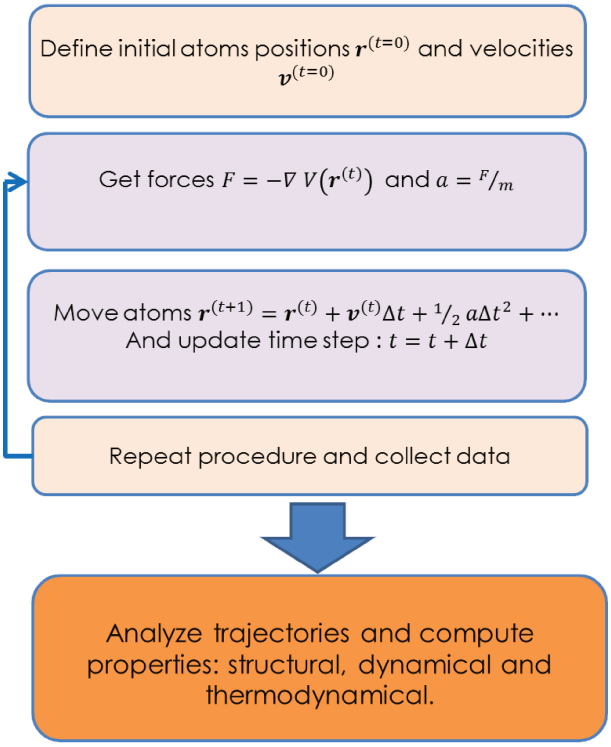

FIGURE 2.6: Block diagram which summarizes steps in order to proceed with MD simulation

Constraints

During the last decades, different tricks have been introduced to increase the speed of the calculations. In this section, I present the SHAKE algorithm for constraining bonds. Usually these constraints are employed to fix light atoms bonds (hydrogen) since the period of oscillations of these bonds is short when compared to others. This offers the possibility to use a time step of 2 fs or even larger, and then to reduce the numerical cost.

With the use of the SHAKE algorithm, we can impose constraints on the lengths of the bonds. In other words, we will change propagated unconstrained positions $\mathbf{r}'$ to $\mathbf{r}''$ while applying constraints set on initial positions $\mathbf{r}$. This can be formulated by Lagrange mechanics and holonomic constraints. The equations of motion must fulfil K holonomic constraints, expressed as:

$$\sigma_k(\mathbf{r}_1, ..., \mathbf{r}_N) = 0; k = 1...K. \tag{2.25}$$

An holonomic constraint σ, for example, can be expressed as $|\mathbf{r}_1 - \mathbf{r}_2|^2 = b^2$ where we constrain bond length to a preassigned value b.
The extended Lagrangian is written as :

$$\mathcal{L}^*(\mathbf{r}, \dot{\mathbf{r}}) = \mathcal{L}(\mathbf{r}, \dot{\mathbf{r}}) + \sum_{i=1}^{K} \lambda_i \sigma_i(\mathbf{r}) \tag{2.26}$$

where the summation is over K geometric constraints, $\mathcal{L}^*$ is the Lagrangian for the extended system, and λ_i is a Lagrange multiplier associated with a geometric constraint σ_i.
Lagrange multipliers λ_i are determined with following the iterative procedure:

1. Perform a standard MD step (leap-frog algorithm):

$$\mathbf{v}_i(t + \delta t/2) = \mathbf{v}_i(t - \delta t/2) + \frac{\mathbf{a}_i(t)}{m_i}\delta t \tag{2.27}$$

$$\mathbf{r}_i(t + \delta t) = \mathbf{r}_i(t) + \mathbf{v}_i(t + \delta t/2)\delta t \tag{2.28}$$

2. Use the new positions $\mathbf{r}(t + \delta t)$ to compute Lagrange multipliers for all constraints:

$$\lambda_k = \frac{1}{\delta t^2} \frac{\sigma_k(\mathbf{r}(t + \delta t))}{\sum_{i=1}^{K} m_i^{-1} \bigtriangledown_i \sigma_k(\mathbf{r}(t)) \bigtriangledown_i \sigma_k(\mathbf{r}(t + \delta t))} \tag{2.29}$$

3. Update the velocities and positions by adding a contribution due to restoring forces (proportional to λ_k):

$$\mathbf{v}_i(t + \delta t/2) = \mathbf{v}_i(t - \delta t/2) + \left(\mathbf{a}_i(t) - \sum_k \frac{\lambda_k}{m_i} \bigtriangledown_i \sigma_k(\mathbf{r}(t)) \right) \delta t \tag{2.30}$$

$$\mathbf{r}_i(t + \delta t) = \mathbf{r}_i(t) + \mathbf{v}_i(t + \delta t/2)\delta t \tag{2.31}$$

4. Repeat steps 2-4 until all $|\sigma_i(\mathbf{r})|$ are smaller than a predefined tolerance.

Details of the SHAKE method can be found in [77] and the VASP code manual [78].

2.1.5 Periodic boundary conditions and Ewald summation

Periodic boundary conditions

An elegant way to avoid border effects in a finite size systems and effectively to simulate bulk is the application of periodic boundary conditions (PBC). The idea is to surround the original box with replica of itself. Usually potential cutoff is chosen to be smaller than half-size of the box and we can adopt the minimum image convention. This convention states that each atom interacts with the nearest atom or image in its periodic image. During the simulation, if an atom leaves the original simulation box, it appears at the opposite side of the box. This is shown in Fig. 2.7. Of course, it is important to bear in mind the artificial periodicity when considering properties which are influenced by long-range correlations and size of the system. By this trick, we have solved the boundary problem but infinite long range interactions are introduced. This problem can be solved by Ewald summation.

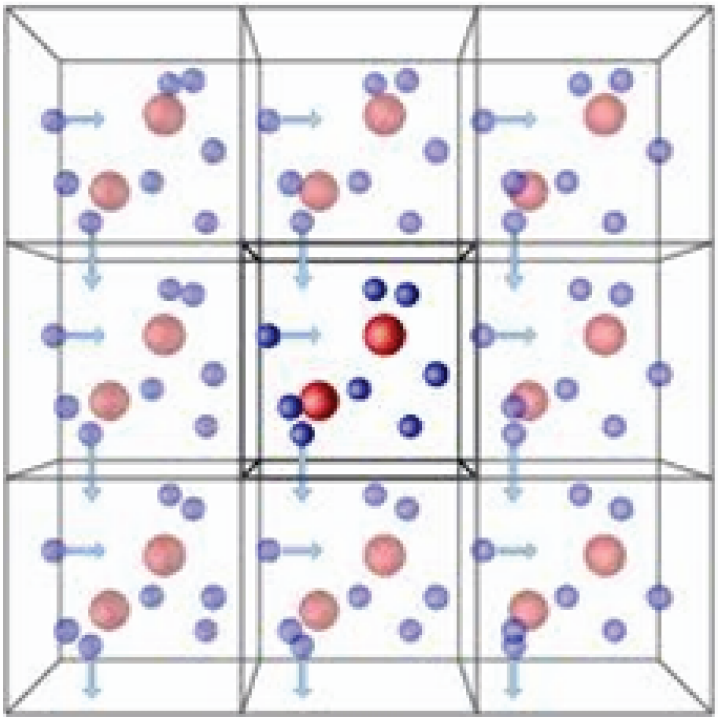

FIGURE 2.7: Application of PBC. Image copies are shadowed while the primary box is represented in darker colors. Picture taken from $http://isaacs.sourceforge.net$

Using PBC, the total charge-charge electrostatic interaction energy is written as:

$$U(\mathbf{r}_i) = \sum_{j<i} \sum_{n} \frac{q_i q_j}{|\mathbf{r}_{ij} + \mathbf{n}|} \tag{2.32}$$

where

$$\mathbf{n} = (\hat{x}, \hat{y}, \hat{z}) m\mathrm{L} \quad with \quad m = \pm 0, \pm 1, \pm 2....$$

and L is the size of cell. In Eq. 2.32, pairs are all explicitly counted to avoid double counting.

This direct summation is simple to implement, but is very computer demanding. For finite and small systems, the sum converges quickly, but not for large systems or infinite system, as is the case for systems described by introducing PBC. To evaluate this sum numerically, we can truncate the sum at some cut-off distance, assuming that the contributions from large n can be neglected. But the ignored contributions beyond this cut-off distance introduce systematic errors to the calculation. The sum for Lennard-Jones interaction, with $1/r^6$ and $1/r^{12}$ decaying rapidly, converges fast. But for long range interactions (such as electric contributions, with a $1/r$ or $1/r^3$ dependence), the evaluation of the direct sum method requires a large cut-off to get accurate results. Therefore, the direct sum method is not used for simulations of large systems.The Ewald sum is a faster method to compute electrostatic energies or forces.

Ewald long range summation

The most model solution to this problem was proposed by Ewald [79]. His idea was to replace the diverging sum of long range interactions by two converging sums.

Generally we separate $1/r$ into two contributions:

$$\frac{1}{r} = \frac{f(r)}{r} + \frac{1-f(r)}{r} \tag{2.33}$$

where $r = |\mathbf{r}_{ij} + \mathbf{n}|$. The error function erf and its complement $erfc$ are introduced:

$$erf(x) = \frac{1}{\sqrt{\pi}} \int_0^x e^{-t^2}\,\mathrm{d}t \tag{2.34}$$

$$erfc(x) = 1 - erf(x) = \frac{2}{\sqrt{\pi}} \int_x^\infty e^{-t^2}\,\mathrm{d}t \tag{2.35}$$

Combining 2.33, 2.34, 2.35 and introducing the term α which is an arbitrary parameter governing the relative convergence of the two series, we obtain:

$$\frac{1}{r} = \frac{erf(\frac{1}{2}\alpha r)}{r} + \frac{erfc(\frac{1}{2}\alpha r)}{r} \tag{2.36}$$

Using Eq. 2.32, we can write the overall expression as:

$$V(\mathbf{r}_{ij}) = \frac{1}{2}\sum_n \sum_{i=1}^{N}\sum_{j=1}^{N} q_i q_j \frac{erfc(\alpha(|\mathbf{r}_{ij}+\mathbf{n}|))}{(|\mathbf{r}_{ij}+\mathbf{n}|)} - \\ - \frac{2\pi}{V}\sum_{k\neq 0} e^{-k^2/4\alpha^2} k^2 \sum_{i=1}^{N} q_i e^{-i\mathbf{k}\cdot\mathbf{r_{ij}}} k^{-2} e^{-k^2/4\alpha^2} - \frac{\alpha}{\pi^{1/2}}\sum_{i=1}^{N} q_i^2 \tag{2.37}$$

The first term in Eq. 2.37 converges quickly in real space and the second one converges in k space. Erfc function can be seen as a summation of point charges and centered Gaussian functions, visible as a real space lattice in Fig. 2.8. Gaussian like charges are added in place of point charges with opposite signs. Lattice in k space represents gaussian like charges added to screen the diffuse charges of the real space lattice. The parameter α defines

the width and height of the spreading function and thereby the effective size of the charges.

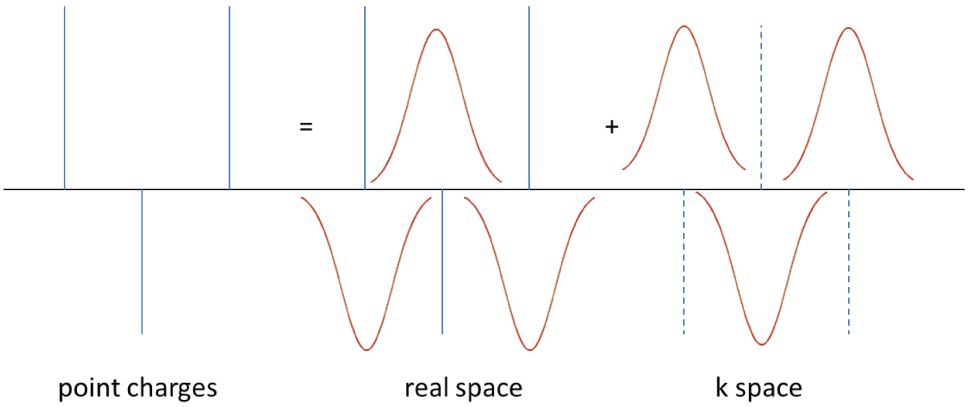

FIGURE 2.8: Separation of the original lattice into two subspaces: the first one in real space and the second one in reciprocal space.

The details of the derivation can be found in Frenkel and Smith 2002 [80] or Gibbon and Sutmann 2002 [81].

Particle Mesh Ewald (PME)

The Ewald method was a huge contribution in the field but it still scales with N^2, N being the number of charged particles in the primary box. For small systems, Ewald is still a good choice for the reason of simplicity but nowadays systems are getting bigger and there is a need for further improvements. Particle Mesh Ewald is among these improvements achieving a $NlogN$ scaling [82]. In Ewald method, the summation in real space converges fast since Gaussian charge distribution looks like point charges at large distance. By increasing the distance, total charge becomes zero. Thereby most of the improvements can be achieved in the k space summation.
The inter-particle energy contribution is split into short range and long range parts. The short range part is simply a sum of pair potentials. For the long range part, instead of directly summing wave vectors, the charges are assigned to a grid using interpolations. The grid is then Fourier transformed with a FFT algorithm. The reciprocal energy term is then obtained by a single sum over the k-space grid. The cutoff radius for short and long range interactions are chosen to optimize accuracy as well as computational cost.

2.1.6 Controlling dynamics

Proceeding with equations presented in the previous sections would yield the microcanonical ensemble (NVE), where number of particles (N), volume (V), and energy (E) are preserved. Potential and kinetic energy are fluctuating but the sum stays constant in what is called an adiabatic process. However, we prefer to do simulations with a constant temperature

and pressure since these are conditions which we meet in either experiments or natural occurring physical phenomena. Usually, the first step is to apply a thermostat which yields canonical ensemble having number of particles (N), volume (V) and temperature (T) conserved. The second step is to introduce a barostat which leads to so called isothermal–isobaric ensemble with constant number of particles (N), pressure (P) and temperature (T). Hereby, as an example, I present the *weak-coupling* Berendsen scheme for thermostat and barostat. The equipartition theorem states that temperature is directly connected with the average kinetic energy. This can be written by using Eq. 2.38. The basic principle in most of the approaches is to maintain the temperature by re-scaling the velocities.

$$\frac{3}{2}Nk_BT = \frac{1}{2}\sum_i m_i\mathbf{v}_i^2 \tag{2.38}$$

To assign initial velocities to particles, one could use, for example, Gaussian distribution and then re-scale velocities to desire temperature T_0. The system is then propagated and after each step λ is calculated (Eq. 2.39) and immediately we re-scale all the velocities, corresponding to the instantaneous temperature T_i with given λ. This is the simplest way to achieve constant temperature and thereby kinetic energy in the system.

$$\lambda = \sqrt{(T_0/T_i)} \tag{2.39}$$

Berendsen thermostat

Berendsen algorithm is used to provide a weak-coupling to an external bath with given temperature [83]. This is achieved by scaling velocities at a given time step by $v' = \lambda\mathbf{v}$. Parameter λ_{Ber} is calculated as:

$$\lambda_{Ber} = \left[1 + \frac{\Delta t}{\tau}\left(\frac{T_0}{T} - 1\right)\right]^{\frac{1}{2}} \tag{2.40}$$

where Δt is the time step, T is the current temperature, T_0 is the desired temperature, and τ is a time constant characterizing the coupling with the thermostat.

Since the Berendsen thermostat directly scales kinetic energies, some properties may be affected, like heat capacity. An improvement of Berendsen thermostat is the velocity rescaling thermostat which is essentially Berendsen thermostat with stochastic term dK which improves kinetic energy distribution.

$$dK = (K_0 - K)\frac{dt}{\tau_T} + 2\sqrt{\frac{KK_0}{N_f}}\frac{dW}{\sqrt{\tau}} \tag{2.41}$$

where K is the kinetic energy, K_0 is the desired kinetic energy, N_f the number of degrees of freedom and dW is a Wiener noise [84].

Andersen thermostat

The Andersen thermostat is a simple stochastic thermostat which tends to correctly sample the NVT ensemble [85]. At each time step, number of particles is selected randomly, and their velocities are assigned by using a gaussian distribution at the desired temperature:

$$P(p) = \left(\frac{k_B T_0}{2\pi m}\right)^{3/2} \exp\left[-k_B T_0 p^2/(2m)\right] \tag{2.42}$$

Andersen thermostat mimics particle collisions with a bath of particles at a specified temperature T.

Berendsen barostat

To efficiently control the dynamics, the use of a thermostat is often not sufficient. To introduce constant pressure in the system, one needs to use a barostat. I will present the basic principles of the Berendsen barostat [83], which I have used in my studies.
The pressure in MD simulation is defined as:

$$P = \rho T + vir/V \tag{2.43}$$

where vir denotes the virial:

$$vir = \frac{1}{3}\sum_{i>j} \mathbf{f}\left(\mathbf{r}_{ij}\right) \cdot \mathbf{r}_{ij} \tag{2.44}$$

where $\mathbf{f}\left(\mathbf{r}_{ij}\right)$ represents the force on the $i-th$ particle, at distance $\mathbf{r}_{ij}$ from the particles j. The approach is similar to the Berendsen thermostat. Here each dimension of the box and positions are rescaled.

$$\mathbf{r}_i \to \mu \mathbf{r}_i; L \to \mu L \tag{2.45}$$

In GROMACS, this scaling is achieved with scaling matrices defined as:

$$\mu_{ij} = \delta_{ij} - \frac{\Delta t}{3\tau}\beta_{ij}\left\{P_{0ij} - P_{ij}(t)\right\} \tag{2.46}$$

Here, β is the isothermal compressibility of the system. In the case of an isotropic system β is a diagonal matrice. Real matrices μ are written as:

$$\mu\prime = \begin{pmatrix} \mu_{xx} & \mu_{xy} + \mu_{yx} & \mu_{xz} + \mu_{zx} \\ 0 & \mu_{yy} & \mu_{yz} + \mu_{zy} \\ 0 & 0 & \mu_{zz} \end{pmatrix} \tag{2.47}$$

2.1.7 How does it look in practice?

There is a significant number of commercial or open-access program packages which enable users to work independently. Packages are often well documented with available examples. During my thesis, I have worked with the GROMACS package to perform classical MD. GROMACS offers a complete manual [ftp.gromacs.org/pub/manual/manual-5.1.2.pdf] and

nice tutorials (www.bevanlab.biochem.vt.edu/Pages/Personal/justin/gmx-tutorials/). In this section, I will briefly explain the technical steps of a MD simulation (Fig. 2.9).

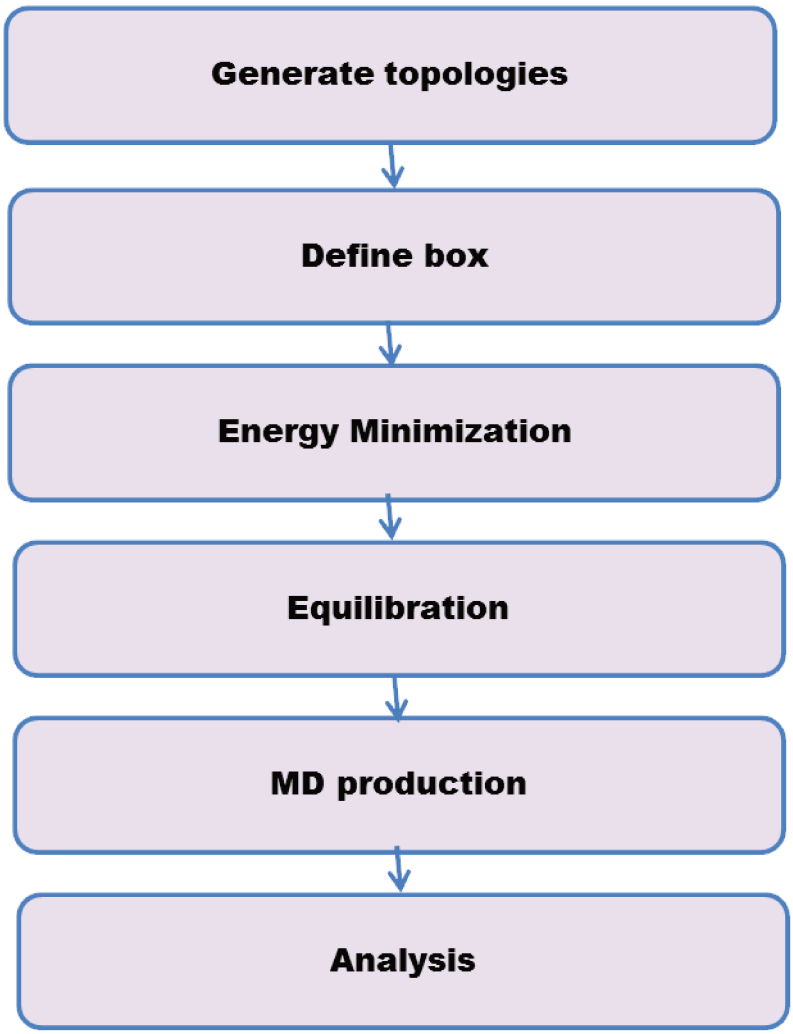

FIGURE 2.9: Schematic MD algorithm

When starting the simulation, one needs to define the molecules types in a topology file, and define in the proper format the force field to be used. In my thesis, I have employed OPLS-AA [74] force field, but other force fields are available as CHARMM [86], GROMOS [87], etc.

In a second step, we define the simulation box. Energy minimization is first performed to move the atoms on the potential energy surface in order to remove spurious interactions (atoms too close from each other and other non physical situations). An equilibration, performed in 2 steps, follows the minimization. First, in a NVT ensemble, the system is relaxed. This ensemble is also referred as "isothermal-isochoric" or "canonical". Then, the second phase is conducted in the NPT ensemble. The simulation time required to reach equilibrium depends strongly on the system. When the equilibrium is reached, MD production is performed during tens or hundreds of nanoseconds. In the production phase, data are stored at given time intervals such as positions, velocities, ... These data are then used in

the analysis. Finally, analysis on the equilibrated trajectories is done in order to obtain statistical averages. The energy convergence criteria are often used to check if the system is equilibrated. The time step used in simulation is limited by the time scale oscillation of the the lightest atoms in the system (typically hydrogen). If SHAKE algorithm (or an other algorithm) to constrain bonds is not used, the time step is limited to 0.5-1 fs maximum. Using bond length constraint algorithm, a 2 fs time step can be used, which is the case in this thesis.

During my PhD, most of the calculations were performed on the local cluster named SAKURA (https://wikis.univ-lille1.fr/phlam-pcmt/accueil), able to proceed hundreds of GHz operation in one second. Since this cluster is shared between all members of laboratory, the accessible number of nodes is changing all the time.

Simulation time is very dependent on the studied system. For example, one classical MD simulation of a 50 ns trajectory for a system with 10 000 atoms takes one week on one node of 16 cores and speed of 2.7 GHz each core. Ab initio MD simulations are much more demanding. Indeed to perform one ps of trajectory (for the systems represented in Chapter 5), it requires at least one week.
Some of the analysis of the calculated trajectories were performed with pre-existing codes implemented in GROMACS package like RDF calculation. But I had to write my one code to perform some specific calculations like energy and angle distributions. As concerns the results obtained by CP2K (Chapter 5), the analysis has been done externally using my own code since CP2K does not have module to analyse trajectories.

2.2 Ab initio methods

The Schrödinger equation can be solved by separation of time and spatial variables. The time independent Schrödinger equation derived from separated wave function as a product of spatial and time part is written as [88]

$$\hat{H}\Psi = E\Psi \tag{2.48}$$

where $\hat{H}$ is the Hamiltonian of the system and Ψ is an N-body wave function, E denotes the energy of the system. This equation is a typical mathematical problem of finding eigenvalues and eigenvectors.
The Hamiltonian of a system of nuclei and electrons, in atomic units, can be written as:

$$\begin{aligned}\hat{H} \;=\; & \sum_{i}^{n} -\frac{1}{2}\nabla_i^2 + \sum_{A}^{N} -\frac{1}{2}\nabla_A^2 + \sum_{i}^{n}\sum_{A}^{N} \frac{Z_A}{|\mathbf{r}_i - \mathbf{R}_A|} + \\ & + \sum_{i}^{n}\sum_{j\neq i}^{n} \frac{1}{|\mathbf{r}_i - \mathbf{r}_j|} + \sum_{A}^{N}\sum_{B\neq A}^{N} \frac{Z_A Z_B}{|\mathbf{R}_A - \mathbf{R}_B|}\end{aligned} \tag{2.49}$$

The two first terms correspond to the kinetic energy of electrons and nuclei respectively. The third term describes nuclei-electrons interactions. The last two terms are electron-electron and nuclei-nuclei interactions. To solve this many-particles Schrödinger equation is a very difficult task and is analytically possible only for Hydrogen atom and He^+, He_2^+, HeH^+ ions.

The development of so called quantum chemistry and physics is based on an interplay between approximations and development of numerical methods to solve this equation.
Atomic units ($e = m_e = \hbar = 4\pi\epsilon_0 = 1a.u.$) are used in this thesis.

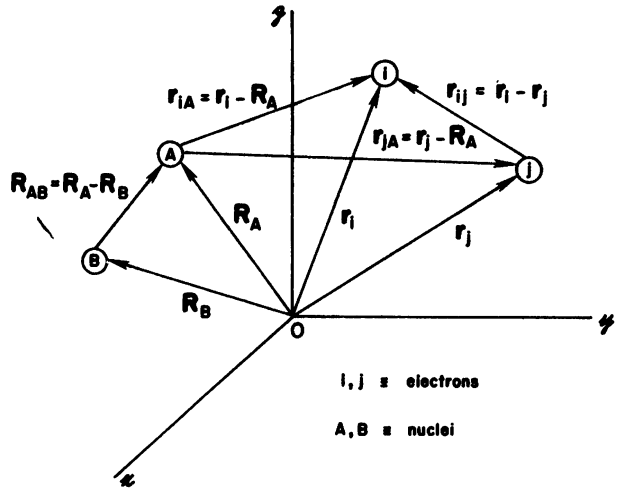

FIGURE 2.10: System of atomic nuclei and electrons represented in Cartesian coordinate system. Figure taken from [88].

2.2.1 Born-Oppenheimer approximation and Hartree-Fock approach

The Born-Oppenheimer (BO) approximation [89], a key concept in the quantum chemistry, is the first step in the simplification of the problem. In the following section, I will explain qualitative aspects of BO approximation. The Hamiltonian (Eq. 2.49) is simplified if the movement of electrons can be considered as instantaneous regarding to the movement of the nuclei. This approximation is reasonable since the mass ratio between electrons and proton is huge ($m_p/m_e = 1836.15267389$). In some cases, this BO approximation however breaks down. For example, the BO approximation fails when two electronic states (almost) cross. The description of non adiabatic transitions at conical intersections is of fundamental interest in photochemistry as well [90]. Effectively the second and last terms in Eq. 2.49 will be neglected, the second one because nuclei are fixed and the last one because Coulomb interaction between nuclei in this approximation is just a constant. The Hamiltonian is then written as a pure electronic term:

$$\hat{H}_{elec} = \sum_{i}^{n} -\frac{1}{2}\nabla_i^2 + \sum_{i}^{n}\sum_{A}^{N} \frac{Z_A}{|\mathbf{r}_i - \mathbf{R}_A|} + \sum_{i}^{n}\sum_{j\neq i}^{n} \frac{1}{|\mathbf{r}_i - \mathbf{r}_j|} \tag{2.50}$$

The Schrödinger equation for the electronic part is now written as:

$$\hat{H}_{elec}\Psi_{elec} = E_{elec}\Psi_{elec} \tag{2.51}$$

and the wave function Ψ_{elec} depends explicitly on electron positions and only parametrically on the nuclei positions:

$$\Psi_{elec} = \Psi_{elec}(\{\mathbf{r_i}\}; \{\mathbf{R_A}\}) \tag{2.52}$$

and

$$E_{elec} = E_{elec}(\mathbf{R_A}) \tag{2.53}$$

This approximation will be used for the remainder of this work. It is important to note that this approximation does not limit the techniques described only to systems of fixed nuclei; once the electronic configuration is known, the nuclear degrees of freedom could also be solved, giving rise to nuclear motion. This is presented in section 2.2.2. In the following, for a reason of simplicity, spin is not taken into account explicitly.

Hartree-Fock approximation

A full quantum solution to the problem given above even with BO approximation of any non-trivial size is unreachable. But approximations such as the Hartree-Fock allow to replace the n electrons problem by n problems with a single electron. Hereby I present the Hartree-Fock approach, since it serves as a first quantitative understanding of post Hartre-Fock methods which are nowadays extensively used.
If we solve the Schrödinger equation separately for each electron without including the electron-electron interaction, the solution Ψ^0 would be close to the true electron wave function Ψ_e.

$$\hat{H}^0\Psi^0 = E^0\Psi^0 \quad where \quad \hat{H}^0 = \sum_i^n h_i \tag{2.54}$$

where h_i is the mono-electronic Hamiltonian for electron i. This n-electron equation can be separated into n one electron equations, Ψ^0 can be written as a product of one electron functions $\Psi_a^0(\{\mathbf{r_i}\}; \mathbf{R_A})$, where a denotes a spin-orbital. The energy of an electron "located" in orbital a is calculated from the equation:

$$h_i\Psi_a^0(i) = E_a^0\Psi_a^0(i) \tag{2.55}$$

$\Psi_a^0(i)$ represents the orbital occupied by electron i with coordinate $\mathbf{r_i}$ and parametrically depending on the nuclear arrangement $\{\mathbf{R_A}\}$. The overall function Ψ^0 is represented by the product of mono-electronic wavefunctions:

$$\Psi^0 = \Psi_a(1)\Psi_b(2)...\Psi_z(n) \tag{2.56}$$

1,2,...n denotes electrons and a,b,...z orbitals. Due to the Pauli exclusion principle, the wavefunction has to be to be antisymmetric with respect to an interchange of any two electrons positions, i.e.

$$\Psi(\mathbf{r}_1, \mathbf{r}_2, \ldots, \mathbf{r}_i, \ldots, \mathbf{r}_j, \ldots, \mathbf{r}_N) = -\Psi(\mathbf{r}_1, \mathbf{r}_2, \ldots, \mathbf{r}_j, \ldots, \mathbf{r}_i, \ldots, \mathbf{r}_N) \quad . \tag{2.57}$$

By definition, a change of row or column in determinants leads to a change of sign of the determinant. By this, antisymmetry is preserved and we can

elegantly write Ψ^0 as a so called Slater determinant:

$$\Psi^0 = \begin{vmatrix} \psi_a(\mathbf{r}_1) & \psi_a(\mathbf{r}_2) & \cdots & \psi_a(\mathbf{r}_N) \\ \psi_b(\mathbf{r}_1) & \psi_b(\mathbf{r}_2) & \cdots & \psi_b(\mathbf{r}_N) \\ \vdots & \vdots & & \\ \psi_z(\mathbf{r}_1) & \psi_z(\mathbf{r}_2) & \cdots & \psi_z(\mathbf{r}_N) \end{vmatrix} , \tag{2.58}$$

An improvement of this approximation is the treatment of electron interaction. In the Hartree-Fock scheme, this interaction is treated in an average way. An electron is moving in the field induced by nuclei and the n-1 other electrons. This is called mean-field approximation. Consequently, the Hamiltonian now will be expressed as:

$$\hat{H} = \sum_i^n h_i^c + \frac{1}{2}\sum_{j<i}\frac{1}{r_{ij}} \tag{2.59}$$

where h_i^c is one-electron core Hamiltonian and is written as:

$$h_i^c(1) = -\frac{1}{2}\nabla_1^2 - \sum_A \frac{Z_A}{r_1 - r_A} \tag{2.60}$$

Calculating expectation value of the total energy $E = \langle\Psi_0|\hat{H}|\Psi_0\rangle$ and applying the variational principle, [88] in order to minimize the total energy while using Lagrange multiplier to keep Ψ^0 normalized, leads to the Eq. 2.61:

$$\frac{\delta}{\delta\psi}\left[< \hat{H} > - \sum_j \lambda_j \int |\psi_j|^2 d\mathbf{r} \right] = 0 \ . \tag{2.61}$$

where $< \hat{H} >$ is the total Hartree-Fock energy and λ_j are the Lagrange multipliers. This leads to the following set of Schrödinger-like equations called Hartree-Fock equations:

$$f_i\psi_a(\mathbf{r}_i) = \epsilon_a\psi_a(\mathbf{r}_i) \tag{2.62}$$

with the Fock operator defined as:

$$f_i = h_i + \sum_{j=1}^N (\hat{J}_j(i) - \hat{K}_j(i)) = -\frac{1}{2}\nabla_i^2 - \frac{Z}{r} + \sum_{j=1}^N (2\hat{J}_j - \hat{K}_j) \tag{2.63}$$

$$h_i = -\frac{1}{2}\nabla_i^2 - \frac{Z}{r_i} \tag{2.64}$$

Operators $\hat{J}$ and $\hat{K}$ are defined by operation on a wave function:

$$\hat{J}_j(1)\psi_a(1) = \left[\int \psi_j^*(2)\frac{1}{r_{12}}\psi_j(2)d\mathbf{r_2}\right]\psi_a(1) \tag{2.65}$$

$$\hat{K}_j(1)\psi_a(1) = \left[\int \psi_j^*(2)\frac{1}{r_{12}}\psi_i(2)d\mathbf{r_2}\right]\psi_j(1) \tag{2.66}$$

The physical meaning of operator $\hat{J}$ is that it represents a quantum interpretation of Coulomb interaction. But the operator $\hat{K}$ does not have any classical analogue. This operator introduces exchange of orbitals in Eq. 2.66. This operator is then called exchange operator. It contributes to spin correlation effects and in nature is a pure quantum effect.
To obtain the Fock orbitals (Eq. 2.62), we need the Fock operator which depends on Fock orbitals. In other words, we need to know the solution to this equation in order to solve the equation. The self-consistent field (SCF) method is thus used, where one makes first guess on initial orbitals and in the next step orbitals are changed to improve solution of Fock equation. The procedure is repeated until convergence is obtained, i.e when difference of orbitals and in total energy in step $n+1$ compared with orbital in step n is smaller than some predefined value.

Linear combination of atomic orbitals

In the Hartree–Fock calculations, the one-electron wave functions are approximated by a linear combination of atomic orbitals (Eg. 2.67). In the beginning, Slater-type function were used to expand orbitals. Now Gaussian-like functions are used for their computational efficiency reason.

$$\psi_a = c_{1a}\chi_1 + c_{2a}\chi_2 + c_{3a}\chi_3 + \cdots + c_{na}\chi_n \tag{2.67}$$

or

$$\psi_a = \sum_r c_{ra}\chi_r \tag{2.68}$$

Successes and drawbacks of the Hartree-Fock method

This method is a huge milestone in the calculation of electronic structure. All ab initio methods are based on this approach. Also the exchange effect is included in the Hartree-Fock equations. This is a great achievement of the Hartree-Fock method. Moreover it gives rather good results for many problems.
In the Hartree-Fock scheme, electron correlation is not treated, electron is modeled as moving in the averaged potential induced by other fixed electrons, this is the so-called mean-field theory. This approach gives to high energy because electron repulsion is not exactly described, interaction is rather calculated with electron averaged density. Also Hartree-Fock methods include only single reference in describing a given molecular state, whereas electrons rather fill in different shells.

2.2.2 Ab Initio Molecular Dynamics in the frame of Density Functional Theory

Ab Initio Molecular Dynamics (AIMD) is a method which incorporates classical description of particle trajectories and quantum (ab initio) methods to calculate potential and forces. The methods and the mathematical tools represented in 2.1.2 and 2.1.4 can be also applied in this frame. Forces obtained from electronic structure theory calculations are used in AIMD to make the system evolve in time, i.e. the potential energy of the system can be calculated "on the fly" using quantum mechanics. This is the basic concept of

AIMD. AIMD calculations generally are more accurate than classical MD calculations especially for systems exhibiting charge transfers, many body van der Waals effects, strong spin-orbit coupling and electron correlation. The major drawback is the limitation to systems of much smaller size and shorter time scales because of the computational cost. Thus the use of Density Functional Theory (DFT) to calculate potential energy $U = U(r_1, ..., r_N)$ comes naturally since DFT is the fastest method to calculate electronic structure with satisfying accuracy.

Density Functional Theory

Hereby I briefly present the key concepts of the DFT method. Born-Oppenheimer approximation as in Hartree-Fock approach is used. In the frame of DFT, Eq. 2.51 is reduced from $3n$ spatial coordinates, where n is number of electrons, to 3 spatial coordinates. The energy of the electronic system is written in terms of the electron probability density ρ. For the system of n electrons: $\rho(\mathbf{r}) = n \int \mathrm{d}^3 r_2 \cdots \int \mathrm{d}^3 r_n \Psi^*(\vec{r}, \vec{r}_2, \ldots, \vec{r}_n)\Psi(\vec{r}, \vec{r}_2, \ldots, \vec{r}_n)$. The electronic energy E is said to be a functional of the electron density and is denoted $E[\rho(\mathbf{r})]$, in the sense that for a given function $\rho(\mathbf{r})$, there is a single corresponding energy. The conventional normalization $\langle\Psi|\Psi\rangle = n$ is adopted.

Hohenberg-Kohn theorems

The Hohenberg-Kohn theorems [91] state that the total energy is a unique functional of the electron density, within an additive constant. The external potential, $V_{ext}(r)$ and the number of electrons, $n = \int \mathrm{d}\mathbf{r}\ \rho_0(\mathbf{r})$, determine completely the ground-state properties of the system.

$$E[\rho] = F[\rho] + \int \rho(\mathbf{r}) V_{ext}(\mathbf{r}) d\mathbf{r} \tag{2.69}$$

$$V_{\text{ext}}(\mathbf{r}) = -\sum_A \frac{Z_A}{|\mathbf{r} - \mathbf{r}_A|} \tag{2.70}$$

where the sum is over all ion cores. F, the universal functional, is the same for all systems of n non-interacting electrons, so that the Hamiltonian, and hence the ground-state $|\Psi_0\rangle$, are completely determined by $V_{\text{ext}}(\mathbf{r})$. The ground-state $|\Psi_0\rangle$ for this Hamiltonian gives rise to a ground-state electronic density $\rho_0(\mathbf{r})$. The exact ground-state electronic energy E_0 is the minimum value of the functional $E[\rho]$.
Further if n electrons move in an external potential $V_{ext}(\mathbf{r})$, the functional, that delivers the ground state energy of the system, gives the lowest energy if and only if the input density $\rho_0(\mathbf{r})$ is the true ground state density. The ground state energy can be obtained variationally: the density that minimizes the total energy is the exact ground state density.

However, these theorems do not tell us how to find good functional $F[\rho]$ and density $\rho_0(r)$ which obey the statements above. Approximate solutions are thus needed.

Kohn-Sham equations

Until now, we have presented a fictitious system of non-interacting electrons. To describe the system properly, one needs to include electronic exchange and correlation effects. The solution was proposed by Kohn and Sham [92]. They separeted $F[\rho]$ into 3 distinct parts so that equation 2.69 becomes:

$$E\left[\rho(\mathbf{r})\right] = T_s\left[\rho(\mathbf{r})\right] + \frac{1}{2}\int\int \frac{\rho(\mathbf{r})\rho(\mathbf{r}')}{|\mathbf{r}-\mathbf{r}'|} d\mathbf{r}d\mathbf{r}' + E_{XC}[\rho(\mathbf{r})] + \int \rho(\mathbf{r}) V_{\text{ext}}(\mathbf{r}) d\mathbf{r} \tag{2.71}$$

First and second part on RHS of Eq. 2.71 can be precisely calculated for a non interacting electron system. All non classical effects are included in the exchange-correlation part. We use the same variational procedure as explained in the Hartree-Fock section for the Hohenberg-Kohn density-functional, introducing a Lagrange multiplier λ to constrain the number of electrons to be n:

$$\frac{\delta}{\delta\rho(\mathbf{r})}\left[F[\rho] + \int \mathrm{d}\mathbf{r}\; V_{\text{ext}}(\mathbf{r})\rho(\mathbf{r}) - \lambda\left(\int \mathrm{d}\mathbf{r}\; \rho(\mathbf{r}) - n\right)\right] = 0. \tag{2.72}$$

with $F[\rho]$ being

$$F[\rho] = T\left[\rho(\mathbf{r})\right] + \frac{1}{2}\int\int \frac{\rho(\mathbf{r})\rho(\mathbf{r}')}{|\mathbf{r}-\mathbf{r}'|} d\mathbf{r}d\mathbf{r}' + E_{XC}[\rho(\mathbf{r})] \tag{2.73}$$

Here $T[\rho]$ represents the kinetic energy of a gas of non-interacting electron, the second term is so called Hartree energy or Coulomb term being just electron repulsion. The last term is the exchange correlation, which incorporates non-classical electron interaction and the difference between kinetic energies of interacting and the non-interacting electrons. The first two terms are dominant in the total energy and they can be easily calculated. Approximations are used to express the exchange-correlation part. Equation 2.72 can be rewritten:

$$\frac{\delta T[\rho]}{\delta\rho(\mathbf{r})} + V_{\text{KS}}(\mathbf{r}) = \lambda \tag{2.74}$$

in which the Kohn-Sham potential $V_{\text{KS}}(\mathbf{r})$ is given by

$$V_{\text{KS}}(\mathbf{r}) = \int \mathrm{d}\mathbf{r}' \frac{\rho(\mathbf{r}')}{|\mathbf{r}-\mathbf{r}'|} + V_{\text{xc}}(\mathbf{r}) + V_{\text{ext}}(\mathbf{r}) \tag{2.75}$$

and the exchange-correlation potential $V_{\text{xc}}(\mathbf{r})$ is

$$V_{\text{xc}}(\mathbf{r}) = \frac{\delta E_{\text{xc}}[\rho]}{\delta\rho(\mathbf{r})}. \tag{2.76}$$

To find the ground-state density $\rho_0(\mathbf{r})$ for this non-interacting system, we simply solve the one-electron Schrödinger equations obtained with variational procedure from Eq.2.72 in a Hartree-Fock style:

$$\left[-\tfrac{1}{2}\nabla^2 + V_{\text{KS}}(\mathbf{r})\right]\psi_a(\mathbf{r}) = \varepsilon_a\psi_a(\mathbf{r}) \tag{2.77}$$

for $\frac{1}{2}n$ single-particle states $|\psi_a\rangle$ with energies ε_a, constructing the density from

$$\rho(\mathbf{r}) = 2\sum_{i=1}^{n/2} |\psi_a(\mathbf{r})|^2 \tag{2.78}$$

the factor 2 comes from spin degeneracy. We assume the orbitals are singly-occupied and the non-interacting kinetic energy $T_\mathrm{s}[\rho]$ is written as:

$$T_\mathrm{s}[\rho] = -\sum_{i=1}^{n/2} \int \mathrm{d}\mathbf{r}\ \psi_a^*(\mathbf{r})\nabla^2\psi_a(\mathbf{r}). \tag{2.79}$$

Since the Kohn-Sham potential $V_\mathrm{KS}(\mathbf{r})$ depends upon the density $\rho(\mathbf{r})$, these equations are self-consistently solved. Starting with a guess for the form of the density, the Schrödinger equation is solved to obtain a set of orbitals $\{\psi_a(\mathbf{r})\}$ from which a new density is constructed, and the process is repeated until the input and output densities satisfy convergence criteria.
Kohn-Sham formulation of DFT is very close to Hartree-Fock theory. The main difference is the introduction of an exchange-correlation part including all quantum effects. This part is not necessarily "ab initio" and many empiric functionals have been developed. In the gas phase, the most popular is B3LYP functional [93, 94]. This functional is hybrid in the sense that a part of the Hartree-Fock exchange term is included.

Ab initio molecular dynamics

Chemistry and reactivity in molecular systems (electronic structure problematics) have been a subject of great interest since the beginning of quantum physics. In numerous studies, the system is treated in a static way and molecular structures are optimized using different appropriate methods in order to find the energy minima and the transition states. But to fully describe molecular systems, it is necessary to explore the configuration space i.e. to include dynamical effects. In the classical molecular mechanics, nuclei dynamics are well described but the intermolecular bonds are often constrained. The force fields which define the interactions are obtained either empirically or by fitting electronic structure calculations. Force field development is a tedious job. Moreover, atomic parameters generally are not transferable. This means that for each insertion of a new species in the modeled system, a new set of parameters has to be added. Also force fields are often described as pair interactions and subsequently many body effects such as polarization are not included.
The basic idea of AIMD is to keep the advantages of the two mentioned methods: to calculate energy (forces) with an electronic structure method and then propagate nuclei with one of the classical dynamics algorithms such as Verlet (see 2.1.4). The most famous implementation of this kind of method was proposed by Roberto Carr and Michele Parrinello in 1985 [95] and all methods of this family are often called "Carr-Parrinello dynamics" although there are many variations. Hereby I will present only Born-Oppenheimer molecular dynamics, which is implemented by default in the CP2K code. The description of other "flavors" of AIMD can be found in the literature [96, 97].

Born-Oppenheimer molecular dynamics

As already mentioned, we will assume that the potential energy function is calculated "on-the-fly" using DFT: $E[\Psi_a; R] = E_{KS}[\Psi_a[\rho(r)]; R] + E(R)$.

We introduce the Born-Oppenheimer Lagrangian (Eq. 2.80):

$$\mathcal{L} = \frac{1}{2} \sum_{A}^{\text{nuclei}} M_A \dot{\mathbf{R}}_A^2 - E\left[\{\psi_a\}, \{\mathbf{R}\}\right] + \sum_{i,j} \Lambda_{ij}(\langle\psi_i|\psi_j\rangle - \delta_{ij}) \tag{2.80}$$

Similarly to the procedure used for the classical Lagrangian (Eq.2.13), Euler-Lagrange equations of motion are used. In fact, the difference relies on the way to calculate the potential energy. The third term of equation 2.80 is added to preserve the orthonormality of wave functions. Inserting AIMD Lagrangian in Eq. 2.81, we obtain the following Eq. 2.82

$$\frac{\partial}{\partial t}\left(\frac{\partial \mathcal{L}}{\partial \dot{\mathbf{R}}_\mathbf{A}}\right) = \frac{\partial \mathcal{L}}{\partial \mathbf{R}_\mathbf{A}} \tag{2.81}$$

$$M_A \ddot{\mathbf{R}}_A = -\nabla_{\mathbf{R}I} E\left[\{\psi_a\}, \{\mathbf{R}\}|_{\langle\psi_i|\psi_j\rangle=\delta_{ij}}\right] \tag{2.82}$$

Once equations of motion are established and forces calculated, particles can be propagated as in classical dynamics. Fig. 2.11 is a presentation of the different steps in a AIMD simulation.

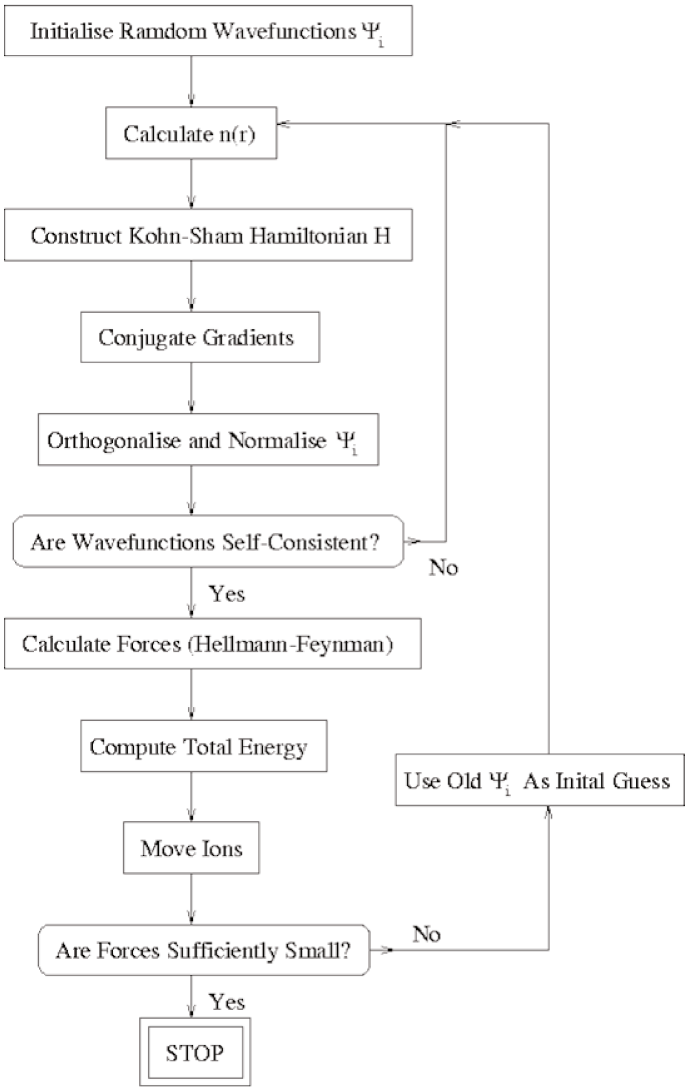

FIGURE 2.11: Block diagram representing main steps in a AIMD calculation. Picture adapted from [98].

2.2.3 QM/MM hybrid methods

Systems containing thousands of atoms and more (e.g. polymers, reactions in solution, molecules on surfaces) are hard to describe. In many applications, however, the main attention is on a small subset of atoms of the large system (reactive sites, the dissolved/adsorbed molecules). While the interaction of quantum part with molecular mechanics (MM) part cannot be neglected, one can often treat it by less computationally expensive models. The system is thus separated in two subsystems: the small part (QM) is quantum mechanically described and the remaining system (MM) is described classically. The pioneering idea of this hybrid QM/MM approach was recognized by the 2013 Nobel Prize in Chemistry, awarded to A. Warshel, M. Levitt and A. Karplus for "the development of multiscale models for complex chemical systems".

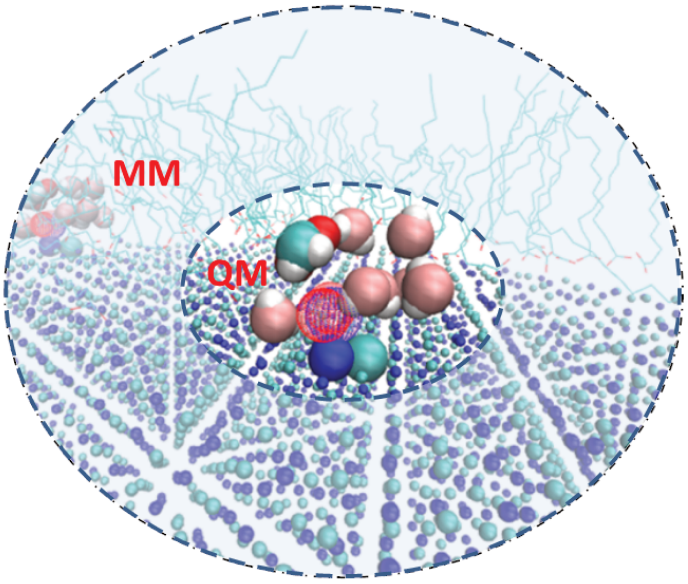

FIGURE 2.12: Illustration of Hybrid QM/MM system where one part is treated quantum mechanically.

The hamiltonian of extended QM/MM system consist of 3 parts:

$$\hat{H}(\mathbf{r}_\alpha, \mathbf{r}_a) = \hat{H}_{\mathrm{QM}}(\mathbf{r}_\alpha) + \hat{H}_{\mathrm{MM}}(\mathbf{r}_a) + \hat{H}_{\mathrm{QM/MM}}(\mathbf{r}_\alpha, \mathbf{r}_a) \tag{2.83}$$

$\mathbf{r}_\alpha$ and $\mathbf{r_a}$ are coordinates of QM nuclei and MM atoms, respectively. The first term is the quantum part of the system described in section 2.2, in the electronic ground state. The second describes the classical part of the system, with classical interactions such as defined in section 2.1.2. The third term is problematic and not trivial to calculate. There are different schemes introduced to calculate the interaction between QM and MM parts. One of the first proposed was mechanical embedding. In this scheme, the interactions of QM with MM part is described by van der Wals interactions and classical point charges [99]. Thereby, only isolated effects of geometrical structure are accounted by this way. The main drawback of this implementation is that polarization effects of MM part on QM are not included. Polarization in reactive processes is nevertheless important and then for the work presented in this thesis electrostatic embedding has been used. The electrostatic coupling implementation in CP2K are already explained in the publication of Laino and co-workers [100]. The interaction between the QM and MM subsystems can be expressed as:

$$\hat{H}_{\mathrm{QM/MM}}(\mathbf{r}_\alpha, \mathbf{r}_a) = \sum_{a,\alpha} q_a \int \frac{\rho(\mathbf{r}, \mathbf{r}_\alpha)}{\mathbf{r} - \mathbf{r}_a} dr + \sum_{a,\alpha} V_{vdw}(\mathbf{r}_\alpha, \mathbf{r}_a) \tag{2.84}$$

where $\mathbf{r}_\alpha, \mathbf{r_a}$ and $\mathbf{r}$ are coordinates of QM nuclei, MM atoms and electrons, respectively. The first part of equation 2.84 corresponds to the coupling between classical point charges and quantum described electronic clouds. The second part is a parametrized van der Wals interaction.

The corresponding Lagrangian for this QM/MM approach is written as:

$$\mathcal{L}(\mathbf{r}_a, \mathbf{r}_\alpha) = \frac{1}{2}\sum_{a}^{MM-nuclei} M_a\vec{\mathbf{r}}_a + \frac{1}{2}\sum_{\alpha}^{QM-nuclei} M_\alpha\vec{\mathbf{r}}_\alpha - E^{MM}(\mathbf{r}_a) - E^{QM/MM}(\mathbf{r}_\alpha, \mathbf{r}_a) - \\ - E^{QM}(\mathbf{r}_\alpha) + \sum_{i,j}\Lambda_{i,j}(<\psi_i|\psi_j> - \delta_{i,j}) \tag{2.85}$$

Eq. 2.85 is the extended AIMD-BO Lagrangian. Equations of motion are obtained using already explained procedure of applying Euler-Lagrange equations.

Chapter 3

Coating of NaCl by palmitic acid. Influence of humidity

The work presented in this chapter has been done in the context of the Labex CaPPA (Chemical and Physical Properties of atmosphere). It promotes cooperation between experimentalists and theoreticians working in the field of aerosols, to investigate their properties and their impact on the atmosphere. The present work was strongly inspired by the experiments conducted in the group of Sophie Sobanska from the "Laboratoire de Spectrochimie Infrarouge et Raman" (LASIR) and Denis Petiprez from the "Laboratoire de Physico-Chimie des Processus de Combustion et de l'Atmosphère" (PC2A), especially publications [19] and [101]. During the last decade, the research on aerosols has focused on organic aerosols. As already mentioned in Chapter 1, organic matter is a significant fraction of marine aerosols particles [14, 102]. These aerosols are heterogeneous, complex and therefore represent a challenge for thereoticians to model them. Salt (NaCl) particles covered with organic molecules represent a model system and a first step toward more complex systems.
Fig. 3.1 describes how the organic fraction can influence the properties of the aerosols, such as deliquescence for instance. Deliquescence is the process by which a substance (here NaCl) absorbs water from the atmosphere until it becomes a solution. Efflorescence is the reverse mechanism. On Fig. 3.1, it is visible that organic molecules are changing the deliquescence and efflorescence properties of NaCl surfaces. The uptake properties of aerosols change dramatically the state, solution/solid, of the particle with respect to pure NaCl particles. Minambres et al. [34] have studied the effect of the organic molecule chain length. The smaller molecules are in nature more hydrophilic whereas longer ones (with 8 or more carbons) tend to be hydrophobic. Due to the FA-FA and the FA-ions interactions, organic acids with long chains form easily Self Assembled Monolayer (SAM) on the ionic substrate [103]. These SAMs, compactly packed, can prevent water uptake on the salt surface. This can be clearly seen on Fig. 3.1, in the case of lauric acid (12 carbons), the fraction of the surface covered with water does not change even with increasing the relative humidity (RH). Due to the heterogeneous nature of these aerosols, it is a complex task to estimate the hydrophilic properties of these aerosols. These effects are usually on a nanometer scale which is often difficult to experimentally investigate and the need for a theoretical modeling at the molecular level appears evident.

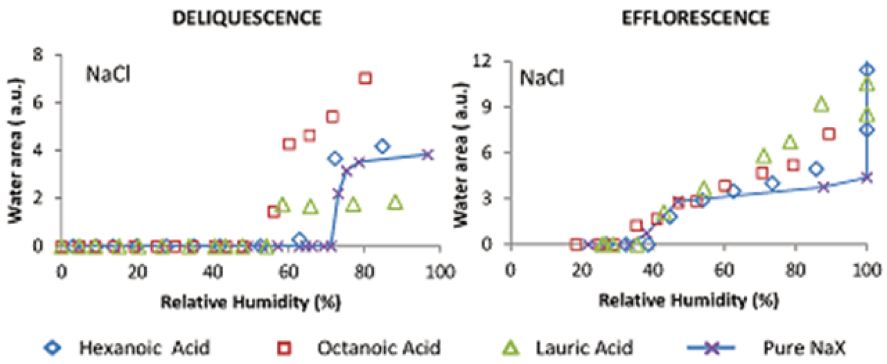

FIGURE 3.1: Deliquescence and efflorescence curves for NaCl particles covered with organic acids. The curves obtained for pure inorganic salts are shown by lines. Figure taken from [34].

3.1 Palmitic acid self-assembled monolayers on NaCl

Self-assembled monolayers attracted the scientific community in the past decades because of the possible applications in the industry and their ubiquitous appearance in biological systems [104]. Due to the biological nature [35] of some aerosol sources (phytoplancton degradation...), the problematic of SAMs appears naturally in the context of our studies. The goal of this thesis is not to focus on SAM formation, this is why I choose not to distract the reader from the atmospheric context. Information on SAMs can be found in the scientific literature [105, 106, 107, 108, 109, 110].

We have performed molecular simulations to study the influence of coverage and temperature on some structural properties of palmitic acid self-assembled monolayers on NaCl (100) surfaces.

3.1.1 Computational details

The GROMACS package [69], well adapted for parallel computing, has been employed to perform MD simulations. The equations of motion are integrated using the leap-frog algorithm [76]. The short range interactions are tuncated with a cut off of 1.4 nm. Long range electrostatic interactions are treated with the Particle Mesh Ewald (PME) method. All bonds are constrained, including light hydrogen atom with short period of oscillations, using the LINCS [111] algorithm, making possible the use of a 2 fs time step for the simulation. The NaCl crystal is built by placing the Na and Cl atoms in a fcc crystal with a lattice constant of 0.56 nm corresponding to the experimental value [112]. After a minimization with the steepest descent algorithm and a short relaxation (100 ps) in the NVT ensemble at 235 K, the lattice parameter of the crystal converged to 0.54 nm. The crystal is then equilibrated in the NPT ensemble at T=235 K during 150 ps giving a final crystal lattice equal to 0.56 nm.
Laboratory measurements on a similar system [19] indicate that PA creates SAM on NaCl. The initial configurations have been chosen with the PA functional group pointing toward the surface while having the chains

aligned perpendicularly to the substrate. The PAs are distributed over a rectangular grid, as illustrated on Fig. 3.2. Several PA coverages were produced likewise by increasing the size of the grid. The number of PA molecules can also be expressed in terms of surface coverage. We can suppose that the COOH group of a PA molecule will adsorb preferentially on top of a NaCl pair with the tail aligned perpendicularly to the surface. Since the modeled NaCl sublayer is composed of 200 Na^+ - Cl^- ion pairs, 200 PA molecules would correspond to a full Theoretical Monolayer (TM). In the following paragraphs, the PA coverage will thus be expressed with respect to the full TM. The size of simulation box is 5.5x5.5x20 nm. MD productions, with a duration of 5 ns for all cases, are performed in NPT ensemble with temperature maintained by the V-rescale [113] algorithm and pressure coupled to 1 bar by the Berendsen barostat [83]. Standard periodic boundary conditions are applied.

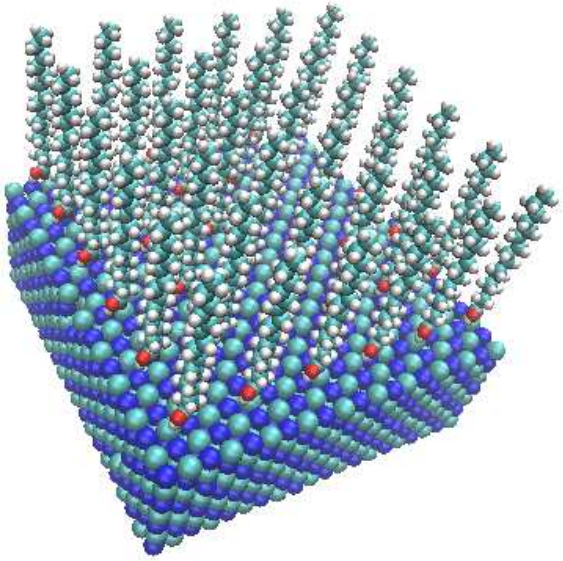

FIGURE 3.2: Initial configuration, PA molecules arranged in a 6x6 grid which corresponds to 18% TM. PA molecules are initially placed 0.3 nm above the surface.

The palmitic acid (PA) molecule is modeled by the "All-Atom OPLS" force field [74] which is reported to be well adapted for organic molecules [75]. Different force fields [114] are used for the description of Na and Cl atoms. All of them reproduce well a stable crystal. Among those, the force field developed by Smith and Dang [115] has been chosen because it gives a lattice parameter close to the experimental value [114] (Fig. 3.3 a).

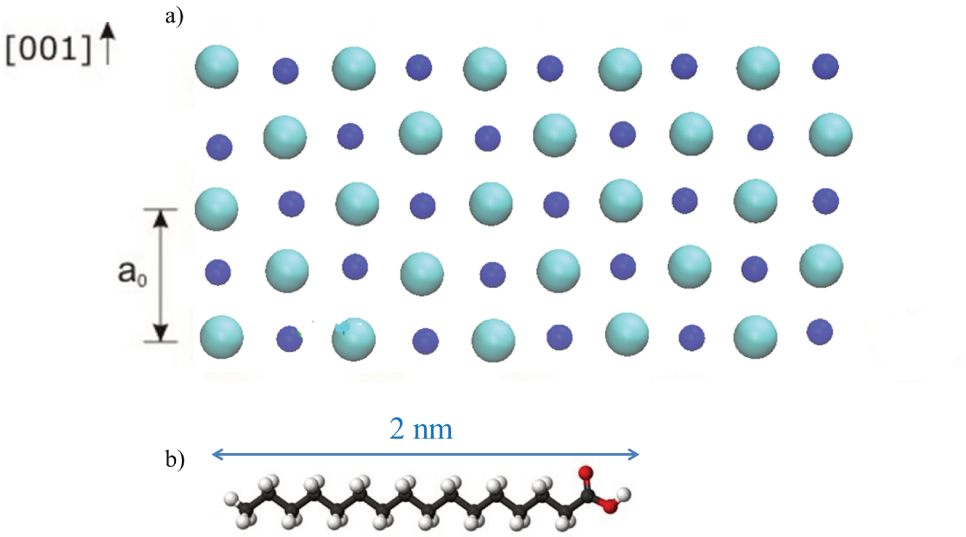

FIGURE 3.3: (a) NaCl (100) surface. Cell parameter $a_0 = 0.56nm$. Cl and Na atoms are represented in yellow and green respectively. (b) Palmitic acid molecule.

3.1.2 Effect of coverage: evidence for a phase transition

The structure of the PA film on NaCl(100) is characterized here in terms of orientation distribution. The tilt angle Θ is defined as the angle between the surface normal and the molecular axis defined as the C1-C16 direction. The distributions averaged at each time step during the production run (3 ns) are represented for the various coverages on Fig. 3.4 at T=300 K. The low coverage distributions are characterized with a large tilt angle, corresponding to a "flat" orientation and a rather broad distribution. The latter feature is an indication of the disorder in the organic matter adsorbed on the NaCl surface, due to the insufficient density to form SAM. Molecules are lying on the surface with tilt angles around $65°$ and $75°$ for coverages of 25% and 18% respectively. The broad distributions are typical of a liquid-like structure on surface. By increasing the PA coverage, the tilt angles decrease, the molecular axis get closer to the normal and the molecules are packing in a SAM-like structure. At low coverage, a small increase of the coverage induces an important change in the tilt angle, whereas around 40%, the tilt angle shows only small variations (Fig. 3.4). Stabilization of the tilt angle around 40% TM is an interesting behaviour which could indicate that the PA chains in SAM have a preferred orientation.

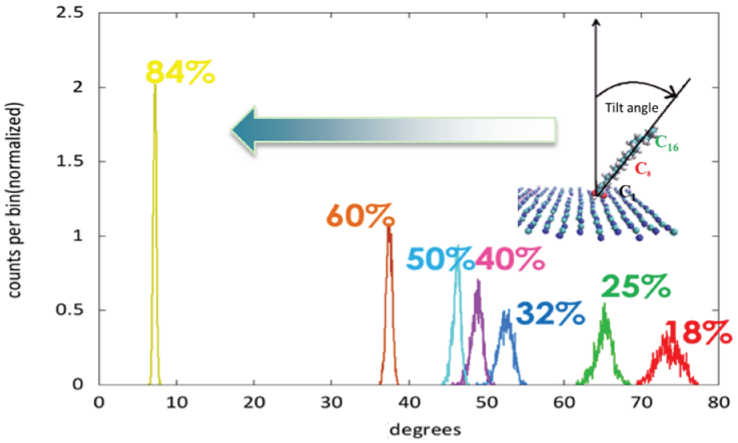

FIGURE 3.4: Distribution of angles averaged at each time step at T = 300 K. Each color corresponds to a different coverage, from 18% to 84%. In the upper right corner, a cartoon recalls how the tilt angle is defined.

An other way to investigate this problem is to look at the distribution of all tilt angles during the simulation (Fig. 3.5). The distributions of tilt angles for the C1-C8 or C1-C16 axis are shown on Fig. 3.5. For both definitions of the molecular axis, at low coverages (< 40 %), two preferential orientations can be noticed: 90° and 40°. The peak around 90° corresponds to molecules lying flat on the surface, while the one at 40° corresponds to tilted molecules. An increase of the coverage results in an increase of the peak at 40°. The differences between the C1-C8 and C1-C16 distributions are indicative of molecules folding, as it is observed at low coverages. By contrast to the highest coverage, the distributions are superimposed, revealing that we obtain packed molecules with almost perfect all-trans configurations.

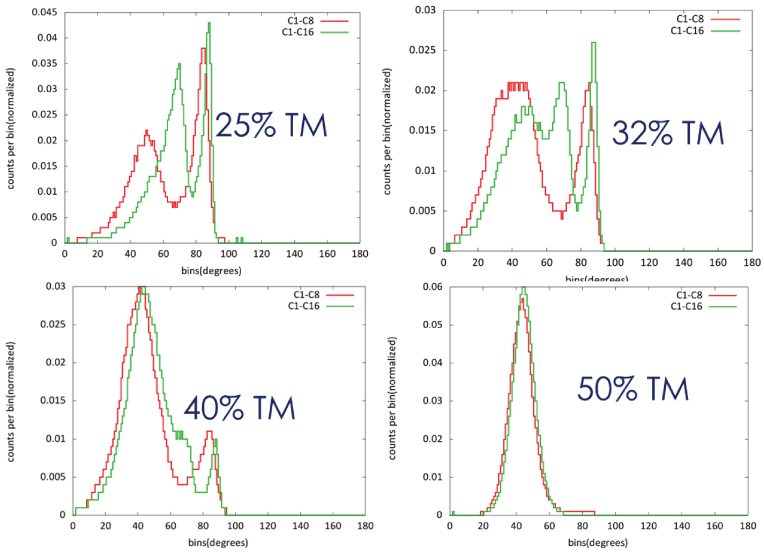

FIGURE 3.5: Distribution of all non averaged angles extracted from the trajectory for different coverages at T= 300K. The green and red lines correspond to the angle between the C1-C16 axis or C1-C8 axis respectively and the surface normal.

On Fig. 3.6, we have represented the average angle as a function of the PA coverage. The curve is characterized by a plateau between 30° and 50° (marked with a blue circle), sign of a discontinuity in the variation of the tilt angle as a function PA coverage. This is a characteristic behaviour of a phase transition [116, 117]. Note that a detailed thermodynamical study would be necessary to fully characterize this phase transition.

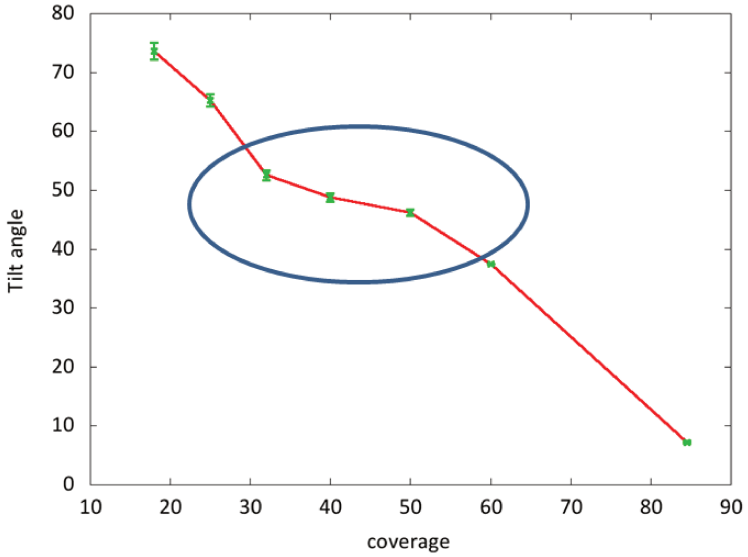

FIGURE 3.6: Green points correspond to averaged tilt angle at each coverage. The green bar indicated corresponds to the width of the distribution. Red line is a connection between the points used to emphasize the trend

One of the advantages of MD simulation is that we can have insights on the interactions at the molecular or atomic level. Fig. 3.7 shows a distribution of the intermolecular interaction energies between one PA molecule and all others PA molecules. This distribution gives us an information about the packing of the PA molecules. For the low coverages (< 40%), the distribution is broad and asymmetric while for higher coverages, the distribution shifts to lower (negative) values and the distribution is getting narrower and more symmetric. If we look more carefully at the intermediate coverages, 32% and 40 %, two peaks can be noticed which likely corresponds to two different PAs orientations, flat and tilted, evidenced on Fig. 3.5. At larger coverage, the interactions are stronger due to the packing of the molecules in SAM. These conclusions are consistent with the previous results relative to the orientation of the chains.

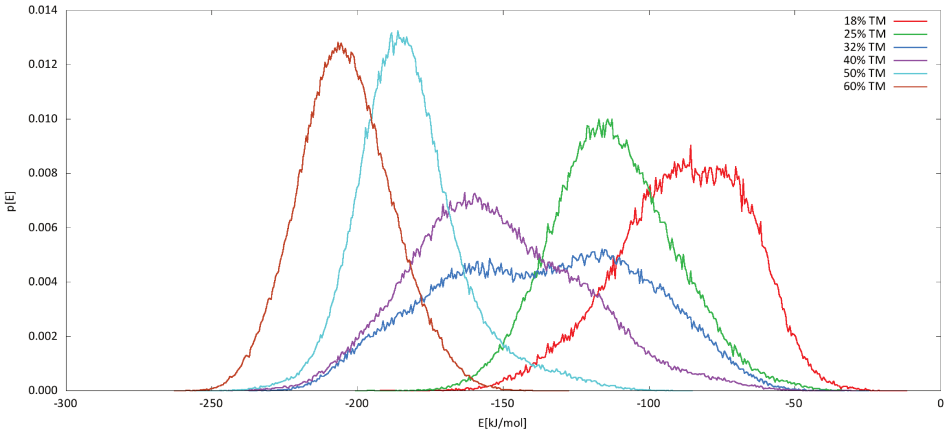

FIGURE 3.7: PA-PA energy distribution for different PA coverages at T= 300 K.

In their experiments, Sobanska and co-workers [19] used stearic acid (SA) as a proxy molecule. The main difference with PA is that SA has 2 carbons more but their physical properties are not significantly different. Fig. 3.8 a) is an Atomic Force Microscope (AFM) image of SA vapor deposited on a NaCl substrate. The phase image (purple) is superimposed on the morphologic image (orange). SA monolayer islands of 2–3 nm thickness are located on flat terraces separated by regular steps (0.4 nm) of freshly cleaved NaCl crystals. The thickness of 2-3 nm corresponds approximately to the length of one SA molecule. Raman spectroscopy has been also performed, revealing SAM like structure of SA on NaCl. It is then reasonable to conclude that our MD simulations match qualitatively with the experimental results. Part b) of Fig. 3.8 corresponds to the Time-of-Flight Secondary Ion Mass Spectrometry (ToF-SIMS) image. This image exhibits some areas with high coverage and some other with lower, i.e. an heterogeneous surface coating and then with different properties. Disordered, "spaghetti"-like structures obtained at low coverage in this work, would likely be less surface protective than SAM-like structures.

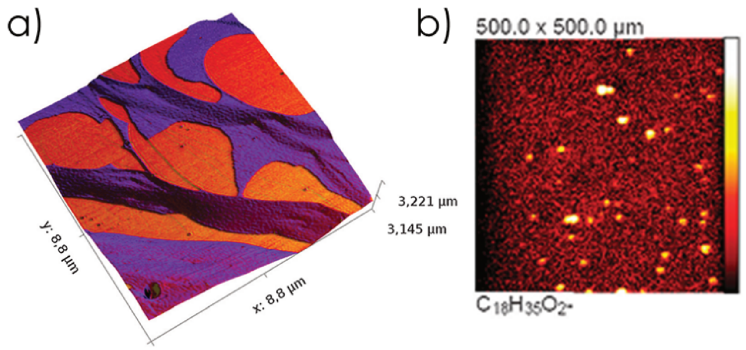

FIGURE 3.8: a) AFM image of the NaCl(100) surface coated by stearic acid (SA). SA is represented in purple color and NaCl in orange. b) ToF−SIMS image of $C_{18}H_{35}O_2^-$ mass peaks. Figure extracted from [19].

3.1.3 Influence of the temperature

To study the effects of the temperature on the structure and phase transition of the monolayers, three different coverages have been chosen: 50 %, 60 % and 100 %. Temperatures ranging from 10 to 365 K have been investigated. The initial configuration for each temperature is taken from an equilibrated simulation at T = 300 K. These results have some important implications for the atmospheric context, especially for cloud condensation. Indeed, the hygroscopic properties of particles are changing dramatically when the organic aerosol is passing from solid to liquid and vice versa.

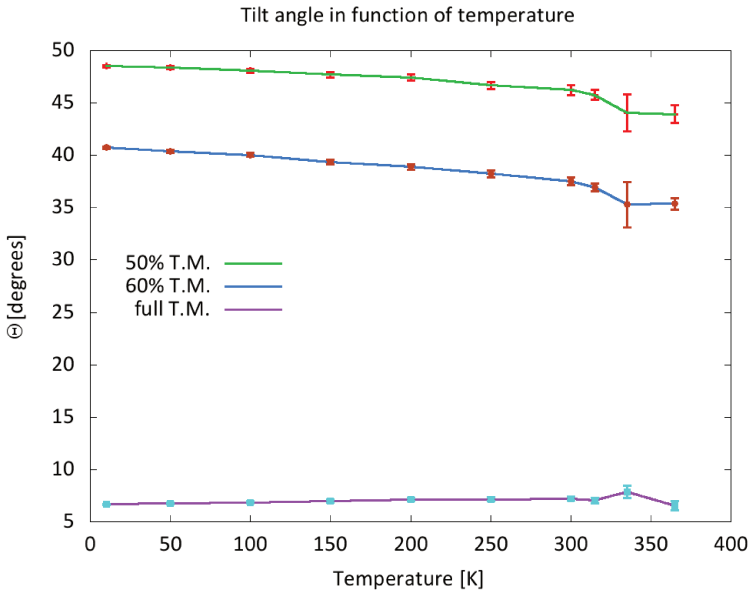

FIGURE 3.9: Average tilt angle as a function of temperature for the 3 coverages. Red bars correspond to the associated width of the distribution.

Tilt angle variation as a function of temperature is shown on Fig. 3.9 for the three coverages. Around 335 K, the orientation of the PA chains in

the monolayers undergo a huge change associated with large width of distribution. This is an indication of melting of the surface monolayer. Note that the bulk melting temperature of PA is known to be 335.9 K [118], close to our estimation. Temperature of 335 K is too high to be considered of atmospheric interest but this study can be used as a model for other organic molecules. For example, hexanoic acid has a melting point at ∼300 K and could be a system of atmospheric interest.
At full coverage, the molecules are really packed and additional thermal energy in the system affects only slightly the orientation of the chains. We can notice a smooth increase of the tilt angle with temperature, while at lower coverages, an opposite behaviour is reported. Similar behaviour has been reported for SAM on metals. For example, Fig. 3.10 shows the potential energy curve as a function of tilt angle, for Alkylthiolates on Au(111) and Ag(111) [119] surfaces respectively. If we put thermal energy in the system (kT), the evolution of tilt angle will be different depending on the potential energy surface (PES) curvature and thus on the susbtrate. In our system, for low coverage, as temperature increases, the molecules are close to the normal as for C_n/Au(111) while at larger coverage it is the reverse situation in a less pronounced manner.

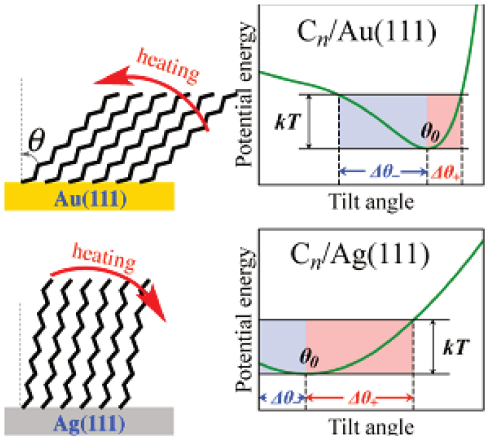

FIGURE 3.10: Alkylthiolates SAM orientation on different metal surfaces. Potential energy curve as a function of the tilt angle. Figure taken from [119]

We can summarize the results of this study as follows: we have found a clear dependence of the structural properties, namely the orientation of the chains, on both coverage and temperature. Low coverage shows a liquid-like behaviour with broad angle distribution. For higher coverage, a structured organization is observed. Inverse temperature behaviour was observed for low and high coverage.

3.2 Heterogeneous coating of palmitic acid on NaCl induced by humidity: atmospheric implications

Details concerning this part can be found in the recently published paper [103] (Appendix C). Here I will summarize the major results. Useful informations and related references can be found in its bibliography [103].
Few MD calculations have been performed to model sea salt particles with

organic molecules [43, 44, 45, 46, 47, 48, 120]. Previous studies have mostly focused on Langmuir monolayers at the air - water interface [44, 46], on water droplets [45, 47], nanoparticles [48] or in ionic solutions. For instance, Chakraborty and Zachariah [47] have investigated the effect of fatty acids, especially of their chain length, on the morphology and properties of water nanodroplets coated with these organics. Their results indicate that, for particles coated with long surfactants, the fatty acid chains tend to align parallel to each other, lowering the sticking coefficient of water vapor on such particles, whereas particles coated with shorter chains are more hydrophilic. Moreover, Takahama and Russell [46] have simulated impinging water vapor molecules on a slab of bare water and a slab of water coated by monomolecular organic films. The mechanism of sticking is shown to depend on the compound, packing density, and resulting surface structure. In addition, MD simulations of water vapor interacting with Sodium Dodecyl Sulfate (SDS)/NaCl slabs [48] indicate that SDS kinetically hinders the initial water uptake partly due to the ordering of the SDS chains as the coverage increases. Most of the studies have focused on the effect of a full organic coated water slab or a nanodroplet on the sticking of incoming water molecules. As a complement to these studies, the purpose of the present study is to understand the effect of humidity on the organization of the coating for a partial coverage of the salt surface. There are many experimental groups working on aerosol modelization and investigation of physical-chemical properties. As previously mentioned, the work developed in this thesis was mainly motivated by the discussions with Sobanska and co-workers and their publication [19]. In this paper, attention was paid on the influence of an organic coating on the reactivity of NO_2 with NaCl under humid conditions. The studies in the Minambres group [34] deal with the impact of the organic fraction on sodium halide aerosols hygroscopic properties. In both cases, the effect of humidity on aerosol properties is evident. Since we deal with heterogeneous aerosol, some kind of interplay driven by water will occur. It is well known that water tends to create monolayers on salt surface [121], organic molecules such as fatty acids are amphiphile, i.e.with one part being hydrophobic and the other hydrophilic. These two properties lead to interesting phenomena. Indeed islands of organics on NaCl were reported in S. Sobanska publication as a consequence of water mediated interactions. Their results are well supported by our MD results. Similar conclusions can be drawn from Minambres and coworkers publication [34]. Indeed, the hygroscopic properties are changing with different organic fraction on surfaces (Fig. 3.1). It appears that carboxylic acids with 8 or more carbons tend to be hydrophobic. Generally, bigger molecules tend to form easily SAM. In the case of lauric acid (C12), water uptake on NaCl is constant despite of increasing humidity. This leads to the conclusion that lauric acid could also form island-like structures in closely packed groups "protecting" the surface as evidenced for SA and PA molecules. Smaller molecules do not exhibit such a behaviour.

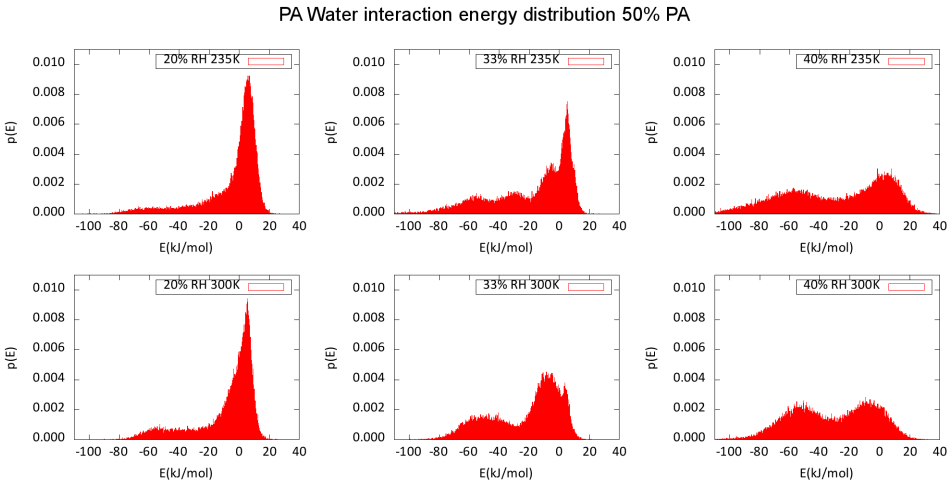

FIGURE 3.11: Distribution of PA-water interaction energy at 235 K, 300 K and 20%, 33% and 40% RH. PA coverage is 50% TM.

Energy distributions between one PA molecule and surrounding water are displayed on Fig. 3.11. These distributions are calculated for two temperatures, 235 K and 300 K. The higher temperature corresponds to laboratory conditions whereas the lower is more representative of the atmospheric conditions (high troposphere). Three different humidity conditions are also explored. When increasing humidity, the peak corresponding to positive energy interaction, i.e. repulsive, is decreasing and the formation of hydrogen bonds between water and PA is observed.

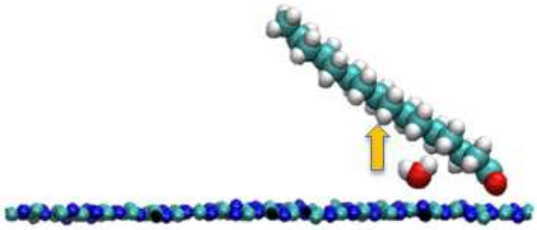

FIGURE 3.12: Snapshot extracted from simulation. Only one PA and one water molecule are shown. Other PA, water and NaCl molecules are omitted in order to emphasize the repulsive nature of water-PA tail interaction under low humidity.

Fig. 3.12 represents a snapshot of the fragment taken from one of the simulations. The goal is to show how water molecule, adsorbed on the surface surface, interacts with the PA chain. This situation is dominant under low humidity conditions and corresponds to positive energy part distribution for low humidity (Fig. 3.11). When the water quantity becomes important, repulsive interactions are sufficiently strong to pack PA molecules in

ordered island structures.

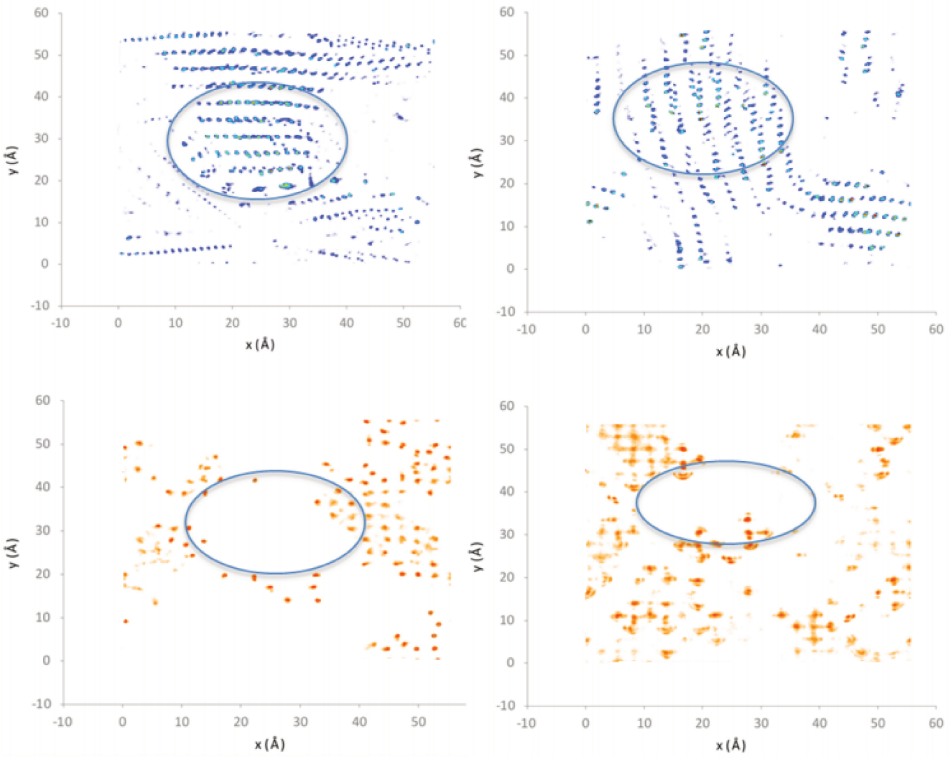

FIGURE 3.13: Results for 33% RH and 50% PA coverage. *Upper panel*: densities of PA C1 carbon (COOH group) at 235 K (left) and 300 K (right). *Lower panel*: densities of water oxygen at 235 K (left) and 300 K (right). The more intense and well defined the dot is, the higher is the probability of having the atoms in this position. In all panels, circles are added to highlight areas with PA islands formation and absence of water.

Fig. 3.13 is an histogram of projected carbon densities on x-y plane. The most intense color represents the most probable positions. From the plot, we can notice that correlation of water and PA probability is rather negative. This is a clear evidence of island formation, as obtained in the experiments [19].

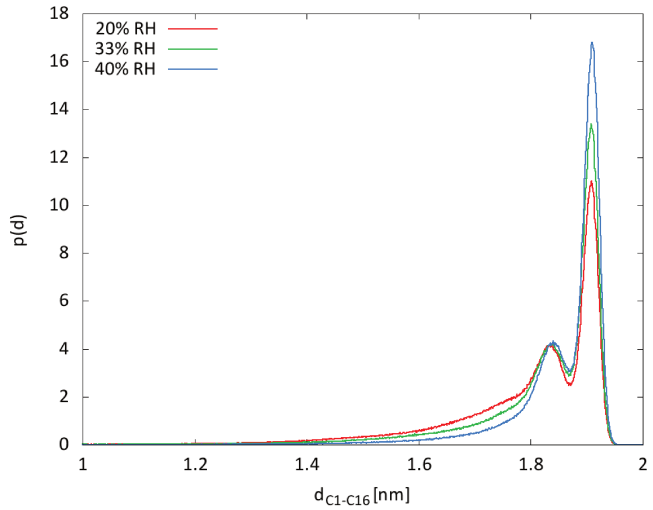

FIGURE 3.14: PA tail length distribution under RH of 20%, 33% and 40%.

The features previously discussed are connected with 2D geometrical properties on the x-y plane. To investigate the 3D arrangements of the adsorbate, the length of PA tails (C_1-C_{16} distance) is monitored during simulations with different humidities. Looking at Fig. 3.14, it is evident that the peak corresponding to 1.9 nm becomes more important when humidity increases. This value corresponds to the optimized linear PA molecule. A 2 nm cover of stearic acid on NaCl crystal is observed also experimentally using Atomic Force Microscope (Fig. 3.8) which supports our results.

To summarize the main results of these studies, we can draw the following conclusions:

1. Molecular modeling of heterogeneous organic aerosol provides detailed informations on the mechanisms and contributes to an improved understanding of cloud nucleation.

2. Classical Molecular Dynamics simulations were employed to model palmitic acid organization on a model sea salt surface, NaCl, at different temperatures and humidity conditions. Humidity is shown to have a significant influence on the fatty acids self-assembling.

3. Present calculations provide evidence for ordered PA islands formation under the humid condition as observed experimentally [19].

4. The coating is driven by water that provides order to the FA islands and binds preferentially to the salt. As a consequence some area of the salt may be covered by water only.

The implication of the organisation of this organic film for the reactivity of the aerosol particle, especially the reactivity of NO_2 with NaCl will be discussed in next chapter.

Chapter 4

QM/MM study of NO_2 reactivity on heterogeneous aerosols

4.1 Context of the study

NO_2 or more generally NO_x (NO and NO_2) are believed to be among the most important atmospheric trace gases because of their impact on health and ecosystems [7]. As precursors to tropospheric ozone, NO_x are responsible for respiratory problems. During the daytime, NO_2 can photolyze to $NO + O$. This atomic oxygen reacts with molecular oxygen leading to ozone creation (Fig 4.2). Main sources are road traffic, energy production and other combustion processes. Figure 4.1 shows the simplified formation mechanisms involving NO_2. NO_x are involved in the ozone cycle through photolyzed reactions (Fig. 4.2). They also contribute to acid rain formation by participating in the reaction: $2\,NO_2 + H_2O \longrightarrow HONO + HNO_3$. Reactions of NO_3 and NO_2 also result in the production of N_2O_5 which is an important source of nitric acid in the atmosphere. In polluted environments, NO_2 can be generated from the reaction of OH and NO with volatile organic compounds [16, 18, 122]. NO_2 is also implied in heterogeneous chemical processes at the surface of aerosol particles. The goal of the present study is to study NO_2 chemistry on a sea salt aerosol modeled by a NaCl surface.

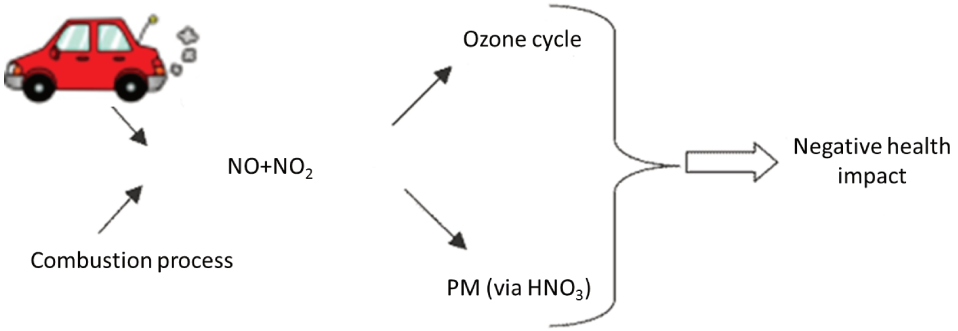

FIGURE 4.1: Simplified relationships of nitrogen oxides emissions with formation of NO_2 and other harmful products including ozone cycle and other particulate matter (PM) [122]

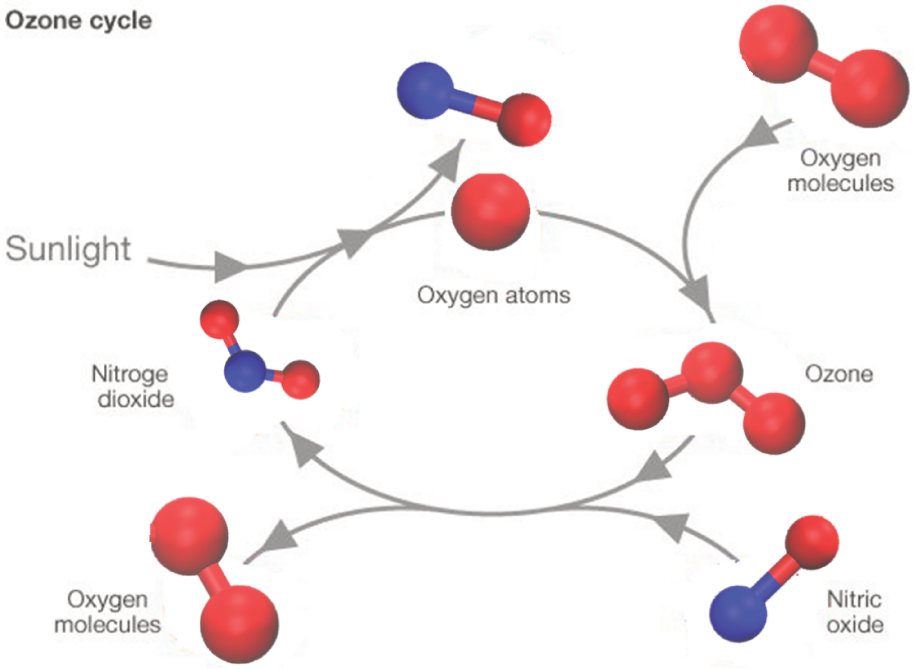

FIGURE 4.2: NO_2-ozone cycle in the troposphere. The sunlight initiates this process and induces the dissociation of NO_2 to NO and O, then oxygen atom reacts with di-oxygen and forms the ozone followed by ozone destruction by nitric oxide. Di-oxygen and NO_2 are then regenerated.

Fig. 4.3 represents the worldwide NO_2 concentration. This concentration is obviously correlated with the density of human population.

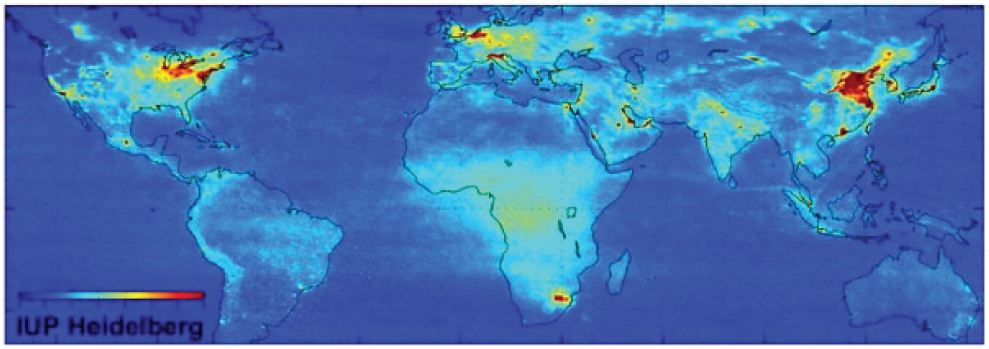

FIGURE 4.3: Worldwide NO_x concentration. Source: European Space Agency (www.esa.int/esaCP/ Credits: University of Heidelberg).

4.2 Background

Because of its tendency to form a dimer in the gas phase, reactions are supposed to occur through the NO_2 dimer rather than the monomer. The isomerization of NO_2 dimer at aerosol surfaces is found to be a major source

of OH radicals in the atmosphere. NO_2 is a proxy for $HONO$ formation, $HONO$ being a dominant source [123] of OH radicals in atmosphere. In the presence of water, the cis asymmetric isomer is ionized [124]. This ionization occurs immediately. The mechanisms of the reaction involving NO_2 have been extensively studied either in the gas phase (theoretically in the Goddard group) [125] or on different surfaces. Reactivity at the NaCl surface was experimentally studied in the Sobanska group [19] and theoretically by Zhang and co-workers [126]. Other studies mostly dealt with NO_2 on water clusters [127, 128, 129, 130] and metal surface [131].

A combined Atomic Force Microscope (AFM) and micro Raman spectroscopy experiment performed by Sobanska and co-workers [19] showed the formation of $NaNO_3$ on a NaCl surface covered with stearic acid under humid condition and exposed to NO_2 molecules. They proposed, without being able to fully characterize it, the following reaction scheme:

$$NaCl(s) + 2\,NO_2 \longrightarrow NaNO_3(s) + NOCl(g) \quad (1)$$

that can be written in two steps:

$$2\,NO_2 + H_2O \longrightarrow HONO + HNO_3 \quad (2)$$

$$HNO_3 + NaCl \longrightarrow NaNO_3 + HCl \quad (3)$$

This experimental result provides evidence for a surface catalyzed reaction since numerous studies have shown that reaction (1) is negligible in the gas phase [123, 132].

In their recent study [126], Zhang and co-workers have investigated, by density functional theory calculations, the adsorption sites of NO_2 (monomer) on a NaCl surface using the Perdew–Wang 1991 (PW91) functional combined with a plane wave calculation approach (cutoff at 330 ev). They also considered the formation of NO_2 dimer and the hydrolysis to nitric and nitrous acid. Firstly, they adsorb the NO_2 monomer on the salt surface. This starting hypothesis is questionable since it is admitted that NO_2 easily forms the symmetric dimer in gas phase [123, 125]. Surprisingly, they found that the activation energy between the symmetric and the trans-dimer on NaCl surface is higher than in gas phase [125] (51.84 kcal/mol vs 47.2 kcal/mol). Method and basis set used in these two studies are not the same but the result is still surprising and in contradiction with previous studies. Finlayson-Pitts et al. [123] proposed that, on a silica surface, the symmetric dimer is first transformed to cis or trans isomer and that from these states, fast dissociation forming NO_3^- and NO^+, occurs at the surface (Fig. 4.4). This idea has already been used in other studies [130, 133] and NO_2 auto-isomerization may also occur on other surfaces. In addition, previous AIMD studies on small water clusters showed that the dimer dissociation is influenced by the number of water molecules [134]. The role played by water is not clearly characterized in Zhang's work [126] since the process is modeled using just one water molecule. A better understating of the surface and humidity effects on the dimer dissosiation is thus required. The goal of the present study is to characterize the influence of a model aerosol surface, dry or wet, on the ionization of the $cis-NO_2$ dimer. Hereby, I have carried out AIMD QM/MM calculations of the NO_2-dimer dissociation on a NaCl surface under humid and dry conditions.

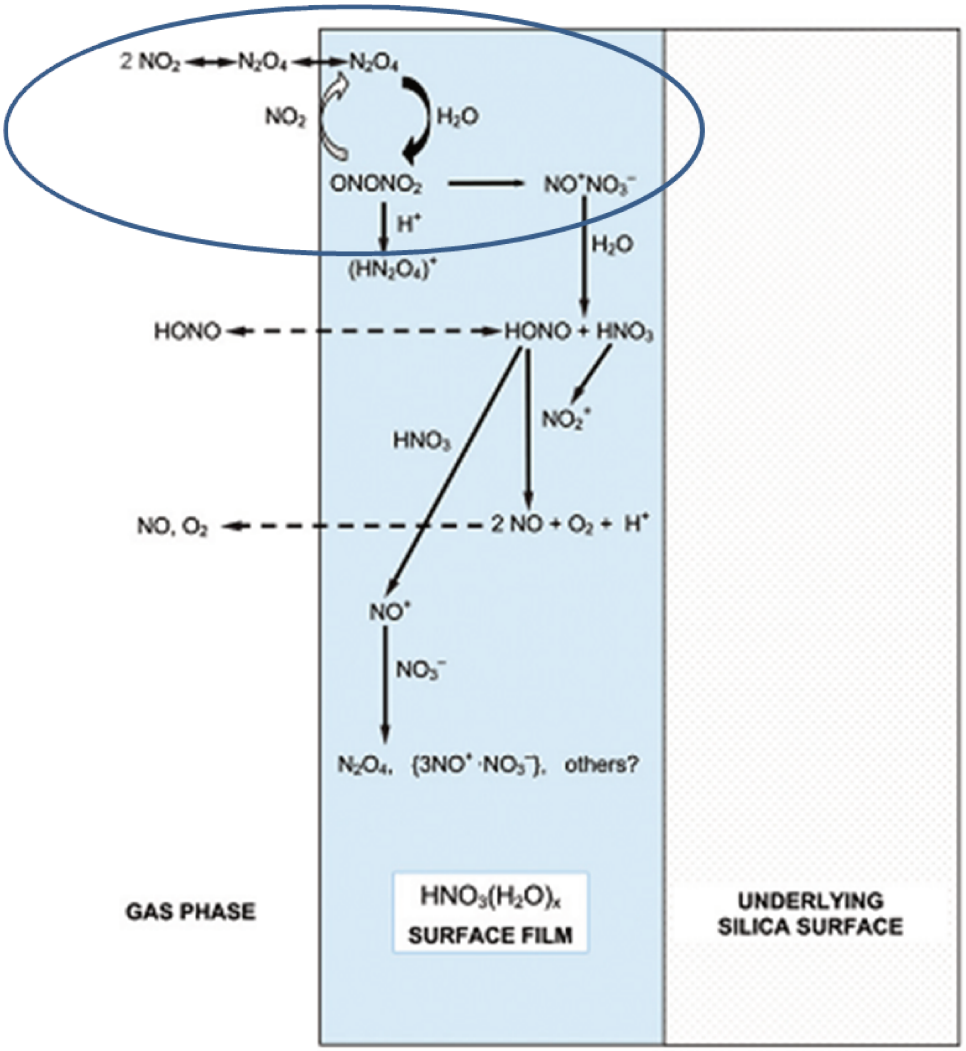

FIGURE 4.4: Scheme representing the chain of reactions implying NO_x at a silica surface [123].

4.3 Simulation details and benchmark of the functional

The simulations reported here are obtained with the open source CP2K suite of programs [70]. CP2K was chosen because of its versatility, indeed "dynamic" and "ab initio" modules are implemented in one code. This makes possible to perform AIMD and QM/MM calculations more efficiently. A drawback of this decision is that I am pioneer in my group in using this code. I had to learn how to use this program and since the code itself is not a "black box", a first validation of our results is required.

To start, the method (functional and basis set) used is benchmarked with reference to values of the litterature. The group of Goddard [125] has performed extensive theoretical work with high level quantum calculations on the gas phase conformers of the NO_2 dimer. The different isomerization pathways have been characterized including transition states and stable conformers. (Fig. 4.5 a).

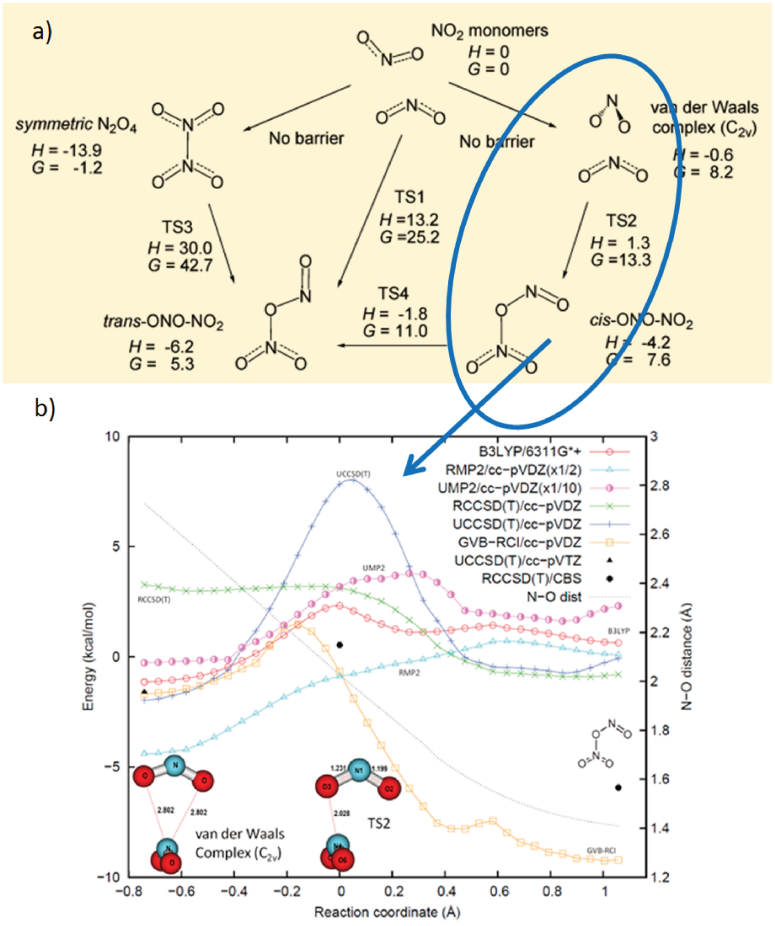

FIGURE 4.5: a) Reaction paths and thermochemical data for interconversion between isomers of NO_2 dimer. (RCCSD(T)/CBS//B3LYP/6-311G*+ enthalpy and free energy in kcal/mol). b) The PES for asymmetric dimerization $2NO_2 \rightarrow cis-ONO-NO_2$. The cis-dimer is considered in this work. Figure adapted from [125].

We have chosen to perform QM/MM AIMD calculations of the cis NO_2 dimer dissociation. Cis dimer was chosen mainly because of possible comparison with previous results available in literature. In the study of group of R. Benny Gerber [133] they have showed that BLYP functional paired with dispersion corrections gives good results for the cis dimer. In the future, we plan to investigate the trans-dimer also. Because of the high computational cost, the electronic structure calculations can only be performed using DFT methods. Gas phase geometrical and energetic properties of the system are benchmarked for the DFT calculations using both B3LYP and BLYP functionals in comparison with published results [125]. The electronic structure is calculated with the Quickstep module which combines the hybrid Gaussian plane wave method for ab initio Born-Oppenheimer molecular dynamics within the Kohn-Sham framework of DFT [91, 92]. The Becke-Lee-Yang Parr [135, 136] functional incorporating the Grimme dispersion correction [137, 138], BLYP-D3, is used. The Kohn-Sham orbitals are expanded in a triple valence basis with two sets of polarization functions (TZV2P) and

core electrons replaced by norm conserving atomic pseudopotentials optimized for BLYP [139]. Elements of the Kohn-Sham and overlap matrices less than 10^{-12} are neglected, a 400 Ry electron density grid is employed, and a convergence criterion of 10^{-9} is placed upon the electronic gradient. The nuclear equations of motion are integrated with a 1 fs time step. Comparison of B3LYP/DZVP and B3LYP/TZVP calculations with core electrons replaced by norm conserving atomic pseudopotentials [139] and all electrons calculations with B3LYP/6-311++G* are performed and values are compared. The latter basis set is close to the one employed in the literature [125]. All hydrogen are replaced by deuterated one to enable utilization of a larger propagation step size.

The geometries obtained with the various methods are detailed in Table 4.1 and they vary slightly with the methods. For the binding energy, defined as the difference between the dimer energy and the energy of the two separated molecules, differences are more significant. The values of the binding energy for the symmetric dimer vary between -11.78 and -15.58 kcal/mol compared to the reference value of -16.5 kcal/mol. For the cis-dimer, the energies range between 0.60 and -2.50 kcal/mol compared to the RCSSD(T) value of -5.9 kcal/mol. The BLYP-D3/TZV2P method gives the best agreement with the RCCSD(T) data, providing confidence in choosing this functional and basis set.

The ability of the BLYP-D3/TZV2P is also tested for the NaCl crystal. 3 layers are considered, each one counting 36 atoms and the first layer being fixed. The obtained lattice constant, 5.64 Å, corresponds to the experimental value [112] as shown in Fig. 4.6. Similarly, the use of this functional is also validated for the water molecule 4.7.

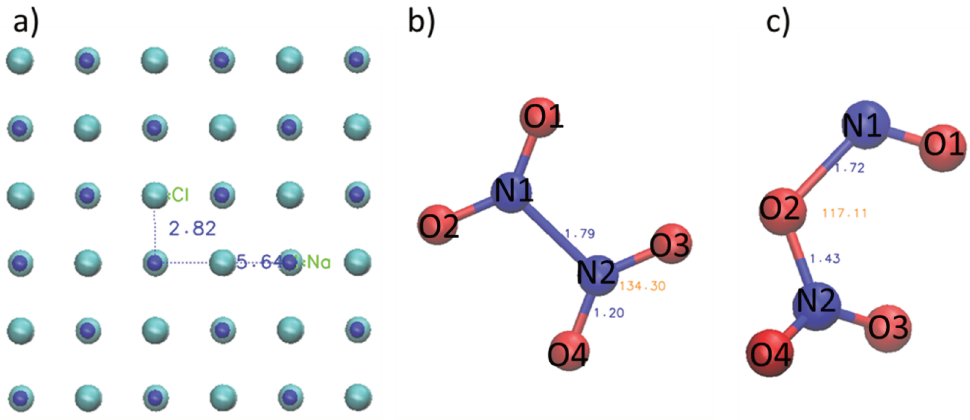

FIGURE 4.6: Geometrical values used for benchmarking CP2K and DFT functionals. Reported values on figure correspond to B3LYP/DZVP combination. a) Nacl crystal, consisting of 3 layers. Each layer counting 36 atoms while first layer having fixed position. Obtained lattice constant corresponds to experimental value [112]. b)NO_2 symetric dimer and c)NO_2 cis-dimer.

TABLE 4.1: Bond lengths (in Å) and angles (in degrees) for the NO_2 dimers in gas phase. Also NaCl lattice parameter for two DFT functionals.

	BLYP-D3/TZV2P	B3LYP/DZVP	B3LYP/6-31G++	B3LYP/6-311G*+ [125]
symmetric dimer, N1-N2	1.84	1.79	1.79	1.81
cis dimer. N1-O2	1.73	1.57	1.57	1.71
cis dimer. O2-N2	1.46	1.45	1.45	1.40
cis dimer.∠ N1-O2-N2	116.17	114.63	115.75	117.79
NaCl. lattice parameter	5.64	5.64	-	-

TABLE 4.2: Binding energies (in kcal/mol) for the NO_2 symmetric and cis dimers.

	BLYP-D3/TZV2P	B3LYP/DZVP	B3LYP/6-31G++	B3LYP/6-311G*+ [125]	RCCSD(T)/CBS [125]
Symmetric dimer	−15.58	−11.78	−15.14	−13.50	−16.50
Cis dimer	−2.50	0.46	−2.09	0.60	−5.90

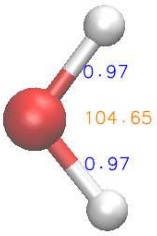

FIGURE 4.7: Optimized geometry for water with BLYP-D3/TZV2P level of theory, bond lengths are given in blue (Å) and angle (degrees) in orange. Values are in good agreement with the literature [140].

Table 4.3 gives Mulliken charges for the symmetric and cis NO_2 dimer in the gas phase. To be noted that our calculated charges for the cis dimer are not in agreement with the published values, calculated in the group of R. Benny Gerber [133]. Functional, basis set and the software used in our study and in the published paper [133] are the same. It is difficult to give a clear explanation for these different results. We can suspect that they have given the charges of the cis dimer on the water slab instead of charges in the gas phase.

TABLE 4.3: Gas phase Mulliken charges at BLYP-D3/TZV2P level of theory. Water molecule charges are in the range of values reported in literature [141]

Mulliken charges	NO_2						Water		
	N1	O1	O2	N2	O3	O4	OW	HW1	HW2
symmetric dimer	0.022	-0.011	-0.011	0.022	-0.011	-0.011	-0.450	0.225	0.225
Cis dimer	0.053	0.190	-0.185	0.071	-0.090	-0.040			

Due to the high computational cost, the QM part is actually reduced. More precisely, only one surface layer of NaCl crystal is treated quantum mechanically, while the underneath layers are treated classically. In order to

validate this reduced description of the system, a simulation with 2 quantum surface layers is also performed for comparison. Fig. 4.8 and 4.9 show behaviour of dissociation bond and Mulliken charges. The behaviour of the system is qualitatively the same. After fast dissociation, ions are stable for 1 ps and 2 ps for the simulation with 1 QM and 2 QM layers respectively. After this, they both effectively recombine to 2 isolated monomers. Also charge transfer is not affected with number of QM atoms. Thereby simulations are carried out with 1 layer of QM atoms.

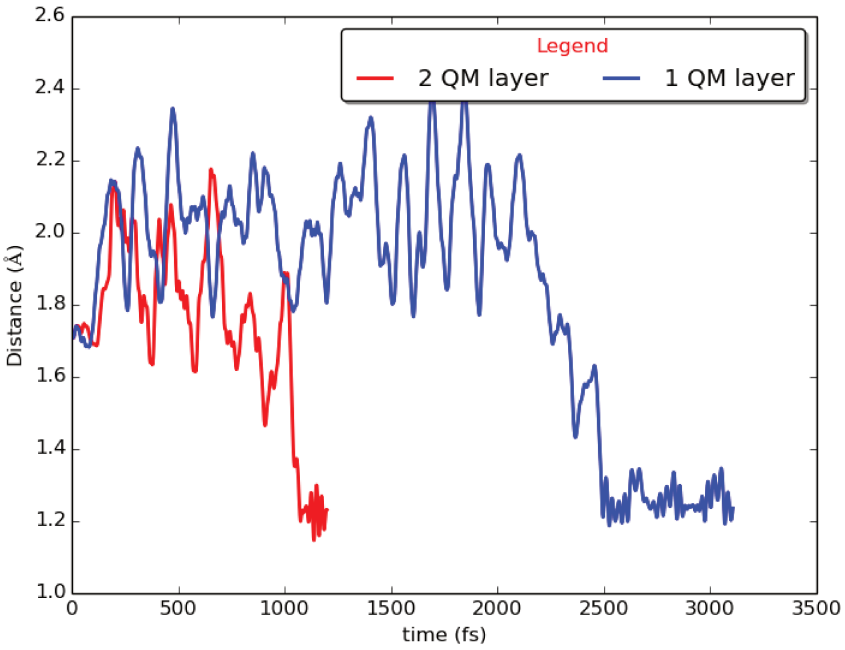

FIGURE 4.8: Time evolution of $N1 - O2$ bond length for 1 or 2 NaCl layers treated quantum mechanically (Fig. 4.6 c)).

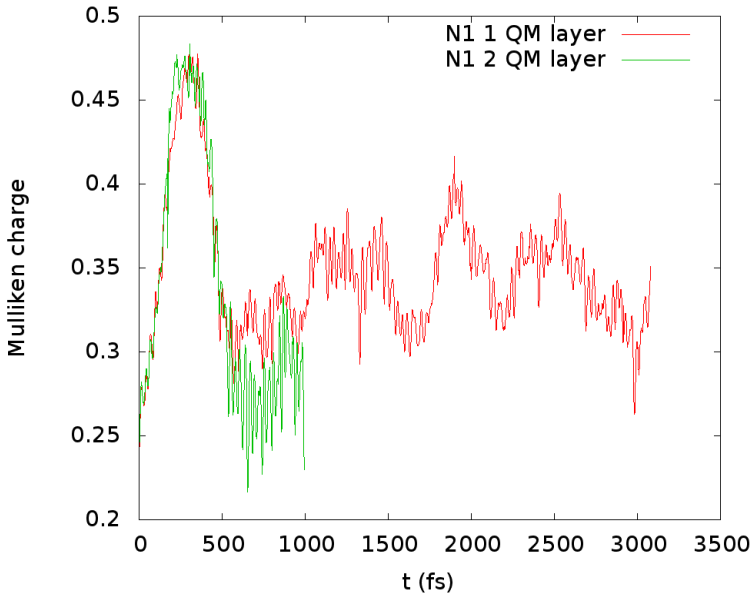

FIGURE 4.9: Mulliken charge of N_1 atom (Fig. 4.6 c)) for 1 or 2 NaCl layers treated quantum mechanically

4.4 AIMD simulation in the QM/MM frame

This part is the continuation of the work presented in Chapter 3. PA island formation was evidenced, humidity driving this heterogeneous coating of PA on the NaCl substrate. From the experiments conducted in the group of S. Sobanska [19], it is visible that FAs are not directly involved in the reactivity process of NO_2 with NaCl and formation of $NaNO_3$, but indirectly through their distribution relatively to water. As shown in Fig. 4.10, $NaNO_3$ formation occurs on areas where water is present. Indeed, the catalytic role played by water in the NO_2 reactivity is well known [130]. Water promotes NO_2 dissociation and stabilizes the ions. As a consequence of the heterogeneous coating, areas with different quantity of water will exist and since water drives the reactivity, it is crucial to study this effect. This is why cis-dimer dissociation is studied here under different humidity conditions. PA molecules are omitted since they do not participate directly in reactivity, and inclusion of these large molecules makes the calculation difficult to handle. Due to the increase of the system size, the QM/MM implementation gets even more complicated. Three different cases are considered, each one corresponding to possible configurations on the NaCl surface: 1) dry conditions, 2) a partially formed water monolayer on NaCl which corresponds to RH <30% and 3) a full water monolayer, RH >30%. The number of QM atoms is variable depending on the simulation and in all the cases the first layer of MM atoms is fixed. The infinite sandwich model is used [142], i.e. the system is periodic in 2 dimensions both for MM and QM parts.

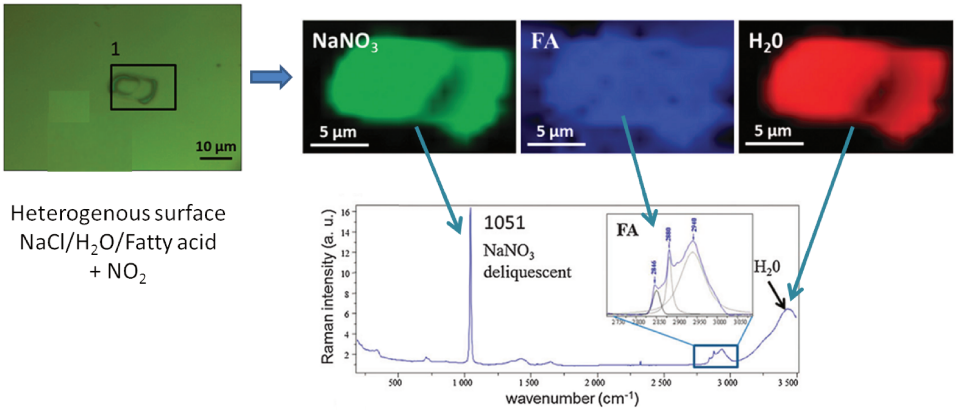

FIGURE 4.10: Raman images reconstructed for deliquescent $NaNO_3$ (green 1051 cm^1), stearic acid (blue 2700–3000 cm^1) and H_2O (red 3400 cm^1), respectively. Spatial correlation of involved species is evident [19].

Table 4.4 summarizes the calculation details of each simulation.

TABLE 4.4: Details of the QM/MM calculations.

	Number of QM atoms	Number of MM atoms	Trajectory duration (fs)	Calculation time (days)
(1) dry conditions (1/2 QM layer)	126/246	576/456	3000/1150	~7/14
(2) RH <30%	250	576	2450	~14
(3) RH >30%	147	360	1110	~7

4.4.1 Under dry conditions

Initially, the NaCl substrate is equilibrated at 300 K for 500 fs. The cis NO_2 dimer is then positioned 5 Å from the surface and directed toward the substrate with a velocity corresponding to a temperature of 300 K. Fig. 4.11 shows the dissociation and recombination of the dimer on the perfect NaCl (100) surface. Fast dissociation into NO_3^- and NO^+ ions occurs upon contact with the surface within 10's of fs. Fig. 4.12, representing the time evolution of the bond lengths or atoms separation, shows that dimer dissociation occurs within the first 50 fs as the $N_1 - O_2$ bond increases over 2 Å. The formed ions are stable on the surface for 2 ps and then recombine to form two isolated monomers.

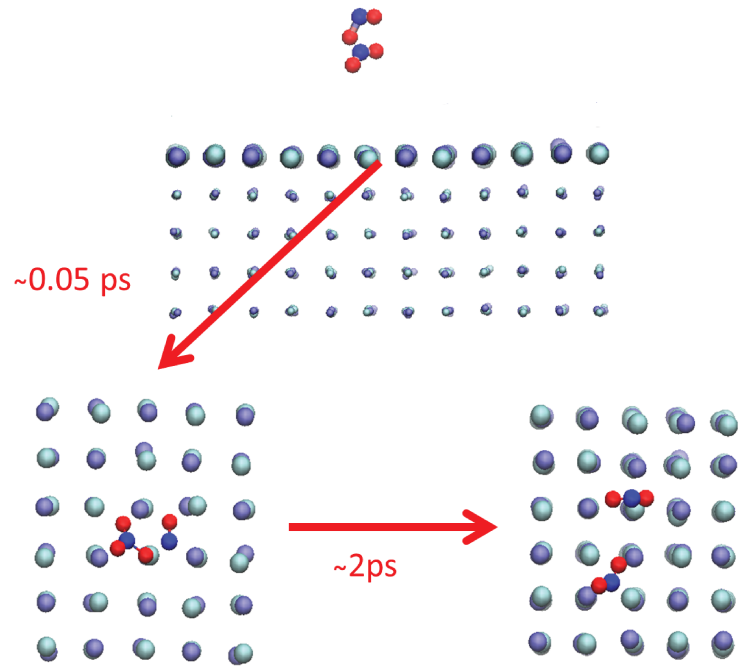

FIGURE 4.11: Figure illustrating the $cis - NO_2$ dimer dissociation and recombination to isolated monomers. QM atoms are represented by balls and MM atoms by points.

NaCl(100) surface is characterized by Na-Cl ion pairs (Fig. 3.3). The ions formed from the dimer dissociation remain close to each other, strongly bonded to the surface ions through coulombic interactions. NO_3^- ion is bonded to Na^+ and NO^+ ion to Cl^-. This is shown by the green line which corresponds to NO_3^--NO^+ distance on Fig. 4.12. The distance separating the ions is close to the value of the Na-Cl separation (2.8 Å) in the surface. This "trapping" prevents ions to move away from each other and also from the surface. The stabilization of the ions may favor the reaction with the surface and consequently the formation of $NaNO_3$.

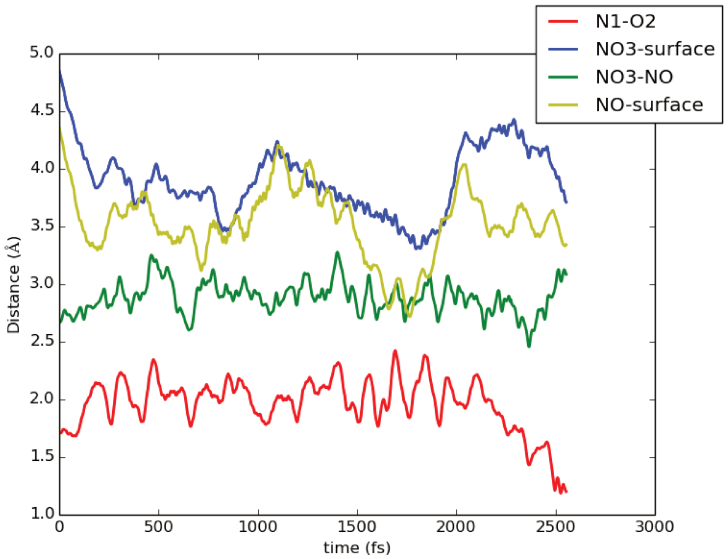

FIGURE 4.12: Time evolution of atoms separation in Å for dry conditions. Blue and yellow lines represent the distance of NO_3^- and NO^+ ions from the NaCl surface, respectively. Red line corresponds to the $N_1 - O_2$ dissociation bond length and green line defines the distance between the NO_3^- and NO^+ ions.

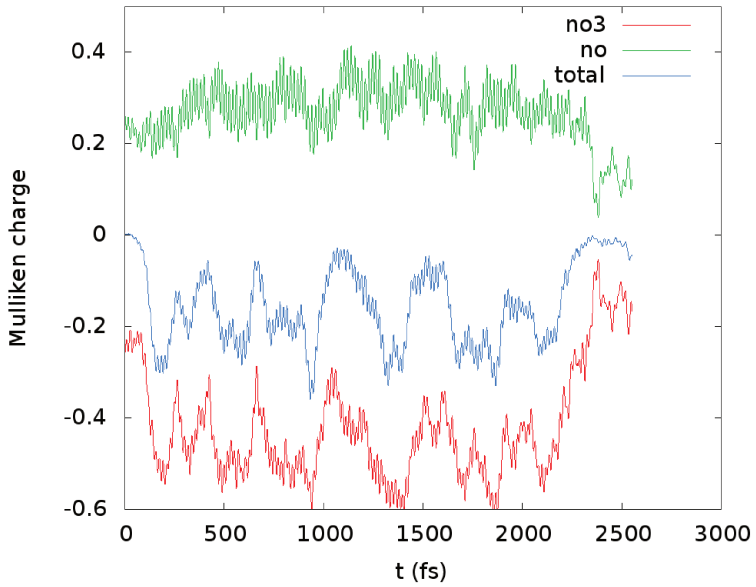

FIGURE 4.13: Mulliken charges (au) of the invoked group of atoms for dry conditions. Total corresponds to the total charge of the 2 NO_2 dimer (in a.u.).

Fig. 4.13 represents the Mulliken charges of NO_3^-, NO^+ and of NO_2. Mulliken charges support the results obtained by distance analysis and dissociation shown on Fig. 4.12. Reported charges on the surface can be compared with gas phase Mulliken charges given in Table 4.3. In the case of

surface, the electronic cloud is more localized on the nuclei. Upon dissociation, the absolute values of the charges are increasing for almost all atoms. Charge transfer between the surface (more precisely Cl) and NO^+ ion is visible since total charge is oscillating towards negative values and the same tendency is visible for NO_3^- ion.

4.4.2 RH < 30%

The second step is addition of water to the system. As already explained, water should act as a catalyst and promote dissociation. The amount of water added here corresponds to RH smaller than 30%, since a full water monolayer is formed on a NaCl surface around 30% RH. This models a possible configuration that could exist on the heterogeneous PA-coated NaCl surface. NO_2 dimer, water and the first layer of NaCl are in the QM box, making a total of 250 QM atoms. Water on the substrate is equilibrated for 1 ps at 300 K prior exposure to NO_2 dimer, directed toward the surface with a kT kinetic energy.

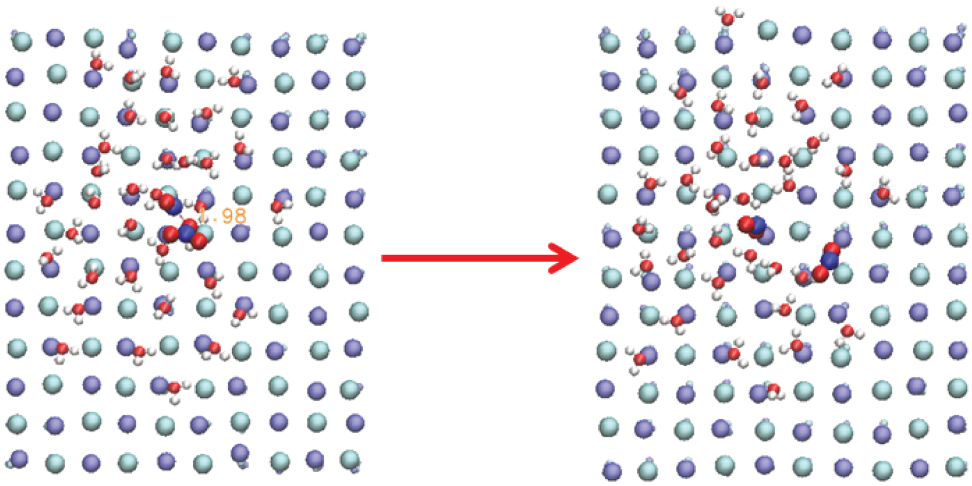

FIGURE 4.14: Figure illustrating the fast dissociation and recombination to the two isolated monomers of the $cis-NO_2$ dimer. NO_2 nitrogen in dark blue color, oxygen in red, chlorine and sodium atoms in glassy green and blue representation respectively.

Cis-dimer exhibits fast dissociation within 10's of fs in a similar way as on the bare surface. NO_3^- and NO^+ ions are formed as can be seen from the time evolution of the Mulliken charges (Fig. 4.16). This is also evidenced from the lengthening of the $N_1 - O_2$ dissociation bond (Fig. 4.15). The ions remain stable during 1.5 ps before recombining into two isolated NO_2 monomers. Looking in more details on the snapshot of Fig. 4.14, it seems that recombination occurs when one of the NO_2 molecules leaves the water substrate and then becomes exposed directly to the NaCl surface. Since the water coverage is low, ions can not form clusters with water molecules,

water molecules are rather dispersed over the salt and the ions are in direct contact with NaCl surface, recombining to two isolated monomers (Fig. 4.15).

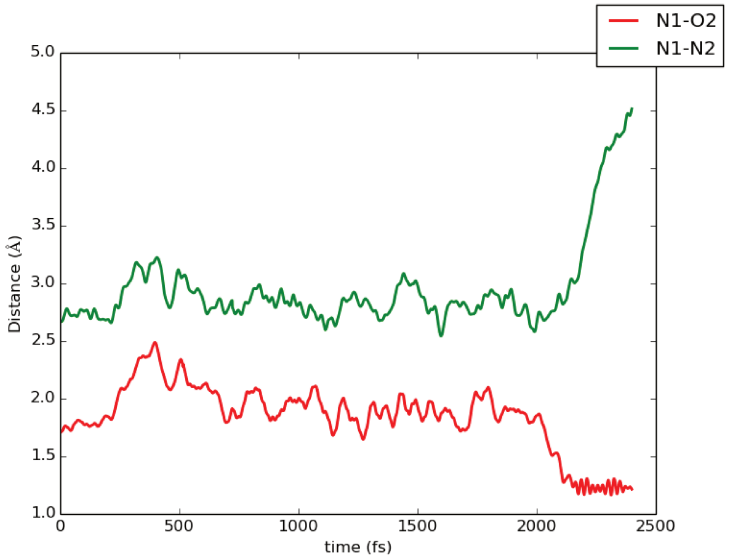

FIGURE 4.15: Time evolution of atoms separation in Å for RH < 30%. In green distance of $N1$ and $N2$. Red curve stands for the $N_1 - O_2$ dissociation bond.

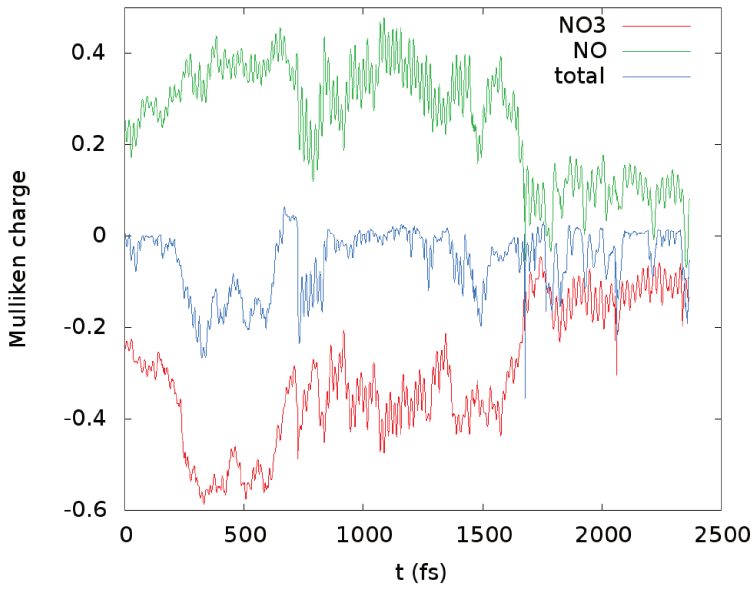

FIGURE 4.16: Mulliken partial atomic charges (au) of the invoked group of atoms for RH < 30%. Total corresponds to the total charge of the $2NO_2$ dimer (in a.u.).

4.4.3 RH > 30%

For this last case, the water concentration becomes more important. In the condition of RH > 30%, water creates a full monolayer on the NaCl surface. Water and NO_2 molecules are treated quantum mechanically; which gives 147 QM atoms. Water is equilibrated on the NaCl surface before introducing NO_2 dimer, which was sent to surface having kT kinetic energy directed toward the surface. As in previous cases, the cis-dimer dissociation occurs shortly, within 10's of fs, after the arrival of the dimer on the wet surface. While in the first two cases, 0 and <30% RH, ions stay sufficiently close to each other (within a distance between 2 and 3 Å) to recombine after some time into two isolated nearly neutral monomers, here the distance quickly increases to more than 4 Å. Ions are separated by water molecules.

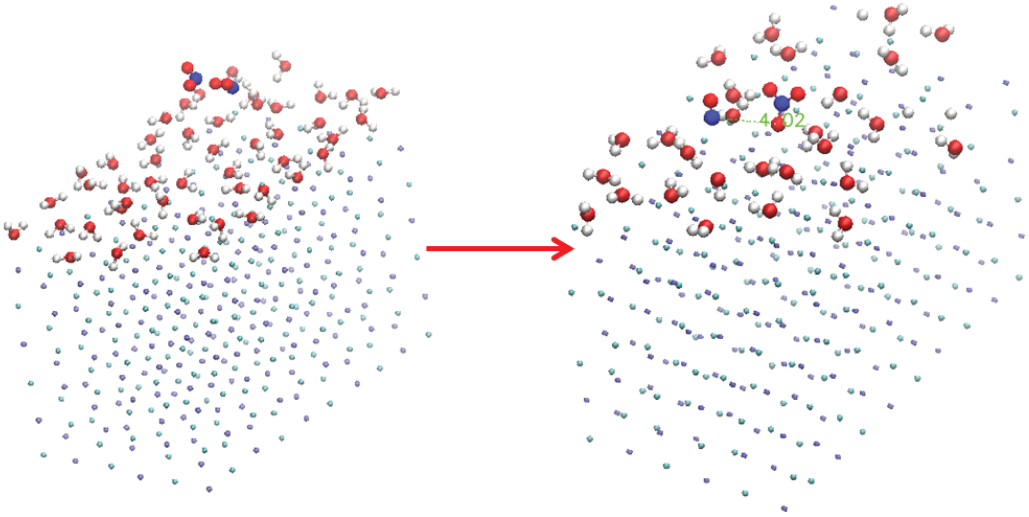

FIGURE 4.17: Figure illustrating the fast dissociation of the $cis-NO_2$ dimer and ions formation for RH > 30% . The ions are sufficiently far from each other for not recombining. QM atoms are in the balls representation and MM in points.

From Fig. 4.18, it is visible that after cis-dimer accommodation on the wet surface, fast dissociation occurs leading to ions isolation. The Mulliken charges analysis indicates an important charge separation between the ions probably due to charge transfer between water and ions.

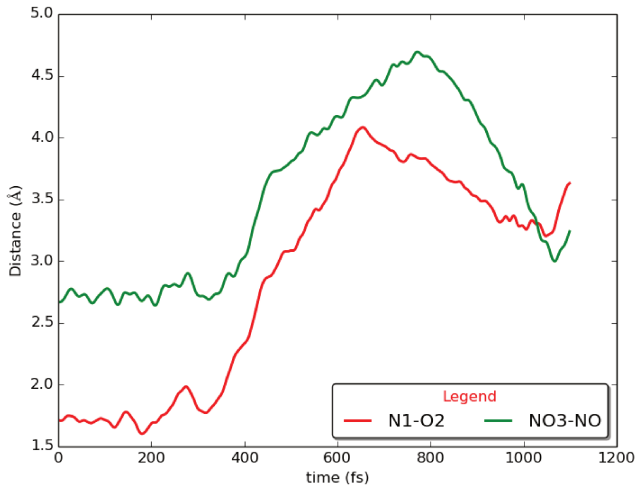

FIGURE 4.18: Time evolution of atoms separation in Å for RH > 30%: In green $N1 - N2$ distance, in red $N_1 - O_2$ dissociation bond.

Fig. 4.19 are snapshots of fragments extracted from simulation. Water cluster formed with NO_3^- and NO^+ ions are visible. Negative NO_3^- ion tends to create three bridges with water hydrogen through three own negatively charges oxygen. On the other hand, NO^+ ion creates bridges with water oxygen. NO_3^- ion cluster is more stable what is visible from equilibrium cluster distances.

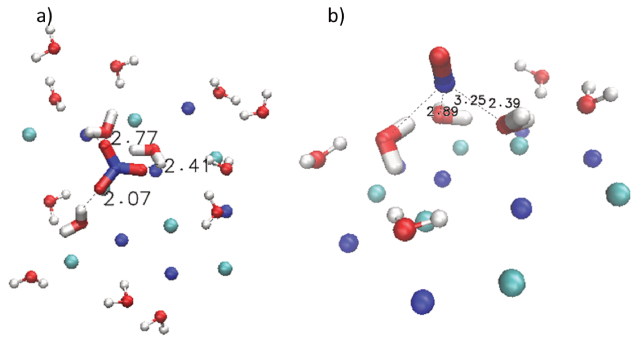

FIGURE 4.19: Snapshots of a configuration extracted from the dynamics with emphasis on the a) NO_3^--water cluster or the b) NO^+-water cluster.

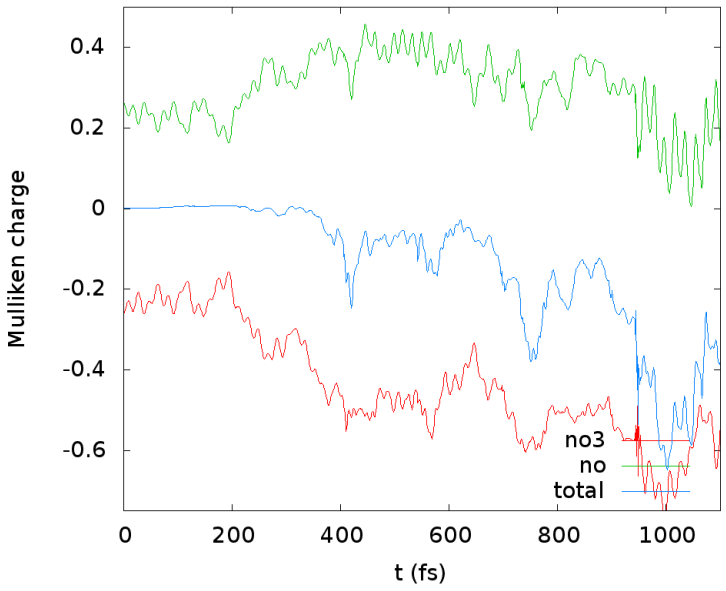

FIGURE 4.20: Mulliken charges (au) of the NO^+ and NO_3^- ions for RH > 30%. Total corresponds to the total charge of the dimer.

Moreover transfer is dominated with NO_3^- ion since NO_3^- charge changes in coherent way with total charge (Fig. 4.20). As shown in Fig. 4.19, three hydrogen atoms of water are pointing toward the NO_3^- oxygens, stabilizing the ion on the water film. It is more difficult for NO^+ to find binding sites. It would preferentially bind to negative water oxygen. Water binds to NaCl surface through Na^+-$O^-H^+H^+$ bridges leading to an orientation of the water molecules with their hydrogen atoms directed upwards [121]. Taking into account all this, we can say that this is an unfavourable configuration for NO^+ to effectively bind to water substrate. The trajectory should be continued to see how the ions will evolve in the system.

4.5 Conclusion

In this chapter, the results obtained by QM/MM AIMD simulations are presented. Special attention is paid to the influence of water on NO_2 reactivity on NaCl aerosols. Under dry conditions, the cis-dimer exhibits fast dissociation and then recombination to two isolated NO_2 monomers. In the condition of water partially covering NaCl, fast dissociation is also observed but the quantity of water is not sufficient to stabilize the ions. Fig. 4.21 represents the calculated charge separation between NO^+ and NO_3^- ions for reactant (cis-dimer) and product (ions). Increase in charge separation provides evidence for NO_2 dimer dissociation. In the case of full water monolayer (RH >30%), the average charge separation is the most important. This is also an indication of the most effective dissociation under high humidity conditions. In the group of prof. Gerber, NO_2 dissociation has already been studied. Miller et al. [134], using AIMD on MP2 level of theory, showed that on 3 water molecules clusters, immediate dissociation of the $2NO_2$ dimer occurs. At the BLYP-D3 level of theory, fast dissociation

was also observed [133]. What is new in our study is the influence of the NaCl surface. Under high humidity conditions (RH > 30%), the nitrate ion, produced from the fast dissociation of the cis-dimer, is stabilized. Nitrate is bonded to hydrogen atoms of neighboring water molecules. Our results support the experimental results obtained in the group of S. Sobanska. They observed that $NaNO_3$ existence is correlated with FA locations, and consequently also with water locations. Indeed, in the previous chapter, we have shown that water tends to create water clusters close to FAs. In addition, for a non-coated surface [143], creation of $NaNO_3$ is also observed when humidity increases.

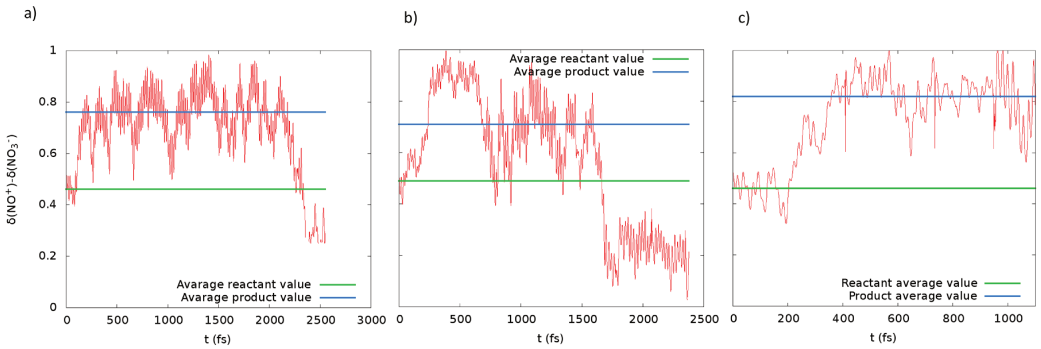

FIGURE 4.21: Charge separation of NO^+ and NO_3^- ions (NO^+-NO_3^- charge). Horizontal green and blue lines correspond to average charge separation of NO^+ and NO_3^- for the cis-dimer before dissociation and after dissociation to ions, respectively. a) dry surface; b) RH < 30%; RH > 30%

Chapter 5

Modelisation of n-butanol aerosol: aggregation by water uptake near the melting temperature

The work presented in this chapter is done in collaboration with Prof. Jan Pettersson (GAC, Gothenburg). The idea is to shed light on the experimental results by molecular level modeling. Note that a part of the work has been done by a Master 2 student, Yassine Bouchafra, under the supervision of Celine Toubin and myself. I tutored the Master student during his internship.

5.1 Introduction

As already mentioned in Chapter 1, thanks to field measurements and laboratory experiments, organic aerosols presence and impact on climate are becoming more and more evident [7, 144]. When organic substances are released in the atmosphere, they may form aerosols and interact with the water present all around [145]. Precipitation and radiation levels are affected by the efficiency of the water condensation mechanism. Liquid or solid particles of typically 0.2 μm diameter are involved. They serve as a starting point for water vapour condensation and formation of clouds. In the atmosphere, water is ubiquitous and influences various processes [146, 147]. Fig. 5.1 illustrates water accommodation on organic aerosols. Once the aerosols are in atmosphere, they serve as a CCN. Wetting process starts and water creates films or droplets at the aerosol surface. These particles can be then transformed in cloud droplets under high humidity conditions. Interaction of water with hydrophobic surfaces is not fully understood, especially the details of water dynamics in the presence of organic molecules [145, 148]. Low volatile organic compounds are known to condense on existing particles and form coated aerosols, thereby changing their physical and chemical properties [149, 150]. The organic fraction in atmosphere is assumed to be liquid, but nowadays, it is admitted that it can also coexist as solid or glassy. The phase state is thought to have a significant impact on particles growth [151]. Due to the complexity of the problem, a multidisciplinary approach is needed to improve our understanding of water accommodation on organic aerosols. Efficiency of this process and implication of temperature on phase state is studied in the case of butanol.

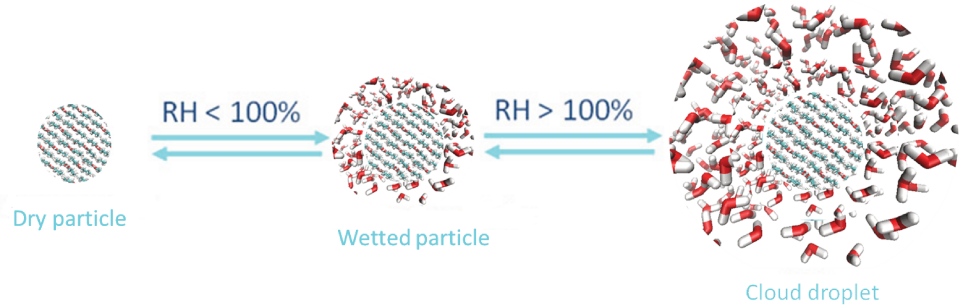

FIGURE 5.1: Illustration of water aggregation on organic aerosol.

Among organics, alcohols have interesting molecular properties, with a part of the molecule is hydrophilic (functional group) and the other part hydrophobic (carbon chain). Interesting behaviours were observed either experimentally [19, 34, 152] or theoretically [43, 103] on similar molecules. Water uptake is found to vary across the temperature range and be strongly affected when a phase transition occurs. A deeper understanding of this process is missing. MD simulations are valuable tools thanks to their ability to reach large sizes and long time scales. Previous simulations of organic systems show that the diffusion of water molecules through a water-oil interface exhibits significant role [153]. Moreover, the water penetration through membranes seems to be important on time scales of 100 ns [154]. A MD study of octanol showed that molecules near surface prefer to orient into bilayers at 298 K, and tend to create several monolayers inside the bulk [155]. Butanol is used here as a model molecule in a combined theoretical and experimental study, in collaboration with Prof. Jan Pettersson.

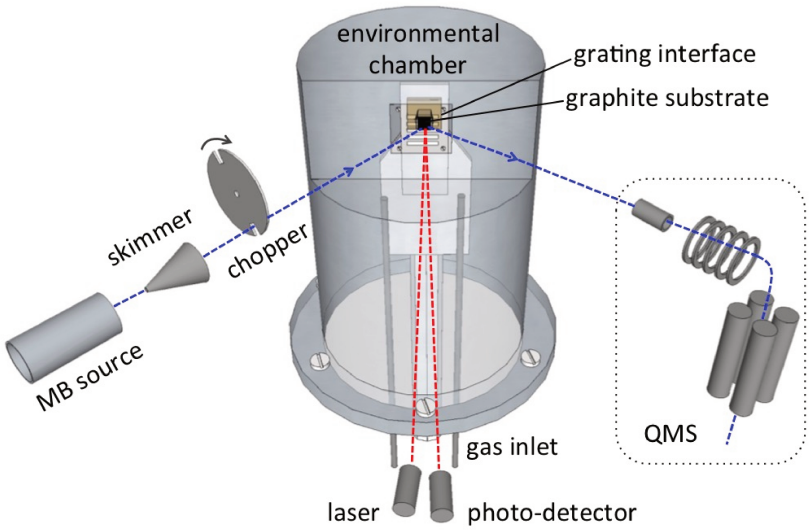

FIGURE 5.2: Schematic view of the Environmental Experimental Beam (EMB) setup [152, 156].

Fig. 5.2 describes the Environmental Molecular Beam (EMB) experimental setup developed in the group of Prof. Pettersson. The objective of this study is to monitor the water uptake and interaction with a sample inside the environmental chamber. An inlet jet of water is sent to the butanol surface and the outlet jet is monitored and analyzed by mass spectroscopy. Fig. 5.3 shows the signal due to the scattered water molecules. Thanks to recent technological developments, the outlet jet can be analysed for different angles, while previous set up only probed the specular direction [152]. The advanced technique allows also to decompose the output signal into three channels: one corresponding to the inelastic scattering, i.e. molecules that are not thermally equilibrated with surface, and two others signals corresponding to fast and slow thermal desorption, i.e. molecules desorbing after being trapped on the surface for a certain time. Informations about collision dynamics, surface and bulk accommodation, desorption and diffusion kinetics can be extracted from these experiments.

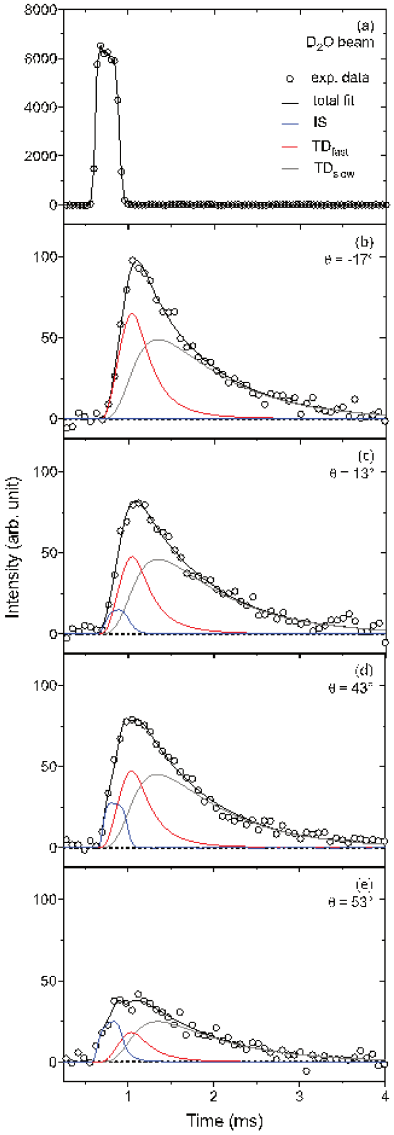

FIGURE 5.3: Time-of-flight distributions of water intensities of the inlet jet (a). Remaining panels show the scattered water molecule leaving the solid n-butanol surface in different scattering angles (θ) with respect to the surface normal. The angle between the inlet jet and the surface normal is equal to 43° having an incident kinetic energy of 0.28 eV. Figure obtained from Sofia Johansson.

Gas molecules colliding with a surface in general are highly inelastic, which results in an efficient vapour condensation on the surface [145, 157]. Therefore the surface accommodation of water tends to be absolute under typical ambient conditions. Organic molecules such as alcohols can create hydrophobic surfaces that significantly decrease water uptake. Another aspect is the temperature dependence. For higher temperatures and liquid state of the surface, water uptake is very efficient. This is evidenced in the case of n-butanol (BuOH), the water accommodation changes brutally over a 10 K interval around the BuOH melting point (185 K) (Fig. 5.4). Fig.

5.5 shows available time scales accessible with EMB and MD methods. Informations obtained with simulation are complementary to experimental results providing physical insight on the processes.

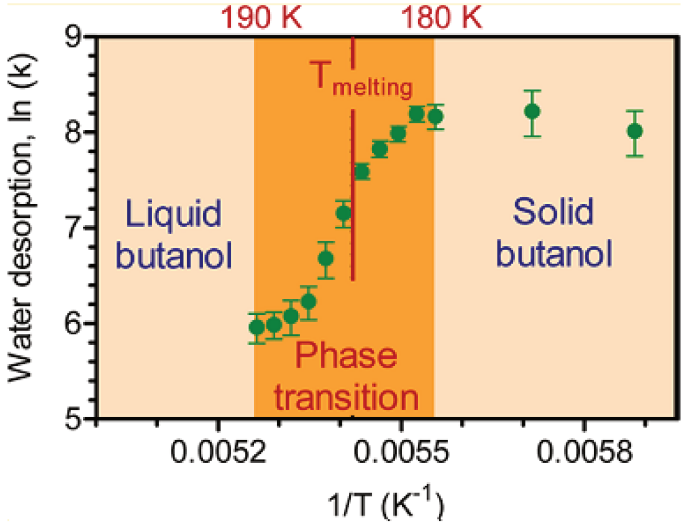

FIGURE 5.4: EMB derived desorption rate constants k of D_2O on n-butanol as a function of temperature. Melting occurs at 185 K. Figure taken from [152].

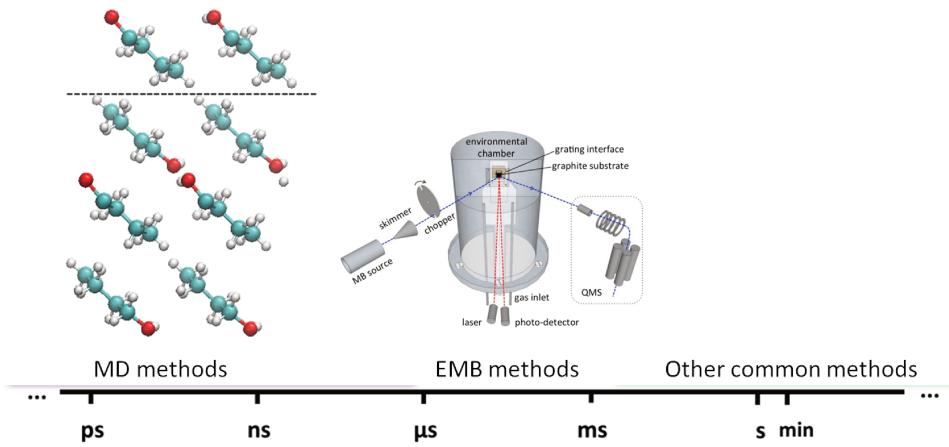

FIGURE 5.5: Available time scales of the MD simulations and experimental studies.

5.1.1 Computational details

The GROMACS package [69], has been employed to perform classical molecular dynamic simulations. The equations of motion are integrated using the leap-frog algorithm [76]. A cut off distance fof 1.4 nm is applied for the short range interactions. Long range electrostatic interactions are treated using the Particle Mesh Ewald (PME) method (see Chapter 2). All bonds are constrained with the LINCS [111] algorithm making possible the use of a 2 fs time step. An infinite crystal is created by duplicating an unit cell in

x, y, z directions. After a minimization with the steepest descent algorithm, the crystal is equilibrated in the NPT ensemble at T=150 K during 10 ns giving a crystal structure close to the experimental one.

5.2 Creation of a butanol slab and melting point determination

The butanol crystal is created on the basis of the published X-ray structure [158]. The cohesion of the crystal is insured by a strong hydrogen bonds network (Fig. 5.6).

TABLE 5.1: Hydrogen-bond lengths (Å) for the n-butanol crystal from our calculations and compared with experiments [158]. The labels of the atoms are defined in Fig. 5.6

D—H...A	Experiments	Simulation
C2a—H2a...Ob	2.86	2.80
Oa—HOa...Ob	2.03	1.90
Ob—HOb...Oa	2.00	1.90

Once prepared, the crystal is cut along a given direction generating two interfaces. The direction used to create the surface, noted with green dashed line on Fig. 5.6, is chosen because it gives the lowest energy. The simulation box is extended to 2 nm along the z direction for each side. The slab of dimensions 4.7 x 5.0 x 8.7 nm is heated at various temperatures and equilibrated in the NVT ensemble for 50 ns.

Butanol was at first modeled by the 'original' OPLS-AA (All Atom) force field [74], that gives reasonable results for various properties of organic liquids [75]. However, while increasing the temperature even far above the melting point (240K), the structure of the crystal is preserved and no melting was observed as shown on Fig. 5.7.

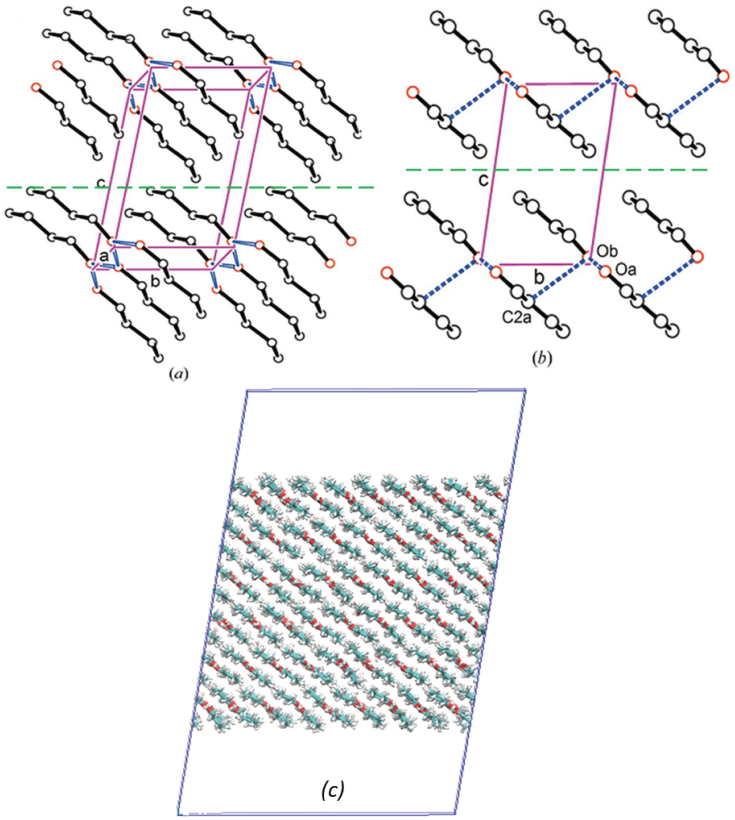

FIGURE 5.6: a) Butanol unit cell and b) the unit cell projection on a-b units vectors plane. c) butanol slab created from the given unit cell. Green dashed line correspond to surface from which slab is created. Hydrogen bonds are represented in blue color. Figure adapted from [158].

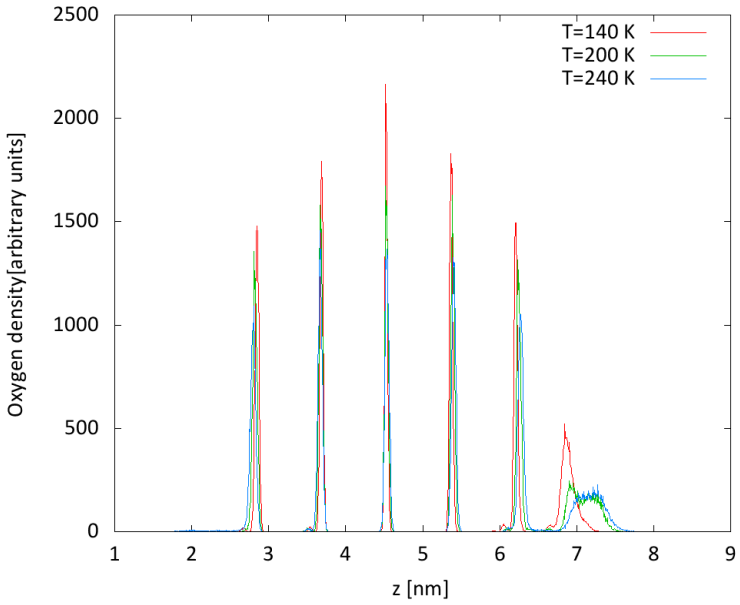

FIGURE 5.7: Calculated butanol (oxygen) densities for three different temperatures using the standard OPLS-AA force field.

The standard OPLS-AA force field fails to reproduce the melting of the butanol crystal, thereby we have applied an improved force field devlopped for carbohydrates [159]. This force field differs from the OPLS-AA force field in a new parametrization of the torsion interaction on the basis of ab initio calculations. Surprisingly, this improved force field gives very good results for the melting properties of butanol crystal as shown on Fig. 5.8. Melting is observed in the simulation around 190-200 K, i.e. 15 K above the experimental value. For all the simulations presented thereafter, the improved force field is used. The improved torsional parameters adjusted to the GROMACS format can be found in Appendix C.

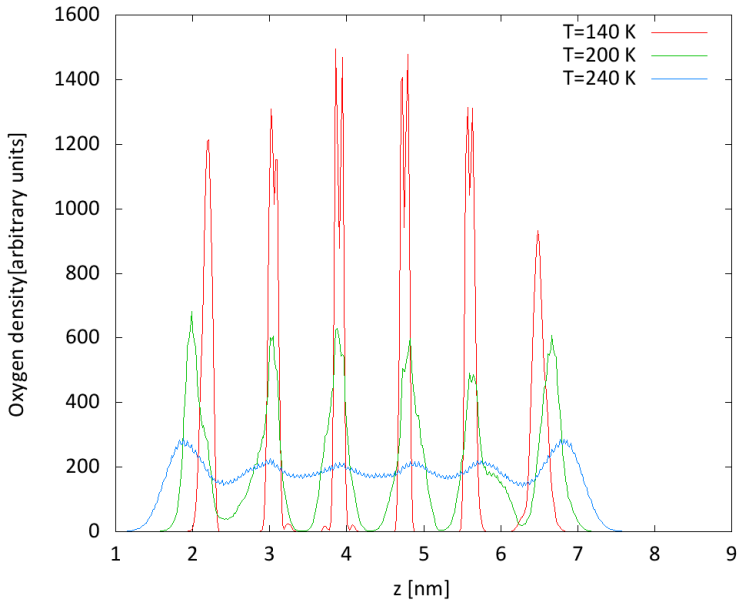

FIGURE 5.8: Calculated Butanol (oxygen) densities for three different temperatures using the improved OPLS-AA force field.

Equilibrium configurations are shown on Fig. 5.9 at three different temperatures. At T = 170 K, molecules are organized in a well ordered crystalline structure. Upon heating to T = 200 K, disorganization of molecules is occurring and a structural order remains locally. By putting the slab in the conditions of T = 240 K, a complete disorder of the molecules is achieved and the slab has melted. On Fig. 5.8 and 5.9 an homogeneous structure, similar to a liquid, for high temperature is visible. The densities of the butanol oxygen confirm the trend observed on the snapshots. The layering is still present at 200 K and disappears completely at 240 K. It is rather difficult to exactly identify the melting point since long equilibration periods are required at these temperatures. However, additional calculations are in progress to determine more precisely the butanol melting point.

5.3 Water uptake on butanol close to the melting point

We performed MD simulations to model the collision of a water molecule on an equilibrated slab of butanol. The time scale of a MD simulation is too short compared to the experiments and the uptake coefficient α will be overestimated due to the too short sampling time. Weakly bonded molecules over longer periods could desorb after the sampling period. Nevertheless valuable informations can be extracted. The presented results are a significant step for the modeling of colliding process. Different surface temperatures around the melting point are investigated for their roles in the uptake processes: (a) 170 K (solid crystal), 200 K (intermediate) and (b) 240 K (melted crystal).

Water is modeled with the TIP5P/Ew model [160], the choice of the potential being motivated by an earlier work, in which butanol layers are supported by ice layers. The gas uptake process is performed in the same

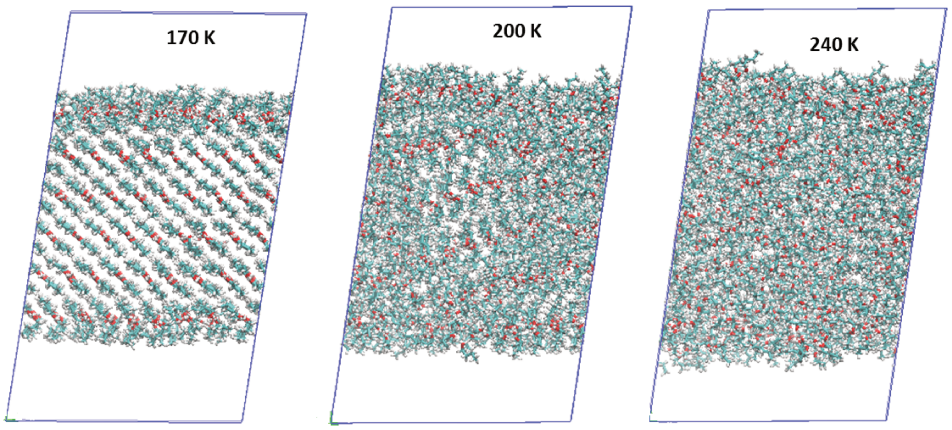

FIGURE 5.9: Butanol snapshots extracted from equilibrated simulations. Three temperatures of interest are selected: 170, 200 and 240 K

way as in the EMB experiment [152, 157]. One water molecule is sent toward the surface with an incident water kinetic energy equal to 0.29 ± 0.01 eV (1.760 ± 27 nm/ps in velocity) and with an incident angle of 45 degrees with respect to the surface normal. The initial x,y positions of the beam water are randomly chosen at a distance of 1 nm from the surface. One thousand trajectories of 100 ps are propagated for each temperature.

5.3.1 Collision with a solid surface at T=170 K

Fig. 5.10 represents the trajectories of the water molecule colliding with the surface at T=170 K. Due to the highly ordered butanol surface, water molecules are effectively trapped on the surface of the butanol slab. The structural order and the low temperature do not allow the water to diffuse inside the bulk. Moreover in the first 50 ps, 130 molecules desorb from the surface while the rest of the molecules is rapidly thermalized. Rapid thermalization of incoming water molecules on surface has already been observed in MD studies of water accommodation through a layer of butanol coating water [161].

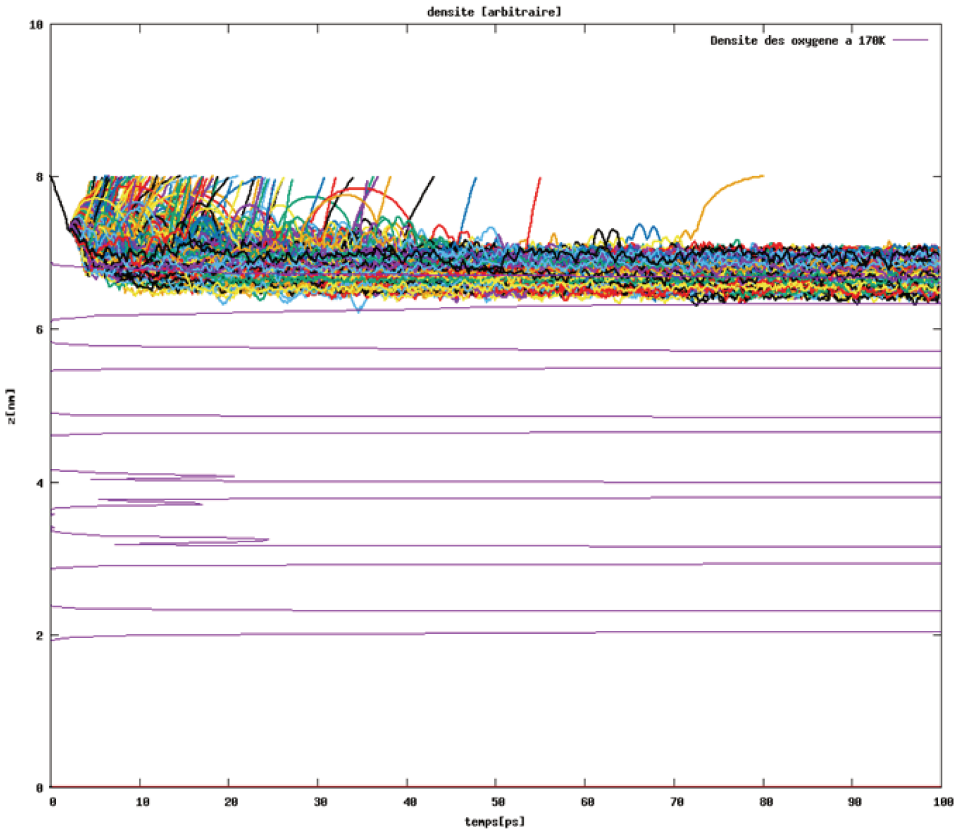

FIGURE 5.10: 940 trajectories showing the water molecule center of mass z coordinate as a function of time at T=170 K . Butanol (oxygen) density is also represented in a purple color.

The starting position (z-coordinate) and velocities are the same for all trajectories, as seen on Fig. 5.11. A statistics over 970 trajectories shows that after 25 ps more than 100 molecules are desorbed from the surface. With the convention adopted here, desorbed molecules are marked as 0 for the position distribution and -1 for velocity. After 50 ps, most of the molecules occupy adsorption sites on the surface for a z coordinate value around 6.85 nm. Adsorbed molecules are very quickly thermalized. Their squared velocity oscillates around 0.23 nm^2/ps^2, which is equivalent to T = 166 K, close to the butanol film temperature.

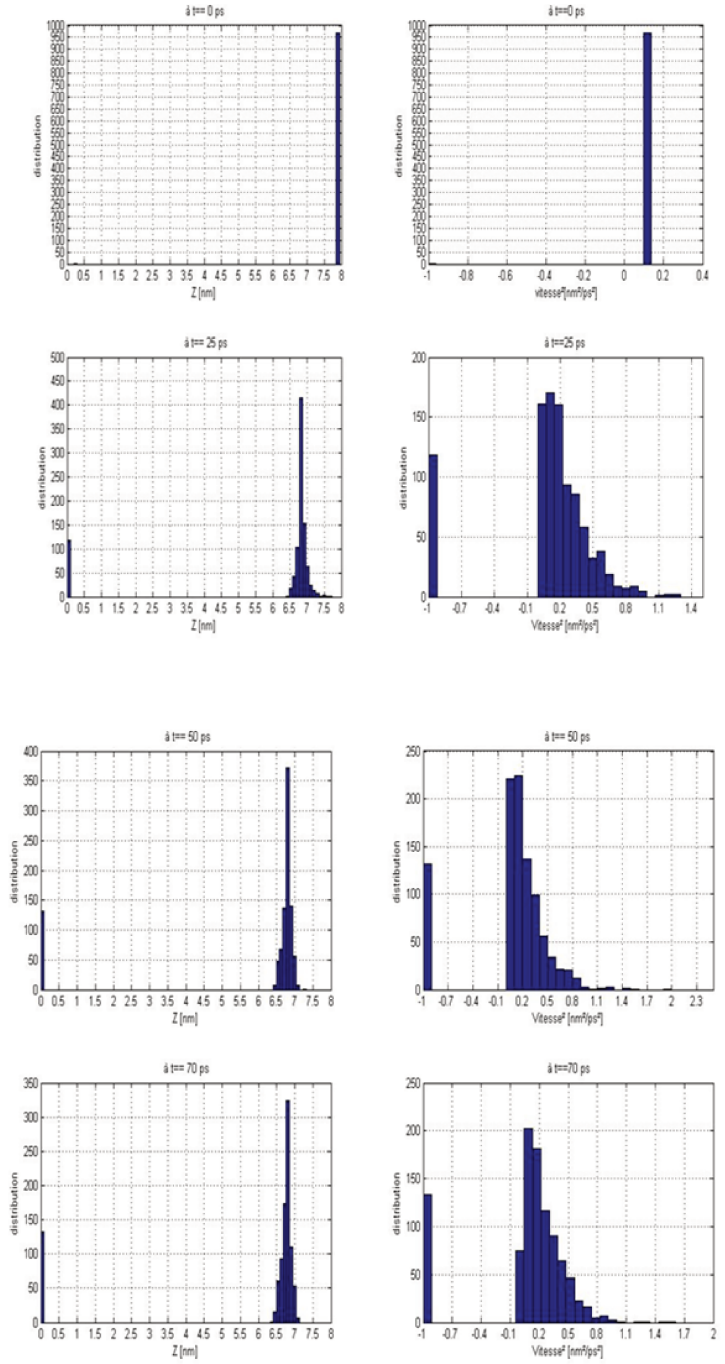

FIGURE 5.11: Distributions at T=170 K represented at different times of the trajectories from t=0 ps to t=70 ps. On the left: z-coordinate distribution of the water molecule center of mass ; on the right: kinetic energy distribution represented by the square velocity in nm^2/ps^2.

5.3.2 Collision on a premelted crystal at T=200 K

200 K represents an intermediate temperature where the butanol film is not solid any more and not liquid yet. The system is close to the melting point in a quasi-liquid state. Experimentally, such a quasi-liquid behaviour around melting point is also observed, Fig. 5.4.

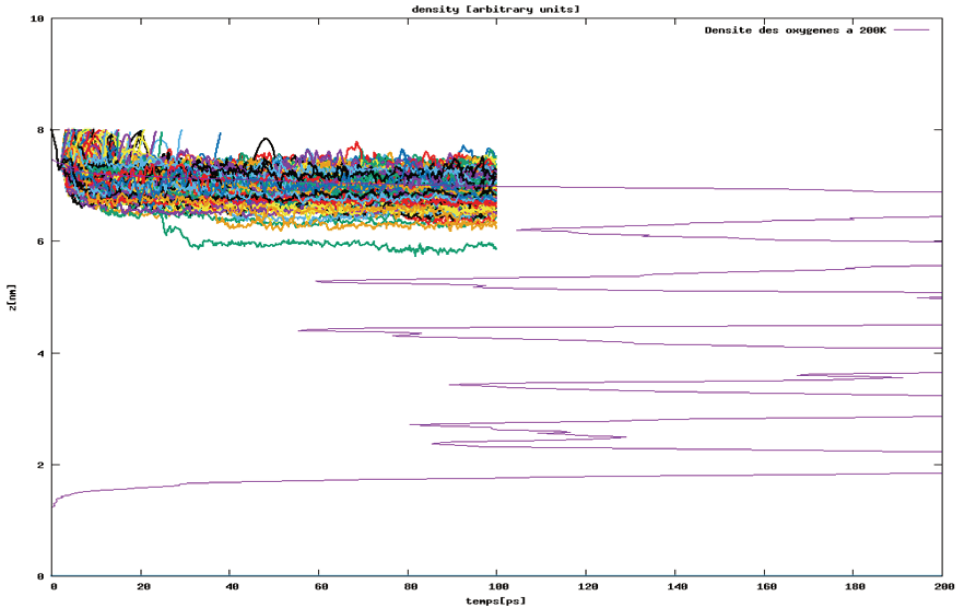

FIGURE 5.12: 970 trajectories showing the water molecule center of mass z coordinate as a function of time at T=200 K. Butanol (oxygen) density is also represented in violet color.

200 molecules over 970 (20.6 %) are quickly desorbed compared to 130 over 940 (13.8 %) at T=170 K. Desorption is fast and occurs during the first 25 ps, the local properties of the surface layer somehow influencing this behaviour. Note that diffusion inside of bulk is now possible and it happened only for few molecules. Adsorbed and absorbed molecules are thermalized with the surface within 70 ps (Fig. 5.13).

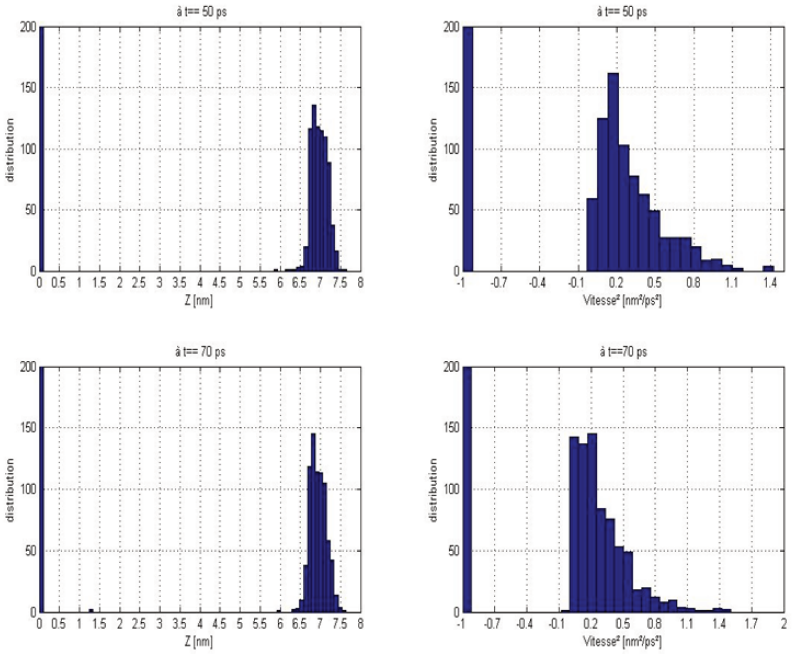

FIGURE 5.13: Distributions at T=200 K represented at different times of the trajectories from t=0 ps to t=70 ps. On the left: z-coordinate distribution of the water molecule center of mass ; on the right: kinetic energy distribution represented by the square velocity in nm^2/ps^2.

5.3.3 T=240 K

At T=240 K, the butanol slab is completely melted and molecules are randomly oriented. For the "high" temperatures, trapping of molecules is extremely efficient and desorbing events are not observed. From the other hand, the fraction of molecules which effectively diffuse inside the slab is much more significant (Fig. 5.14). Molecules are even faster thermalized with the surface (Fig. 5.15).

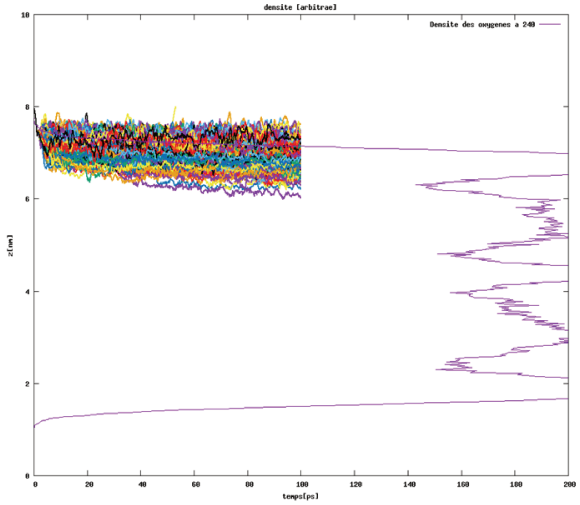

FIGURE 5.14: 970 trajectories showing the water molecule center of mass z coordinate as a function of time at T=240 K. Butanol (oxygen) density is also represented in violet color.

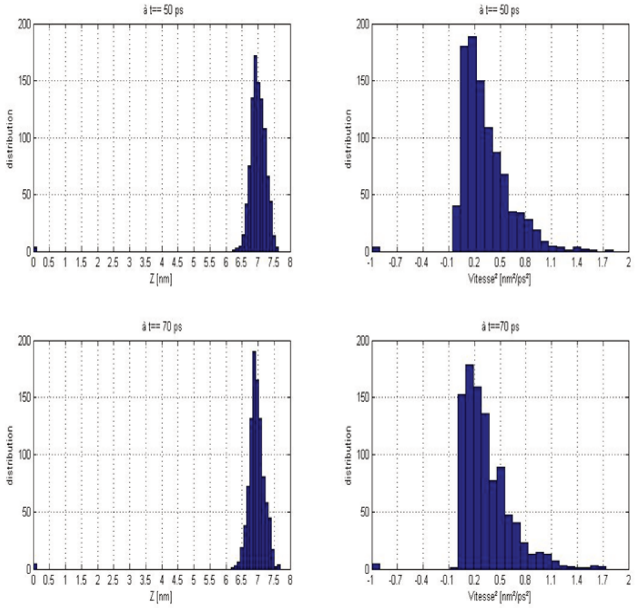

FIGURE 5.15: Distributions at T=240 K represented at different times of the trajectories from t=0 ps to t=70 ps. On the left: z-coordinate distribution of the water molecule center of mass ; on the right: kinetic energy distribution represented by the square velocity in $nm2/ps^2$.

5.4 Conclusion

Experimentally and with MD simulations, it is shown that water undergoes an efficient trapping on both solid and liquid butanol. MD simulations cannot capture experimental time scale but when adsorbed, water molecules seem to reside at the surface. In our simulation, it is visible that diffusion of molecules becomes more and more important as the temperature increases and consequently the mobility of the substrate. Water molecules incorporated into the bulk have a low probability to desorb. This is consistent with the water desorption characterized experimentally, where no desorbed water was detected at high temperature when the sample is liquid. This work is not finished and will be complemented by additional calculations and further analysis.

Chapter 6

Conclusions and perspectives

6.1 Conclusions

The objective of this thesis was to efficiently model atmospheric aerosols, more precisely organic aerosols, at the molecular level. This work has been done in the frame of the Labex CaPPA, more particularly the worpackage 2, which brings together different skills, with different theoretical and experimental approaches, in order to characterize the aerosols microphysical, chemical and optical properties from fundamental heterogeneous processes to remote sensing. Thereby, I had the opportunity to share fruitful discussions with experimentalists from the groups of S. Sobanska (LASIR) and D. Petiprez (PC2A) participating to the CaPPA project, and also from the group of J. Petterson (Gothenburg). These interactions helped us to clearly define the systems to be studied.

The aerosols modeled in this work, namely sea salt particles coated with organic matter and butanol aerosols, represent rather large and complex systems. The present thesis was the first work in the PCMT group (PhLAM Laboratory) dealing with modeling aerosols of this size. To achieve this target, I have employed various theoretical methods: classical molecular dynamics and hybrid quantum mechanics/molecular mechanics (QM/MM). MD simulation is an invaluable tool to study such “big “systems and to get enough details on the atomistic scale, whereas QM/MM allowed us to include explicitly the reactivity of a pollutant molecule with the model aerosol.

I used the GROMACS package to perform classical MD. One of the main difficulties I encountered was the lack of available force fields and/or the validation of the existing force fields. Concerning the AIMD and QM/MM methods, I used the CP2K package. Note that I was the first in the PCMT group to use this method and software. Apprehend CP2K was not a straightforward task, and it required a big effort to learn how to use it at a good level. I was introduced to CP2K by Vedran Miletić, from University Rijeka (Croatia) where I spent one week (V. Miletić is now in Heidelberg as a post-doc). He helped me for the first steps, especially how to transform the GROMACS input files to the CP2K format.

One of the greatest challenges in the theoretical modeling is to connect our results with experimental data. Often space or time scales accessible by the experiments are far away from the ones that can be simulated in our theoretical studies, with sometimes a difference of several orders of magnitude. Nevertheless, in this thesis, I took up this challenge by applying the previously mentioned methods to 4 cases:

i) In a first study, we have considered the formation of PA self-assembled monolayer on a dry NaCl(100) surface, using classical MD. We have demonstrated a clear dependence of the structural properties on both coverage and temperature. At low coverage, the PA cover exhibits a liquid-like behaviour characterized by a broad tilt angle distribution. For higher coverages, a well structured organization typical of self assembled monolayer is observed. A publication on this study is in preparation.

ii) In a second step, we have studied the water-induced organization of a palmitic acid coating at the surface of a sea salt particle. We have evidenced the occurrence of PA islands induced by the presence of water at the surface of the salt. The mechanism of islands formation and their structure has been described in details. The experimental results revealing an heterogeneous surface coating [19] are thereby well supported by our results. Subsequently, depending on the relative humidity, the hydrophilic/hydrophobic character of the sea salt surface can change. This heterogeneous coating gives rise locally to very different surface properties and hence may affect the transfer of gas phase species to the salt and their reactivity.

iii) In the second part of my thesis, I have used AIMD and QM/MM methods (CP2K), to model the NO_2 reactivity on dry and wet NaCl surface. The first studies of this system indicate a fast dissociation of the NO_2 cis-dimer, with evidence for water implication in this process. In the near future, some simulations need to be prolongated and the dependency with respect to the initial configuration needs to be checked. In addition, the analysis will be improved. A publication should be written within the next few months.

iv) I have also worked on the modelization of n-butanol crystal and water accommodation on the organic surface layers. We managed to reproduce the crystal structure and the melting point of the n-butanol crystal in good agreement with experimental values. Moreover, in the context of this study, I tutored a student, Yassine Bouchafra, during his master project. In a second step, we have modeled the collision of a water jet with the n-butanol surface, to compare with experimental results obtained in the group of Prof. Jan Petterson. These results show a qualitative agreement with the experimental results. The statistical analysis will be improved, binding and kinetic energy distributions will be calculated. Also angular distributions of the scattered molecules will be extracted. This study will give rise to a joined publication with Prof. Jan Pettersson.

6.2 Perspectives

In the short term, the projects on the n-butanol and NO_2 system previously described will be completed. But in the long term, I would like to improve the molecular modeling of the marine aerosols in order to:

i) bring a significant contribution to the general understanding on marine organic aerosols, from their formation to their transformation.
ii) bridge the gap between fundamental chemistry and chemically complex systems

iii) contribute to meaningful parametrizations in atmospheric chemistry models

Indeed, as already mentioned in this thesis, seas and oceans are the largest sources of aerosols with 50% of global emission, and there are still open questions [7, 12, 162] about the formation of heterogeneous organic marine aerosols and their reactivity. We think that molecular modeling can shed light on marine organic aerosols formation and their transformation in SOA in the atmosphere. We hope also that this can contribute to reduce the uncertainties connecting radiative forcing and secondary organic aerosols (SOA) [3]. There are some experimental studies concerning marine aerosol formation [33, 163], but to my knowledge, there are only few theoretical studies dealing with this problematic. Marine aerosols properties are determined by the composition of sea surface organic enriched monolayer (see Fig. 6.1). The ions, inorganic components present in sea water and their interaction with the organic matter greatly influence the properties of the marine aerosols.

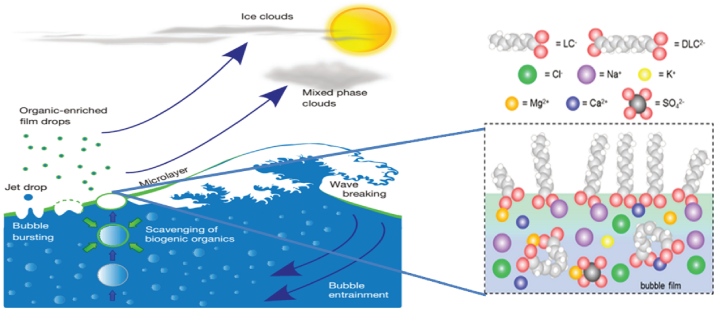

FIGURE 6.1: Creation of marine aerosol, organics from the surface microlayer are launched in the atmosphere by bubble bursting (left part). Structuralization of organic fraction in primary marine aerosols is highly influenced by presence of different ions detectable in the sea (right side) [33, 38].

The implication of ions and of the type of organics on aerosol formation/ properties remains poorly understood.

1. What is the influence of ions, organics, mixing state on nucleation, growth, hygroscopicity, cloud droplet activation potential of these aerosols ?

2. What are the mechanisms implied in the organics aging processes? Heterogeneous/ multiphase chemical reactions, mass transport, phase transitions, surface versus bulk process...?

3. What are the products issued from SOA formation?

To address these questions, the model SSA used in this thesis has to be improved, in order to be more representative of an ionic solution mixed with organic matter:

i) in a first step, we can study the hygroscopicity change with respect to the length of the carbon chain of the fatty acid for example,

ii) we can include a mixture of organic molecules, and study the effect of changing the composition of this mixture on "blocking" interfacial transport,

iii) it would be interesting to study the specific organization of the organic coating induced by solvated ions, and the effect on hygroscopic properties of the modeled particles (when varying the humidity),

iv) finally, we should study the reactivity of the formed particles, i.e; aging upon oxidation or interaction with gas phase species such as NO_x, O_3, OH, Cl to form SOA.

As a final conclusion, this thesis is a valuable experience that confirms my wish to purchase research in physical chemistry. The skills I have acquired and the collaborations I have established will be highly beneficial for my future career.

Appendix A

GROMACS to CP2K transfer tutorial

During my research, to improve my model system and to treat it quantum mechanically, need to change modelling tools appeared. The equilibrated system created by GROMACS software required to be transferred to CP2K program package. This means that all information about atomic force field parameters and molecular connectivity need to be rewritten in a new format. This is not a problem for a small system of a few 10s of atoms since it can be done manually in a reasonable time. But when one deals whit a large and heterogeneous system, this becomes a tedious job. Hereby I will present the transfer procedure step by step.
Procedure represented here is done on unix/linux distribution and generally it is not possible to do with other operating system. Also it was necessary to install acpype, openbabel and VMD.

CP2K is a versatile program and has more options to define topology and input parameters (see CP2K connectivity). For this purpose, we use a PSF file to determine the connectivity. PDB files are used for coordinates and force field parameters are defined in PRM files. PSF and PRM files are part of the CHARMM distribution (see CHARMM).

My system consists of PA, water, Na and Cl ions. For each of these molecules, intermolecular connectivity needs to be defined. In GROMACS this is done through ITP and TOP files. When using CP2K, this files can not help us. Solution to this is to take PDB structure of each molecule separately and, by using acpype software, to create other type of connectivity file. Then either RTF or PRM files can be used in the VMD plugin "Automatic PSF builder" to create one single PSF file which is then used in CP2K. Above mentioned procedure now will be explained step by step:

1. First we create the pdb file for each molecule, for example PalmiticAcid.pdb. This file can either be downloaded directly from some internet data bases or in my case extracted from model system using VMD.

2. Next we employ acpype (command line: $acpype.py - iinputfile.pdb$) to create topology files which are input files for VMD plugin. As already mentioned, acpype works for just one residue at the same time so one needs to execute acpype residue by residue and after combine all together. Output of this step are connectivity and force field files. What we use afterword are RTF files.

3. When we have all necessary RTF files, we can proceed with VMD plugin to build one PSF connectivity file.

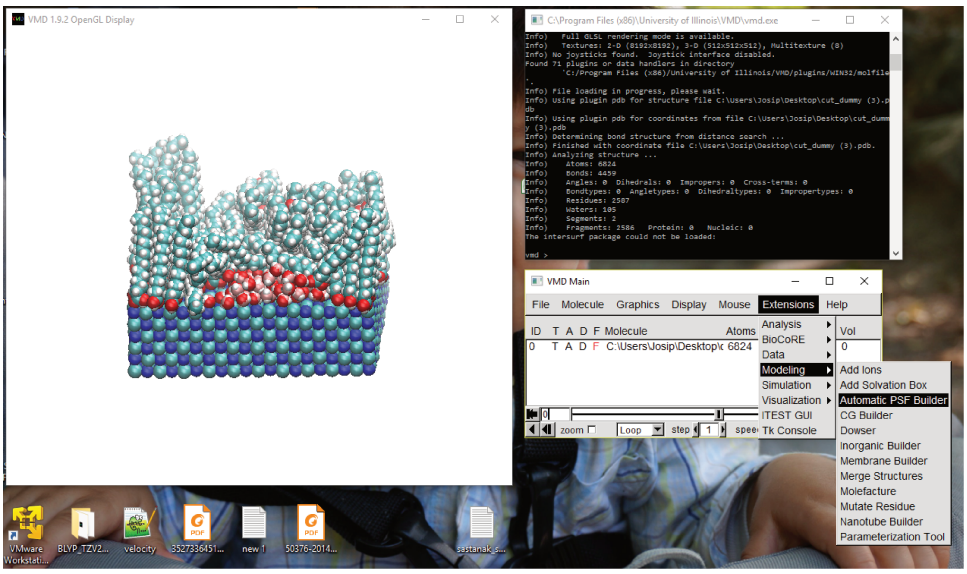

FIGURE A.1: VMD PSF builder plugin.

On Fig. A.1 is visible how PSF builder, VMD plugin, is accessed. Next if click on $AutomaticPSFbuilder$ a new window will appear, (Fig. A.2).

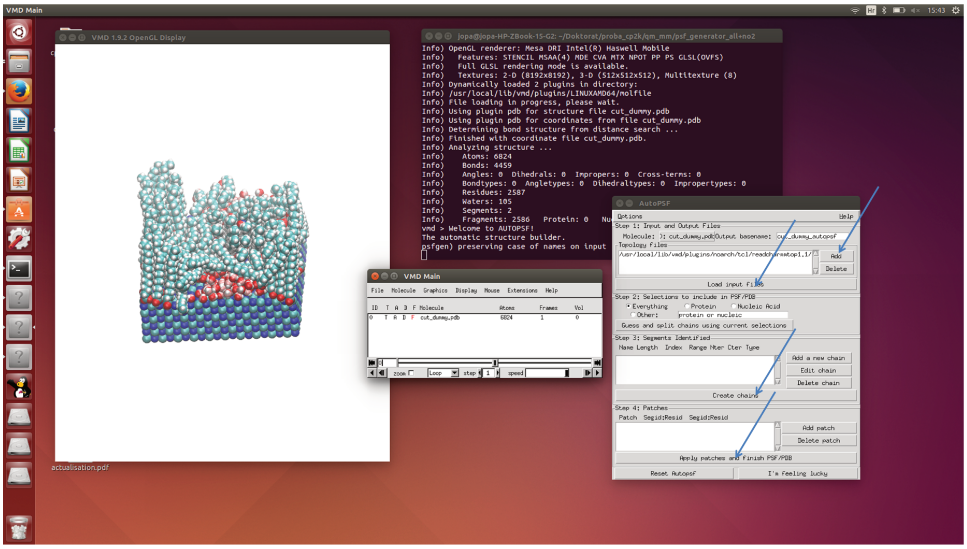

FIGURE A.2: VMD PSF builder plugin, execution.

First we need to load RTF files in the section $Topologyfile$ (Fig. A.2). Then, by simple clicking on the marked fields PSF connectivity file will be created and it is ready to be used by CP2K program.

PSF file provides just connectivity information about system and force field parameters are not written inside. This files are created in the second step by the acpype software and generally can be directly used. But often these parameters do not correspond to the right values and they need to be checked carefully.

Appendix B

Butanol improved force field, parameters adjusted to gromacs formats

Dihedral parameters adapted from periodic type to Ryckaert-Bellemans functions. Further information available in GROMACS manual [69].

TABLE B.1: Improved dihedral parametrization for carbohydrates [159].

C0 [$kJ/molA^2$]	C1 [$kJ/molA^2$]	C2 [$kJ/molA^2$]	C3 [$kJ/molA^2$]	C4 [$kJ/molA^2$]	C5 [$kJ/molA^2$]	dihedral type
0,65084	1,95253	0	-2,60338	0	0	CT- CT- CT- x
0,66944	2,00832	0	-2,67776	0	0	CT- CT- CT- HC
0,66944	2,00832	0	-2,67776	0	0	CT- CT- CT- HC
1,71544	0,96232	0	-2,67776	0	0	CT- CT- OH- HO
0	0	0	0	0	0	CT- CT- x- HA
0,65084	1,95253	0	-2,60338	0	0	x- CT- CT- HC
0,65084	1,95253	0	-2,60338	0	0	x- CT- CT- HC
0,65084	1,95253	0	-2,60338	0	0	OH- CT- CT- CT
1,046	-1,046	0	0	0	0	OH- CT- CT- HC
1,046	-1,046	0	0	0	0	OH- CT- CT- HC
0,65084	1,95253	0	-2,60338	0	0	HC- CT- CT- CT
0,65084	1,95253	0	-2,60338	0	0	HC- CT- CT- HC
0,65084	1,95253	0	-2,60338	0	0	HC- CT- CT- HC
0,69733	2,092	0	-2,78933	0	0	HC- CT- OH- HO
0,65084	1,95253	0	-2,60338	0	0	HC- CT- CT- CT
0,65084	1,95253	0	-2,60338	0	0	HC- CT- CT- HC
0,65084	1,95253	0	-2,60338	0	0	HC- CT- CT- HC
0,69733	2,092	0	-2,78933	0	0	HC- CT- OH- HO
0,6276	1,8828	0	-2,5104	0	0	HC- CT- CT- HC
0,6276	1,8828	0	-2,5104	0	0	HC- CT- CT- HC
0,6276	1,8828	0	-2,5104	0	0	HC- CT- CT- HC
0,6276	1,8828	0	-2,5104	0	0	HC- CT- CT- HC

Appendix C

Water-Induced Organization of Palmitic Acid at the Surface of a Model Sea Salt Particle: A Molecular Dynamics Study

THE JOURNAL OF PHYSICAL CHEMISTRY A

Article

pubs.acs.org/JPCA

Water-Induced Organization of Palmitic Acid at the Surface of a Model Sea Salt Particle: A Molecular Dynamics Study

Josip Lovrić, Denis Duflot, Maurice Monnerville, Céline Toubin, and Stéphane Briquez*

Laboratoire de Physique des Lasers, Atomes et Molécules (PhLAM) CNRS, UMR 8523, Univ. Lille, F-59000 Lille, France

Supporting Information

ABSTRACT: Marine aerosols represent the most important aerosol fraction in the Earth atmosphere. Field studies have revealed that fatty acids form an organic film at the surface of sea salt particles, altering the properties of the aerosol. By means of classical molecular dynamics simulation, the surface organization of palmitic acid (PA) on a salt surface, NaCl, has been investigated at two different temperatures, 235 and 300 K, and with relative humidity varying from 0 to 40%. Calculations show that water promotes the formation of well-ordered close-packed PA islands. As a result, some area of the salt may be covered by water only or by PA molecules supported by water. Depending on the relative humidity, the hydrophilic/hydrophobic character of the sea salt surface varies. This heterogeneous coating gives rise locally to very different surface properties and hence may affect the transfer of gas phase species to the salt and their reactivity.

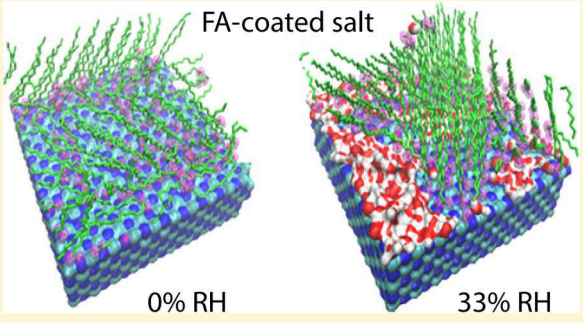

INTRODUCTION

Aerosol particles play an important role in the global climate system.[1] By scattering solar radiation they influence the global energy budget and then the climate directly. Aerosols have also an indirect effect on the climate system[2−4] because they can act as cloud condensation nuclei (CCN), impacting cloud properties (number, size of droplets), on which scattering of solar radiation depends. Their description in climate models can strongly influence the estimated effects of anthropogenic origin on future climate.[5] Natural aerosols, from biogenic sources, dust, or sea salt contribute to a large part of uncertainty in present day aerosol forcing.[6] In addition, the response of the climate system to anthropogenic aerosol perturbations depends strongly on the natural aerosol background. In order to simulate the evolution of the climate from the preindustrial era, with an atmosphere containing only natural aerosols, to the present day and future, it is then crucial to understand the properties of these natural aerosols. Moreover, the emissions of these natural aerosols in the atmosphere can also be affected by climate change. This climate feedback can amplify or dampen the effect of a forcing.[7]

Among natural aerosols, sea salt aerosols (SSA), with estimated annual emissions of 2−10 Pg/yr, represent the major component of primary marine aerosols by mass.[8−10] SSA particles originate from bubble bursting at the ocean surface and are predominantly produced from the microlayer at the sea−air interface where organic matter of biological origin is accumulated.[11−13] The evaporation of sea spray in the marine boundary layer produces numerous liquid or solid particles whose bulk chemical content reflect the initial composition of the surface seawater. SSA, containing mainly sodium and chloride, but also smaller amounts of sulfate, potassium, magnesium, and calcium, are the main source of atmospheric sodium and chloride in coastal regions.[14] Moreover, organic compounds may represent a large fraction of the aerosol mass.[10,15,16] Depending on the biological activity of the region, this organic mass can reach up to 60% of the aerosol mass.[17] Field measurements have shown that SSA particles contain fatty acids (FA),[18−20] mostly myristic acid (C14), palmitic acid (C16), and stearic acid (C18). This FA content strongly depends on the location, season,[21] and size of the aerosol particle. Indeed, recently, Grassian et al. have performed an analysis of organic content in fine and coarse SSA.[22] They have found that fine SSA (<2.5 μm) are more enriched with organics than coarse SSA (2.5−10 μm). Fine SSA exhibit higher densities in FA with shorter chains (C9, C10, C12, and C14). At relative humidity (RH) lower than 40%, SSA particles consist of NaCl cubes of a few micrometers with a FA layer[23−25] that covers 0.3 to 14% of the collected sea salt particles.[11,19] Recently, the use of cryogenic transmission electron microscopy (cryo-TEM) allowed to get a more precise view of the chemical complexity and structure of SSA.[26] Sea spray aerosols appear to be a complex mixture of biological and chemical constituents, with, for example, the formation of NaCl dendrites on the surface, when exposed to a lower RH. The presence of an organic coating can modify the physical and chemical properties of the aerosol.[27,28] It may act as a barrier decreasing the mass transfer across the interface, lowering uptake of atmospheric species[28−30] or preventing reactions between gas reactants and particle surface, such as reaction between NaCl and

Received: August 2, 2016
Revised: December 4, 2016
Published: December 7, 2016

DOI: 10.1021/acs.jpca.6b07792
J. Phys. Chem. A 2016, 120, 10141−10149

NO_2, leading to ClNO(gas) + $NaNO_3$ (solid).[18,31] The presence of water in/on these aerosols can also have a strong influence on the adsorption of atmospheric gases, the organization of the organic film at the surface, and their chemical reactivity.[28,32]

Although numerous works have been carried out on this topic in recent years, there is still much uncertainty remaining about the physical and chemical properties of marine aerosol particles.[10] Several experimental studies about the effect of organic surfactants (stearic, palmitic, and oleic acids) on aerosol particles (NaCl, ammonium sulfate, etc.) have been carried out at different relative humidities.[33−41] For example, Sobanska et al.[42] have studied the effect of stearic acid (SA) coating on the reactivity of NO_2 with the NaCl(100) surface under various humidity conditions, using atomic force microscopy (AFM), Raman imaging, and time-of-flight secondary ion mass spectrometry (ToF-SIMS). They have observed heterogeneous coating with SA monolayer islands. This heterogeneous coating slows down but does not prevent the transfer of NO_2 and H_2O molecules toward the surface of the crystal, at low humidity (20 to 50%). Their results emphasize the role of humidity in the stability of FA islands coating.

The goal of the present article is to investigate water and FA organization at the salt surface by means of classical molecular dynamics (MD) simulations. This approach is indeed an efficient method giving structural and dynamical information for rather large systems provided the processes do not imply charge transfer, bond breaking, etc. Few MD calculations have been performed to model sea salt particles with organic molecules.[43−46] Previous studies have mostly focused on Langmuir monolayer at the air−water interface,[44,47−49] on water droplets,[43,45] and on nanoparticles.[46] For instance, Chakraborty and Zachariah[45] have investigated the effect of FA, especially of their chain length, on the morphology and properties of water nanodroplets coated with FA. Their results indicate that, for particles coated with long-chain FA, the chains tend to align parallel to each other, lowering the sticking coefficient of water vapor on such particles, whereas particles coated with shorter chains FA are more hydrophilic. Moreover, Takahama and Russell[44] have simulated impinging water vapor molecules on a slab of water coated by monomolecular organic films. The mechanism of sticking is shown to depend on the organic compound, packing density, and resulting surface structure. In addition, MD simulations of water vapor interacting with sodium dodecyl sulfate (SDS)/NaCl slabs[46] indicate that SDS kinetically hinders the initial water uptake partly due to the ordering of the SDS chains as the coverage increases. The group of Paesani has investigated the physical properties of Langmuir monolayers of palmitic acid (PA) and dipalmitoylphosphatidic acid (DPPA) at the air−water interface or on air−NaCl solution interfaces through MD simulations.[48] They focused on spatial and chain tilt ordering as a function of surface pressure. They considered PA molecules to be neutral, as assumed in our study. Surface-sensitive spectroscopic studies have shown that, at pH = 6, the PA head groups are mostly protonated.[50] Most of the studies have focused on the effect of a full organic-coated water slab or nanodroplet on the sticking of incoming water molecules. As a complement to these studies, the purpose of the present study is to understand the effect of humidity on the organization of the coating for a partial coverage of the salt surface.

This article is organized as follows: Section II presents the computational details and the description of the model system, results and discussion are presented in Section III, and finally some conclusions are given.

METHODOLOGY AND SYSTEM

Methodology. All the classical MD simulations presented hereafter have been carried out using the GROMACS package,[51] well adapted for parallel computing. The OPLS all-atom force field[52] was employed to model the PA molecule. This force field has been designed for organics in solution and gives reasonable estimations of various properties (density, enthalpy of vaporization, heat capacities, surface tension, etc.) for a significant number of organic molecules.[53] In addition, it has been shown that OPLS force field models efficiently organic monolayer/water systems.[54−56] For the description of the NaCl substrate, different force fields[57] can be found in the literature. Among those, the force field developed by Smith and Dang[58] was chosen because it gives a lattice parameter consistent with the experimental value.[57] The three-site SPC/E force field was used to model water as it is optimized for interactions with organic molecules.[59] Moreover, the SPC/E model is known to reproduce correctly the surface tension of water,[60] this property being critical for studying interfaces. In the present study, as previously mentioned, the PA molecules are considered to be neutral.

The equations of motion were integrated using a leapfrog algorithm.[61] The LINCS algorithm[62] was used to constrain the bonds, which made possible the use of a 2 fs time step. Temperature and pressure were held at the desired values using the V-rescale algorithm[63] and the Berendsen barostat[64] with coupling times of 0.1 and 2 ps, respectively. Standard periodic boundary conditions have been applied. Lennard-Jones and short-range part of the electrostatics were truncated with a cutoff distance of 1.4 nm. Long-range electrostatic interactions were treated with the Particle Mesh Ewald method, with a relative tolerance of 10^{-5}, fourth-order cubic interpolation, and a Fourier spacing parameter of 0.6.

System. The NaCl crystal was built by placing the Na and Cl atoms in a fcc crystal with a lattice constant of 0.56 nm corresponding to the experimental value.[65] After a minimization with the steepest descent algorithm and a short relaxation (100 ps) in the NVT ensemble at 235 K, the lattice parameter of the crystal converged to 0.54 nm. The crystal was then equilibrated in the NPT ensemble at T = 235 K during 150 ps giving a final crystal lattice equal to 0.56 nm. Before introducing water and PA molecules, a NaCl slab was created by extending the size of the box along the z-direction, both in positive and negative directions. The crystal was centered in the simulation box with dimensions of 5.5 × 5.5 × 40 nm in x, y, and z, respectively.

As shown in earlier studies,[66,67] water tends to form a monolayer at the salt surface. We chose thus to adsorb in a first step water on NaCl and second exposing it to vaporized PA. Subsequently, for the various water coverages investigated, the water/NaCl system was first relaxed over 2 ns in the NPT ensemble before introducing PA molecules. The water molecules formed, as already evidenced from previous studies,[68] a monolayer on the substrate, with the water oxygens being adsorbed on top of the sodium ions. Since the surface layer of NaCl in our simulated system consisted of 200 Na−Cl pairs, 200 molecules are required to form a full water monolayer (100% WM). RH can also be connected to the amount of adsorbed water. The adsorption isotherms of water on NaCl published by Foster and Ewing[66] was used to connect the number of water molecules present in our simulation to RH as shown in Table 1. It is also important to stress that the present work considers submonolayer or monolayer water coverage, that means far

DOI: 10.1021/acs.jpca.6b07792
J. Phys. Chem. A 2016, 120, 10141−10149

Table 1. Relative Humidity (RH) Determined from the Adsorption Isotherms[66] and the Corresponding Water Coverage with Respect to the Full Monolayer (WM)

RH (%)	% WM
0	0
20	25
33	50
40	100

below the deliquescence limit of the salt, which appears above a coverage of four water layers.[66] In their MD simulations, Bahadur and Russell have shown that the deliquescence properties of NaCl nanoparticles are size dependent for particles smaller than 100 nm, deliquescence relative humidity (DRH) ranging from 75% for particles larger than 100 nm to 90% for a 2.2 nm particle.[69] On an infinite perfect crystal, deliquescence can occur only if voids are introduced,[70] which is not the case in the present study. Even if the validity of our RH definition may be questionable when PA is included in the system, RH, rather than the number of water molecules, will be used for comparison with the experiments and discussion of the atmospheric implications.

As performed in the experiments of Sobanska et al.,[42] the salt crystal was then exposed to vaporized PA at different humidity conditions. Small amounts of PA were added on the water/NaCl substrate by means of 16 chains regularly distributed on top of the surface with the COOH group oriented toward the substrate. After each addition, the PA molecules were relaxed on the water/NaCl substrate for 2 ns in the NPT ensemble. Several PA coverages were produced likewise. The number of PA molecules can also be expressed in terms of surface coverage. Considering the atom electronegativity and comparing with previous results on acid coating of water droplets,[45] we can expect that the COOH group of a PA molecule adsorbs preferentially on top of a NaCl pair and that their chains align perpendicularly to the surface. Since the modeled NaCl sublayer is composed of 200 Na^+ or Cl^- ions, 200 PA molecules would correspond to a full theoretical monolayer (TM). In the following, the PA coverage will thus be expressed with respect to the full TM. When the desired amount of PA was adsorbed, a 50 ns trajectory was propagated for the entire system and the last 10 ns were used for the analysis.

Figure 1 illustrates the initial state for the simulation of the 50% TM PA-coated NaCl surface and 40% RH. Water forms a monolayer on the NaCl substrate, and PA molecules are added step by step from the gas phase until the desired coverage is reached. It should be noted that the effect of the initial configuration on the results has been investigated by exposing first the NaCl surface to PA and second to water. The analysis of the equilibrated system showed no significant dependence on the initial setup, except that, in the case where NaCl was first exposed to PA, the equilibration process required more computational time. When NaCl is first exposed to water, the equilibrium is quickly reached after a few ns. The complete analysis was performed with the trajectories obtained with this initial configuration (PA adsorbed on wet NaCl). Fifty nanosecond trajectories were subsequently sufficient, and the last 10 ns have been used for the statistics. At the same PA and water coverages (50% TM and 50% WM), the number of hydrogen bonds formed between PA and water has been monitored at each time step for the two different initial conditions as depicted in Figure 2. Hydrogen bonds were formed more rapidly when water was

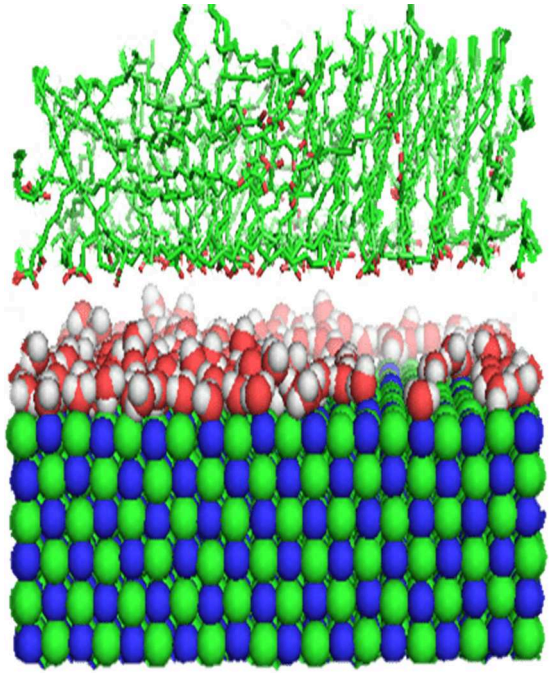

Figure 1. Molecular view of the initial configuration for 50% TM PA coverage and 40% RH. In the space-filling model, Na and Cl atoms are represented in blue and green, respectively, and water in red (O atoms) and white (H atoms). PA molecules are initially placed 0.3 nm above the surface.

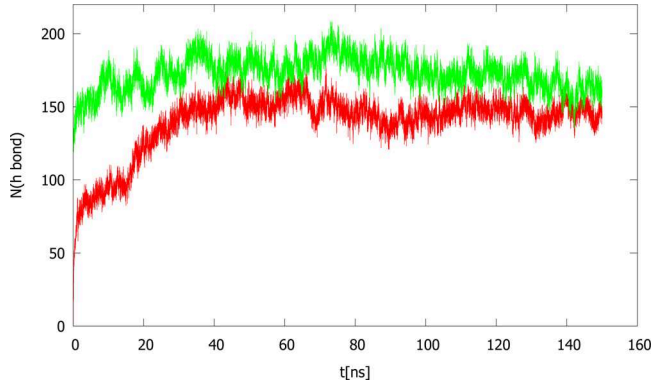

Figure 2. H-bond formation between water and PA functional group for two different initial conditions: PA adsorbed on wet NaCl (green) and PA adsorbed on dry NaCl, followed by water exposure (red). Fifty percent PA TM coverage and 33% RH in both cases.

first adsorbed on NaCl, but after 45 ns, both trajectories converged to a comparable number of hydrogen bonds formed. This criterion is of importance since hydrogen bonding is actually a driving force in the organization of such a system.

RESULTS

Evidence for PA Islands Formation. The experiments carried out by Sobanska et al.[42] showed that when increasing RH from 20% to 50% at 293 K, the salt surface covered by SA significantly reduces from 60 ± 5% to 50 ± 4%. No other morphological changes like reorganization, folding, or multilayer formation were observed. Although the present study focuses on PA, it should be noted that, since PA and SA differ only by two carbons, no significant difference in their physical properties should be expected.

DOI: 10.1021/acs.jpca.6b07792
J. Phys. Chem. A 2016, 120, 10141−10149

Salt area covered by the PA molecules is obtained by calculating 2D densities histograms (projected density on the $x-y$ plane) for the carbon atoms over the 500 ps equilibrated trajectory. For a coverage of 24% TM, PA molecules cover approximately 80% of the surface at 300 K in dry conditions, and upon introduction of water (33% RH), its surface occupancy decreases to 64% at the same temperature. This is illustrated by the snapshots shown on Figure 3. At 50% TM and 300 K, a

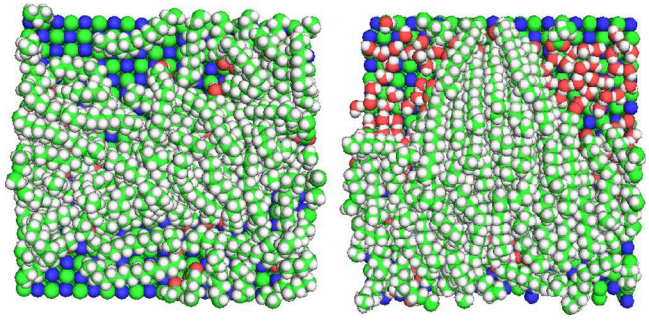

Figure 3. Top view of configurations issued from the simulation for a PA coverage of 24% TM and 0% RH (left panel) and 33% RH (right panel). PA chains are represented with green (carbon) and white (hydrogen) colors. T = 300 K in both cases.

similar trend is observed, the coverage changing from 99% to 91% of the surface under dry and 33% RH conditions, respectively. In the presence of water, PA seem to accumulate on some areas forming "islands". The formation of close-packed PA islands leads to an increase of available surface for water or incoming species, showing that not only the quantity of surfactants matters, but also their surface organization. At lower temperature (235 K), despite a reduced mobility of both water and PA molecules, island formation is still observed (see Supporting Information).

Structural Organization. To mimic the experimental conditions of the work of Sobanska et al.,[42] all the results discussed thereafter were obtained using a PA coverage equal to 50% TM. The density profiles give an average view of the distribution of the species along the surface normal (z-axis) (Figure 4). At low humidity, the H atom of the acidic function, labeled H1, is preferentially bound to the salt surface as shown from the intense peak at 0.2 nm from the surface on Figure 4. Some PA molecules are also adsorbed having their COOH group further away from the surface, as materialized by the broad peaks spreading between 0.3 and 0.55 nm away from the surface and more easily distinguishable at 33% than at 20% RH. As the humidity is increasing from 33% to 40%, the peak characteristic of direct interaction of the COOH moiety with the salt is decreasing (Figure 4a), whereas a single broad peak is growing with a maximum around 0.45 nm from the substrate.

For the interpretation, these features need to be correlated to the water densities (Figure 4b). From 20% to 33% RH, a well-defined peak close to the substrate (0.33 nm) is growing, indicating a stable adsorption of water on the ionic substrate. In addition, for these humidity conditions, water densities present a shoulder around 0.31 nm, as a sign of multilayer growth on some areas of the substrate. The broad peaks, with maxima around 0.33 and 0.47 nm, observed on the PA densities correspond thus to adsorption of PA on these water monolayer or multilayer-covered spots, respectively. Water density at 40% RH is still characterized by a peak close to the substrate with almost the same intensity as that at lower humidity, but the distribution

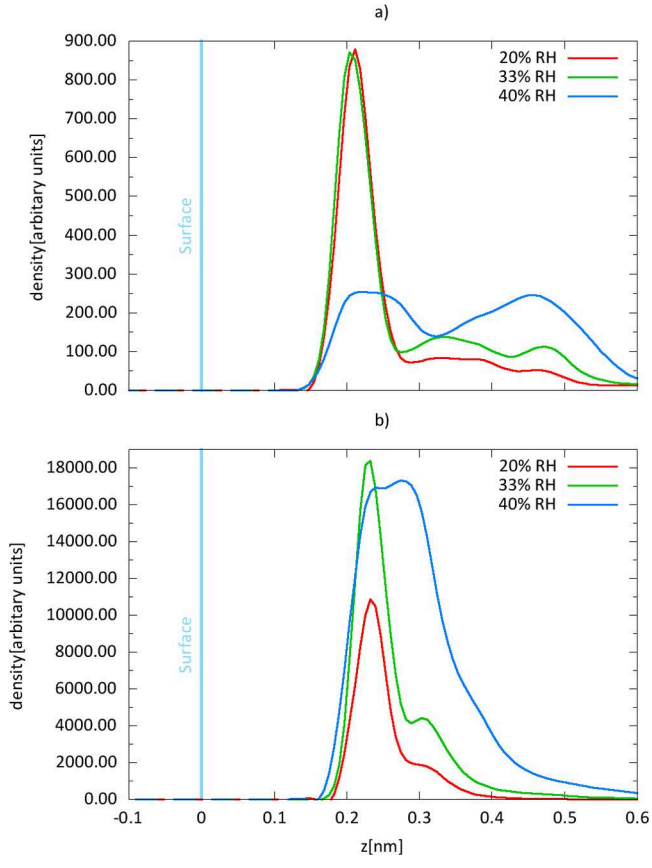

Figure 4. (a) PA (H1) densities along the z-axis. (b) Water (O) densities along the z-axis. All the densities are calculated for a PA coverage equal to 50% TM at T = 300 K.

broadens (40% RH), indicating that the water molecules spread along the normal to the surface forming 3D aggregates, the size of these aggregates varying from one site to another. Most of the PA adsorb on top of these water clusters, this is characterized on the H1 density by a broad peak ranging from 0.28 to 0.6 nm (with the maximum around 0.45 nm). It is worth mentioning that 40% RH corresponds theoretically to a full monolayer of water on bare NaCl, but actually, some areas of the salt are not covered by water, but by PA instead. The fact that the water molecules are not all physisorbed on the salt allows the formation of 3D clusters in other places.

To summarize, when the amount of adsorbed water is not sufficient to cover the whole salt surface, PA will preferentially bind to the salt through its hydrophilic functional group (H1 of COOH) to optimize the electrostatic interaction. For higher humidity conditions (40% RH), PA adsorbs on top of the water clusters. These results provide evidence again for an inhomogeneous PA coating on the salt and the strong influence of water in the organics organization.

The orientation of the PA molecules has been characterized. PA orientation is described by the tilt angle, between the molecular axis and the surface normal (z-axis). Two vectors, C1−C16 and C1−C8, are used to define the molecular axis, with C1 referring to the carbon carrying the acidic function (hydrophilic head) and C8 and C16 corresponding to carbons in the middle of the chain or at the end (hydrophobic tail), respectively. The C1−C8 vector is used to check whether the chain is bent or not. A molecule lying flat on the surface corresponds to a 90° tilt angle. On the opposite, a molecule standing up is characterized by a tilt

DOI: 10.1021/acs.jpca.6b07792
J. Phys. Chem. A 2016, 120, 10141−10149

angle smaller than 45°. Figure 5 represents the angular distributions at T = 300 K with increasing RH and for a PA

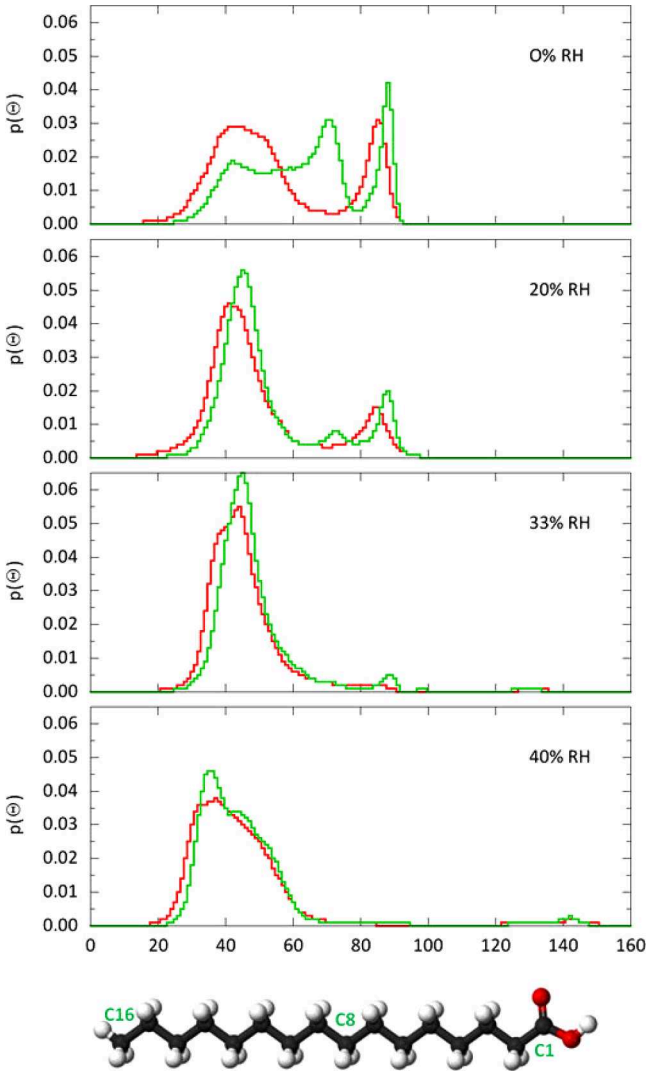

Figure 5. Angular distribution characterizing the inclination of the PA chain, i.e., C1−C8 vector (red line) or C1−C16 vector (green line) with respect to the z-axis perpendicular to the surface. PA coverage is equal to 50% TM and T = 300 K.

coverage of 50% TM. Under dry conditions, two orientations can be distinguished: a tilted orientation of the C1−C16 axis, with angles between 30° and 70° with respect to the surface normal, and a flat orientation of the molecule (close to 90°). Without water present on the salt, and at this PA coverage, the molecules can either stand up or lie flat on the surface. Differences between the C1−C8 and C1−C16 tilt angle distributions are indicative of chain bending. As the humidity increases, both distributions get nearly superimposed and the flat orientation signature disappears. PA chains in the "trans" conformation align nearly parallel to each other with a tilt angle ranging from 30° to 60°. Indeed, when RH increases, PA molecules tend to reproduce self-assembled monolayers (SAM) islands with well-organized chains. This organization resembles the structure of FA self-organized Langmuir monolayers at the air−water interface[45,56] with the polar head of surfactant molecules binding to the water molecules and the hydrophobic hydrocarbon chains oriented toward the gas phase. Tilt ordering has been also extensively studied in the context of SAM of organic molecules adsorbed on different solid substrates (metal, semiconductor, or oxide).[71,72] The growth of a SAM relies on a subtle balance between substrate−headgroup and chain−chain interactions. If the substrate−headgroup interactions are not too strong, allowing molecules to rearrange laterally after adsorption at the surface, it can lead to the production of a SAM with high packing density through chain−chain interactions. In the literature, the tilt angle for SAM of organics on solid substrate can vary from one molecule to another one, but is typically less than 30°.[71] Our values are larger due to the fact that in our heterogeneous system water is modifying their chain organization, and the FA chains are not as packed as in SAM.

This conclusion (inhomogeneous coating in the presence of water) supports experimental results and related assumptions of Sobanska et al.[42] Lower temperature (235 K) distributions exhibit the same trends but in a less remarkable manner (see Supporting Information), the smaller available thermal energy limiting the diffusion of water and the reorientation of the PA.

Bonding Properties. Figure 6 depicts the PA−water energy distribution, this energy characterizing the interaction of one PA

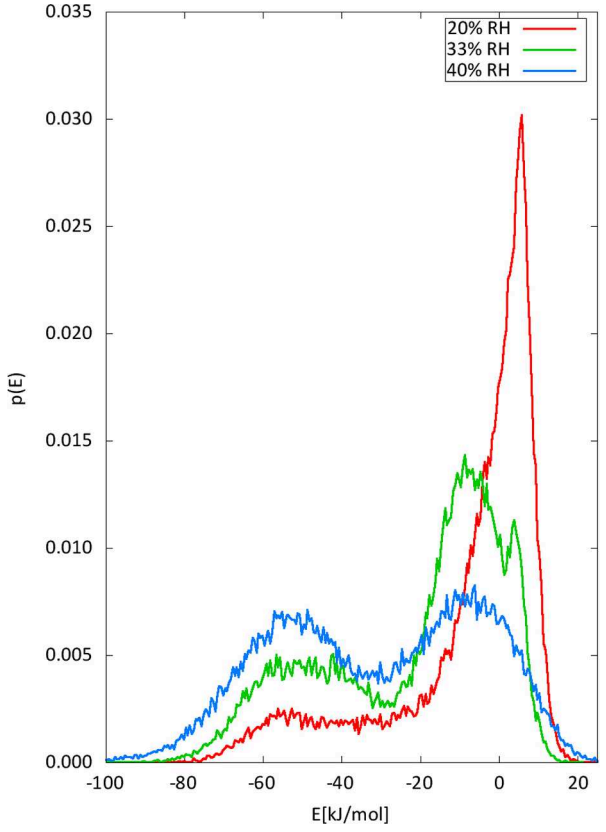

Figure 6. PA−water energy distribution diagrams for different humidities (T = 300 K). PA coverage is equal to 50% TM.

molecule with the surrounding water molecules. At low humidity (20% RH), a peak corresponding to a slightly positive interaction is dominant as a sign of a repulsive interaction between PA chains and water. As humidity increases, this peak decreases and gets displaced toward negative values, down to −10 kJ/mol. In addition, a broad peak ranging from −35 to −70 kJ/mol is growing upon water addition, as a signature of hydrogen bond formation (2 or 3 per PA) between PA and water. When the number of water molecules becomes important, water tends to

DOI: 10.1021/acs.jpca.6b07792
J. Phys. Chem. A 2016, 120, 10141−10149

find its way toward the PA functional group. Actually, these results are connected to the densities discussed previously: water tends to be inserted between the salt and the PA, forming H-bonds with the COOH group. This mechanism of energy exchange between surface, water, and then PA directly favors the creation of self-assembled PA islands on the NaCl surface.

As already mentioned, the mechanism of self-assembly is driven by two effects: on one hand H-bond formation, as shown in Figure 2 and, on the other hand, van der Waals lateral interaction between carbon tails. Figure 7 represents the distribution of the interaction energy between PA molecules as a function of humidity for a given coverage (50% TM). Upon humidity increase, the distribution gets narrower, as a sign of orientational ordering. Moreover, two peaks are observed at high humidity. The higher peak (∼−200 kJ/mol) can be attributed to molecules inside a PA island, strongly bound to other PA molecules. By contrast, molecules at the edge are, on average, bonded to fewer molecules, contributing to a second peak at lower energy (∼−100 kJ/mol).

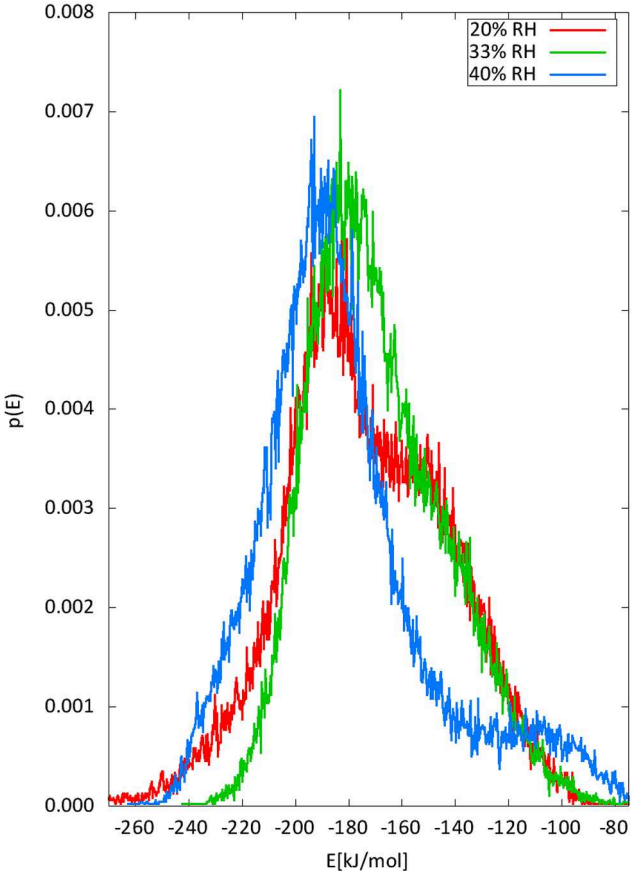

Figure 7. PA−PA energy distribution diagrams for different humidities. PA coverage is equal to 50% TM and T = 300 K.

DISCUSSION

As previously mentioned, the surface organization of FA on salt at dry and wet conditions is of fundamental importance for the condensation and nucleation of aerosol particles. PA chains, hydrophobic in nature, are directed toward the gas phase and may serve as a barrier for incoming species. A common idea is that a self-assembled FA monolayer would certainly impact water evaporation and gas uptake, but many questions remain unanswered.[29,73−75]

At coverages lower than the full monolayer, representative, for instance, of PA coverage used in the experiment of Sobanska et al.,[42] water is either adsorbed on PA free area and/or inserted between the salt and the PA carboxylic functional group, potentially favoring surface deliquescence or chemical processes implying water as a catalyst.[42] Increase of RH (at least from 0 to 40%) leads to the formation of close-packed islands covering only a fraction of the surface. The formation of holes within the organic layer may indeed facilitate the water transfer in this region. This behavior has been observed in the experiments of Garland et al.,[37] on the impact of PA coating on water uptake/loss of ammonium sulfate particles, investigated with a combination of FTIR spectroscopy, electron microscopy, and mass spectrometry. Even in small amounts, adsorbed water can diffuse through the coating and reach the salt. Consequently, water uptake may not be modified as substantially as expected. By contrast, we can assume that a full ideal FA SAM on a dry surface would prevent water or other molecules from approaching the salt. It should be noted that the water effect on FA self-assembly and surface organization may also differ with the length of the carbon chain.[75] Molecules with long chains (≥12 carbons) form close-packed organic films, while shorter chains form less structured films.

Subsequent to the heterogeneous coating of PA, additional reactive species from the atmosphere may be processed and reach the salt. In their experiments, Sobanska et al.[42] correlate the NO_2 reaction with NaCl and $NaNO_3$ formation with PA island positions. In fact, it has been shown in previous studies that water catalyzes *cis*-ONO-NO_2 dissociation,[75−77] and since water is bonded to PA islands, this reaction may be spatially correlated with PA islands. Likewise, the experiments of Ryder et al. showed that, at RH between 50% and 65%, there is no suppression in the reactive uptake of N_2O_5 due to the organic material present in SSA.[78] These experimental results are fully consistent with the conclusions of our MD simulations.

CONCLUSION

Molecular modeling of heterogeneous organic aerosol provides detailed information on the mechanisms and contributes to improvement in the understanding of cloud nucleation and also of the chemistry undergoing on aerosol surface. In the present work, classical MD simulations were employed to model PA organization on a model sea salt surface at different temperatures and humidity conditions. Humidity is shown to have a significant influence on the mechanism of FA self-assembly. Present calculations provide evidence for ordered PA island formation as observed experimentally.[42] This effect is enhanced at room temperature compared to 235 K. Since the organic coverage on aerosols can exhibit strong variations,[19] this study sheds some light on the mechanism of salt partial coating and enhanced self-assembly upon increased humidity. The coating is driven by water that provides order to the FA islands and binds preferentially to the salt. As a consequence some area of the salt may be covered by water only. Furthermore, this heterogeneous organization enables the transfer of incoming species (e.g., NO_2, O_3, Cl) from the gas phase to the water aggregates lying on the salt or to the salt itself, influencing the atmospheric reactivity of sea salt aerosols. Quantum mechanics or quantum mechanics/molecular mechanics methods could be used subsequently to investigate in detail the reactivity of gas phase molecules at this model aerosol surface. The structuration

DOI: 10.1021/acs.jpca.6b07792
J. Phys. Chem. A 2016, 120, 10141−10149

of the organic coating as a function of the RH can impact the hygroscopic properties of the SSA and their aging, and subsequently the climate evolution. The simulation of organic aerosols in global chemistry transport models (CTM) and general circulation models (GCM) varies greatly between models,[79] particularly for parameters such as aerosol aging and microphysics. Due to the complexity of the organic aerosol, and as a compromise between simplicity and accuracy, only simplified representations of organic aerosols are introduced in global chemistry climate models.[5] Even if in some of the recent global models,[80] some processes such as oxidative aging of primary organic aerosol are implemented, it should be taken into account, as shown in the present study that, even with a "simple" SSA model, the properties of the SSA aerosols can exhibit important changes in their physical (hygroscopicity) and chemical (reactive uptake) properties as a function of RH. This study aimed, in the first place, to simulate and explain the experiments of Sobanska et al.[42] It represents a first step toward a model of more complex sea salt particles. Marine aerosols are known to possess a rich variety of chemical classes in their coating. The mixing/demixing as well as the competition between the different molecules (of different lengths and weights) or ions is also believed to affect substantially their surface properties. The present work paves the way toward a more realistic description of interfacial properties of submicron aerosol particles.

■ ASSOCIATED CONTENT

Supporting Information

The Supporting Information is available free of charge on the ACS Publications website at DOI: 10.1021/acs.jpca.6b07792.

Spatial distribution of PA and water on the salt as a function of temperature; energy distributions as a function of humidity and temperature; orientation of the PA chains at low temperature (235 K) (PDF)

Animated video of a molecular dynamics trajectory illustrating formed island of PA, enhanced by the water aggregates. RH = 40%, PA coverage = 32% TM, T = 300 K (MP4)

■ AUTHOR INFORMATION

Corresponding Author

*E-mail: stephane.briquez@univ-lille1.fr. Phone: +33 (0)3 20 33 64 52. Fax: +33 (0)3 20 43 40 84.

Notes

The authors declare no competing financial interest.

■ ACKNOWLEDGMENTS

This work is supported by the CaPPA project (Chemical and Physical Properties of the Atmosphere) funded by the French National Research Agency (ANR) through the PIA (Programme d'Investissement d'Avenir) under contract ANR-11-LABX-0005-01 and by the Regional Council Nord Pas de Calais−Picardie and the European Funds for Regional Economic Development (FEDER). This work was performed using HPC resources from GENCI-TGCC (Grant 2016-086820). The Centre de Ressources Informatiques (CRI) of the Université of Lille also provided computing time. Authors would like to thank A. Habartova and S. Sobanska for the fruitful discussions.

■ REFERENCES

(1) Pöschl, U. Atmospheric Aerosols: Composition, Transformation, Climate and Health Effects. *Angew. Chem., Int. Ed.* **2005**, *44*, 7520−7540.

(2) IPCC. *Climate Change 2013: The Physical Science Basis. Contribution of Working Group I to the Fifth Assessment Report of the Intergovernmental Panel on Climate Change*; Cambridge University Press: Cambridge, United Kingdom, 2013.

(3) Lohmann, U.; Feichter, J. Global Indirect Aerosol Effects: a Review. *Atmos. Chem. Phys.* **2005**, *5*, 715−737.

(4) Finlayson-Pitts, B. J.; Pitts, J. N. Tropospheric Air Pollution: Ozone, Airborne Toxics, Polycyclic Aromatic Hydrocarbons, and Particles. *Science* **1997**, *276*, 1045−1051.

(5) Kanakidou, M.; Seinfeld, J. H.; Pandis, S. N.; Barnes, I.; Dentener, F. J.; Facchini, M. C.; Van Dingenen, R.; Ervens, B.; Nenes, A.; Nielsen, C. J.; et al. Organic Aerosol and Global Climate Modelling: a Review. *Atmos. Chem. Phys.* **2005**, *5*, 1053−1123.

(6) Carslaw, K. S.; Lee, L. A.; Reddington, C. L.; Pringle, K. J.; Rap, A.; Forster, P. M.; Mann, G. W.; Spracklen, D. V.; Woodhouse, M. T.; Regayre, L. A.; et al. Large Contribution of Natural Aerosols to Uncertainty in Indirect Forcing. *Nature* **2013**, *503*, 67−71.

(7) Carslaw, K. S.; Boucher, O.; Spracklen, D. V.; Mann, G. W.; Rae, J. G. L.; Woodward, S.; Kulmala, M. A Review of Natural Aerosol Interactions and Feedbacks Within the Earth System. *Atmos. Chem. Phys.* **2010**, *10*, 1701−1737.

(8) Vignati, E.; Facchini, M.; Rinaldi, M.; Scannell, C.; Ceburnis, D.; Sciare, J.; Kanakidou, M.; Myriokefalitakis, S.; Dentener, F.; O'Dowd, C. Global Scale Emission and Distribution of Sea-Spray Aerosol: Sea-Salt and Organic Enrichment. *Atmos. Environ.* **2010**, *44*, 670−677.

(9) de Leeuw, G.; Andreas, E. L.; Anguelova, M. D.; Fairall, C. W.; Lewis, E. R.; O'Dowd, C.; Schulz, M.; Schwartz, S. E. Production Flux of Sea Spray Aerosol. *Rev. Geophys.* **2011**, *49*, 2001.

(10) Gantt, B.; Meskhidze, N. The Physical and Chemical Characteristics of Marine Primary Organic Aerosol: a Review. *Atmos. Chem. Phys.* **2013**, *13*, 3979−3996.

(11) Wilson, T. W.; Ladino, L. A.; Alpert, P. A.; Breckels, M. N.; Brooks, I. M.; Browse, J.; Burrows, S. M.; Carslaw, K. S.; Huffman, J. A.; Judd, C.; et al. A Marine Biogenic Source of Atmospheric Ice-Nucleating Particles. *Nature* **2015**, *525*, 234−238.

(12) O'Dowd, C. D.; de Leeuw, G. Marine Aerosol Production: a Review of the Current Knowledge. *Philos. Trans. R. Soc., A* **2007**, *365*, 1753−1774.

(13) Despres, V. R.; Huffman, J. A.; Burrows, S. M.; Hoose, C.; Safatov, A. S.; Buryak, G.; Froehlich-Nowoisky, J.; Elbert, W.; Andreae, M. O.; Poeschl, U.; et al. Primary Biological Aerosol Particles in the Atmosphere: a Review. *Tellus, Ser. B* **2012**, *64*, 15598−15655.

(14) Claeys, M.; Wang, W.; Vermeylen, R.; Kourtchev, I.; Chi, X.; Farhat, Y.; Surratt, J. D.; Gomez-Gonzalez, Y.; Sciare, J.; Maenhaut, W. Chemical Characterisation of Marine Aerosol at Amsterdam Island during the Austral Summer of 2006−2007. *J. Aerosol Sci.* **2010**, *41*, 13−22.

(15) Cavalli, F.; Facchini, M. C.; Decesari, S.; Mircea, M.; Emblico, L.; Fuzzi, S.; Ceburnis, D.; Yoon, Y. J.; O'Dowd, C. D.; Putaud, J.-P.; et al. Advances in Characterization of Size-Resolved Organic Matter in Marine Aerosol over the North Atlantic. *J. Geophys. Res.* **2004**, *109*, D24215.

(16) Middlebrook, A. M.; Murphy, D. M.; Thomson, D. S. Observations of Organic Material in Individual Marine Particles at Cape Grim during the First Aerosol Characterization Experiment (ACE 1). *J. Geophys. Res.: Atmos.* **1998**, *103*, 16475−16483.

(17) O'Dowd, C. D.; Facchini, M. C.; Cavalli, F.; Ceburnis, D.; Mircea, M.; Decesari, S.; Fuzzi, S.; Yoon, Y. J.; Putaud, J.-P. Biogenically Driven Organic Contribution to Marine Aerosol. *Nature* **2004**, *431*, 676−680.

(18) Donaldson, D. J.; Vaida, V. The Influence of Organic Films at the Air-Aqueous Boundary on Atmospheric Processes. *Chem. Rev.* **2006**, *106*, 1445−1461.

(19) Mochida, M.; Kitamori, Y.; Kawamura, K.; Nojiri, Y.; Suzuki, K. Fatty Acids in the Marine Atmosphere: Factors Governing their Concentrations and Evaluation of Organic Films on Sea-Salt Particles. *J. Geophys. Res.: Atmos.* **2002**, *107*, AAC 1-1.

DOI: 10.1021/acs.jpca.6b07792
J. Phys. Chem. A 2016, 120, 10141−10149

(20) Tervahattu, H.; Hartonen, K.; Kerminen, V.; Kupiainen, K.; Aarnio, P.; Koskentalo, T.; Tuck, A. F.; Vaida, V. New Evidence of an Organic Layer on Marine Aerosols. *J. Geophys. Res.* **2002**, *107*, 4053−4060.
(21) Yoon, Y.; Ceburnis, D.; Cavalli, F.; Jourdan, O.; Putaud, J.; Facchini, M.; Decesari, S.; Fuzzi, S.; Sellegri, K.; Jennings, S. Seasonal Characteristics of the Physicochemical Properties of North Atlantic Marine Atmospheric Aerosols. *J. Geophys. Res.* **2007**, *112*, D04206.
(22) Cochran, R. E.; Laskina, O.; Jayarathne, T.; Laskin, A.; Laskin, J.; Lin, P.; Sultana, C.; Lee, C.; Moore, K. A.; Cappa, C. D.; et al. Analysis of Organic Anionic Surfactants in Fine and Coarse Fractions of Freshly Emitted Sea Spray Aerosol. *Environ. Sci. Technol.* **2016**, *50*, 2477−2486.
(23) Tervahattu, H.; Juhanoja, J.; Kupiainen, K. Identification of an Organic Coating on Marine Aerosol Particles by TOF-SIMS. *J. Geophys. Res.* **2002**, *107*, 4319−4325.
(24) Chi, J. W.; Li, W. J.; Zhang, D. Z.; Zhang, J. C.; Lin, Y. T.; Shen, X. J.; Sun, J. Y.; Chen, J. M.; Zhang, X. Y.; Zhang, Y. M.; et al. Sea Salt Aerosols as a Reactive Surface for Inorganic and Organic Acidic Gases in the Arctic Troposphere. *Atmos. Chem. Phys.* **2015**, *15*, 11341−11353.
(25) Wise, M. E.; Semeniuk, T. A.; Bruintjes, R.; Martin, S. T.; Russell, L. M.; Buseck, P. R. Hygroscopic Behavior of NaCl-Bearing Natural Aerosol Particles Using Environmental Transmission Electron Microscopy. *J. Geophys. Res.* **2007**, *112*, D10224.
(26) Patterson, J. P.; Collins, D. B.; Michaud, J. M.; Axson, J. L.; Sultana, C. M.; Moser, T.; Dommer, A. C.; Conner, J.; Grassian, V. H.; Stokes, M. D.; et al. Sea Spray Aerosol Structure and Composition Using Cryogenic Transmission Electron Microscopy. *ACS Cent. Sci.* **2016**, *2*, 40−47.
(27) Smoydzin, L.; von Glasow, R. Do Organic Surface Films on Sea Salt Aerosols Influence Atmospheric Chemistry? - A Model Study. *Atmos. Chem. Phys.* **2007**, *7*, 5555−5567.
(28) McNeill, V. F.; Sareen, N.; Schwier, A. N. In *Atmospheric and Aerosol Chemistry*; McNeill, V. F., Ariya, P. A., Eds.; Springer Berlin Heidelberg: Berlin, Heidelberg, 2014; pp 201−259.
(29) Rouvière, A.; Ammann, M. The Effect of Fatty Acid Surfactants on the Uptake of Ozone to Aqueous Halogenide Particles. *Atmos. Chem. Phys.* **2010**, *10*, 11489−11500.
(30) Miñambres, L.; Méndez, E.; Sánchez, M. N.; Castaño, F.; Basterretxea, F. J. The Effect of Low Solubility Organic Acids on the Hygroscopicity of Sodium Halide Aerosols. *Atmos. Chem. Phys.* **2014**, *14*, 11409−11425.
(31) Finlayson-Pitts, B. J. The Tropospheric Chemistry of Sea Salt: A Molecular-Level View of the Chemistry of NaCl and NaBr. *Chem. Rev.* **2003**, *103*, 4801−4822.
(32) George, I. J.; Abbatt, J. P. D. Heterogeneous 0xidation of Atmospheric Aerosol Particles by Gas-Phase Radicals. *Nat. Chem.* **2010**, *2*, 713−722.
(33) Davies, J. F.; Miles, R. E. H.; Haddrell, A. E.; Reid, J. P. Influence of Organic Films on the Evaporation and Condensation of Water in Aerosol. *Proc. Natl. Acad. Sci. U. S. A.* **2013**, *110*, 8807−8812.
(34) Dennis-Smither, B. J.; Hanford, K. L.; Kwamena, N.-O. A.; Miles, R. E. H.; Reid, J. P. Phase, Morphology, and Hygroscopicity of Mixed Oleic Acid/Sodium Chloride/Water Aerosol Particles before and after Ozonolysis. *J. Phys. Chem. A* **2012**, *116*, 6159−6168.
(35) Ebben, C. J.; Ault, A. P.; Ruppel, M. J.; Ryder, O. S.; Bertram, T. H.; Grassian, V. H.; Prather, K. A.; Geiger, F. M. Size-Resolved Sea Spray Aerosol Particles Studied by Vibrational Sum Frequency Generation. *J. Phys. Chem. A* **2013**, *117*, 6589−6601.
(36) Rossi, M. J. Heterogeneous Reactions on Salts. *Chem. Rev.* **2003**, *103*, 4823−4882.
(37) Garland, R. M.; Wise, M. E.; Beaver, M. R.; DeWitt, H. L.; Aiken, A. C.; Jimenez, J. L.; Tolbert, M. A. Impact of Palmitic Acid Coating on the Water Uptake and Loss of Ammonium Sulfate Particles. *Atmos. Chem. Phys.* **2005**, *5*, 1951−1961.
(38) Hansson, H.-C.; Rood, M.; Koloutsou-Vakakis, S.; Hameri, K.; Orsini, D.; Wiedensohler, A. NaCl aerosol particle hygroscopicity dependence on mixing with organic compounds. *J. Atmos. Chem.* **1998**, *31*, 321−346.
(39) Robinson, C. B.; Schill, G. P.; Zarzana, K. J.; Tolbert, M. A. Impact of Organic Coating on Optical Growth of Ammonium Sulfate Particles. *Environ. Sci. Technol.* **2013**, *47*, 13339−13346.
(40) Najera, J. J.; Horn, A. B. Infrared Spectroscopic Study of the Effect of Oleic Acid on the Deliquescence Behaviour of Ammonium Sulfate Aerosol Particles. *Phys. Chem. Chem. Phys.* **2009**, *11*, 483−494.
(41) Rubasinghege, G.; Ogden, S.; Baltrusaitis, J.; Grassian, V. H. Heterogeneous Uptake and Adsorption of Gas-Phase Formic Acid on Oxide and Clay Particle Surfaces: The Roles of Surface Hydroxyl Groups and Adsorbed Water in Formic Acid Adsorption and the Impact of Formic Acid Adsorption on Water Uptake. *J. Phys. Chem. A* **2013**, *117*, 11316−11327.
(42) Sobanska, S.; Barbillat, J.; Moreau, M.; Nuns, N.; De Waele, I.; Petitprez, D.; Tobon, Y.; Brémard, C. Influence of Stearic Acid Coating of the NaCl Surface on the Reactivity with NO2 under Humidity. *Phys. Chem. Chem. Phys.* **2015**, *17*, 10963−10977.
(43) Sun, L.; Hede, T.; Tu, Y.; Leck, C.; Agren, H. Combined Effect of Glycine and Sea Salt on Aerosol Cloud Droplet Activation Predicted by Molecular Dynamics Simulations. *J. Phys. Chem. A* **2013**, *117*, 10746−10752.
(44) Takahama, S.; Russell, L. M. A molecular Dynamics Study of Water Mass Accommodation on Condensed Phase Water Coated by Fatty Acid Monolayers. *J. Geophys. Res.* **2011**, *116*, D02203.
(45) Chakraborty, P.; Zachariah, M. R. *J. Geophys. Res.* **2011**, *116*, D21205.
(46) Harmon, C. W.; Grimm, R. L.; McIntire, T. M.; Peterson, M. D.; Njegic, B.; Angel, V. M.; Alshawa, A.; Underwood, J. S.; Tobias, D. J.; Gerber, R. B.; et al. Hygroscopic Growth and Deliquescence of NaCl Nanoparticles Mixed with Surfactant SDS. *J. Phys. Chem. B* **2010**, *114*, 2435−2449.
(47) Sun, L.; Li, X.; Hede, T.; Tu, Y.; Leck, C.; Agren, H. Molecular Dynamics Simulations of the Surface Tension and Structure of Salt Solutions and Clusters. *J. Phys. Chem. B* **2012**, *116*, 3198−3204.
(48) Lin, W.; Clark, A. J.; Paesani, F. Effects of Surface Pressure on the Properties of Langmuir Monolayers and Interfacial Water at the Air-Water Interface. *Langmuir* **2015**, *31*, 2147−2156.
(49) Baoukina, S.; Tieleman, D. P. In *Biomolecular Simulations: Methods and Protocols*; Monticelli, L., Salonen, E., Eds.; Humana Press: Totowa, NJ, 2013; pp 431−444.
(50) Tang, C. Y.; Allen, H. C. Ionic Binding of Na+ versus K+ to the Carboxylic Acid Headgroup of Palmitic Acid Monolayers Studied by Vibrational Sum Frequency Generation Spectroscopy. *J. Phys. Chem. A* **2009**, *113*, 7383−7393.
(51) Van Der Spoel, D.; Lindahl, E.; Hess, B.; Groenhof, G.; Mark, A. E.; Berendsen, H. J. C. GROMACS: Fast, Flexible, and Free. *J. Comput. Chem.* **2005**, *26*, 1701−1718.
(52) Jorgensen, W. L.; Maxwell, D. S.; Tirado-Rives, J. Development and Testing of the OPLS All-Atom Force Field on Conformational Energetics and Properties of Organic Liquids. *J. Am. Chem. Soc.* **1996**, *118*, 11225−11236.
(53) Caleman, C.; van Maaren, P. J.; Hong, M.; Hub, J. S.; Costa, L. T.; van der Spoel, D. Force Field Benchmark of Organic Liquids: Density, Enthalpy of Vaporization, Heat Capacities, Surface Tension, Isothermal Compressibility, Volumetric Expansion Coefficient, and Dielectric Constant. *J. Chem. Theory Comput.* **2012**, *8*, 61−74.
(54) Plazzer, M. B.; Henry, D. J.; Yiapanis, G.; Yarovsky, I. Comparative Study of Commonly Used Molecular Dynamics Force Fields for Modeling Organic Monolayers on Water. *J. Phys. Chem. B* **2011**, *115*, 3964−3971.
(55) Prime, E. L.; Tran, D. N.; Plazzer, M.; Sunartio, D.; Leung, A. H.; Yiapanis, G.; Baoukina, S.; Yarovsky, I.; Qiao, G. G.; Solomon, D. H. Rational Design of Monolayers for Improved Water Evaporation Mitigation. *Colloids Surf., A* **2012**, *415*, 47−58.
(56) Habartova, A.; Roeselova, M.; Cwiklik, L. Investigation of Mixed Surfactant Films at Water Surface Using Molecular Dynamics Simulations. *Langmuir* **2015**, *31*, 11508−11515.
(57) Patra, M.; Karttunen, M. Systematic Comparison of Force Fields for Microscopic Simulations of NaCl in Aqueous Solutions: Diffusion,

DOI: 10.1021/acs.jpca.6b07792
J. Phys. Chem. A 2016, 120, 10141−10149

Free Energy of Hydration, and Structural Properties. *J. Comput. Chem.* **2004**, *25*, 678−689.
(58) Smith, D. E.; Dang, L. X. Computer Simulations of NaCl Association in Polarizable Water. *J. Chem. Phys.* **1994**, *100*, 3757−3766.
(59) Berendsen, H. J. C.; Grigera, J. R.; Straatsma, T. P. The Missing Term in Effective Pair Potentials. *J. Phys. Chem.* **1987**, *91*, 6269−6271.
(60) Vega, C.; de Miguel, E. Surface Tension of the Most Popular Models of Water by Using the Test-Area Simulation Method. *J. Chem. Phys.* **2007**, *126*, 154707.
(61) Verlet, L. Computer "Experiments" on Classical Fluids. I. Thermodynamical Properties of Lennard-Jones Molecules. *Phys. Rev.* **1967**, *159*, 98−103.
(62) Hess, B.; Bekker, H.; Berendsen, H. J. C.; Fraaije, J. G. E. M. LINCS: A Linear Constraint Solver for Molecular Simulations. *J. Comput. Chem.* **1997**, *18*, 1463−1472.
(63) Bussi, G.; Donadio, D.; Parrinello, M. Canonical Sampling through Velocity Rescaling. *J. Chem. Phys.* **2007**, *126*, 014101.
(64) Berendsen, H. J. C.; Postma, J. P. M.; van Gunsteren, W. F.; DiNola, A.; Haak, J. R. Molecular Dynamics with Coupling to an External Bath. *J. Chem. Phys.* **1984**, *81*, 3684−3690.
(65) Sirdeshmukh, D.; Sirdeshmukh, L.; Subhadra, K. *Alkali Halides*; Springer Series in Materials Science; Springer: Berlin Heidelberg, 2001; Vol. *49*, pp 1−14.
(66) Foster, M. C.; Ewing, G. E. Adsorption of Water on the NaCl(001) Surface. II. An Infrared Study at Ambient Temperatures. *J. Chem. Phys.* **2000**, *112*, 6817−6826.
(67) Ewing, G. E. Ambient Thin Film Water on Insulator Surfaces. *Chem. Rev.* **2006**, *106*, 1511−1526.
(68) Engkvist, O.; Stone, A. J. Adsorption of Water on the NaCl(001) Surface. III. Monte Carlo Simulations at Ambient Temperatures. *J. Chem. Phys.* **2000**, *112*, 6827−6833.
(69) Bahadur, R.; Russell, L. M. Water Uptake Coefficients and Deliquescence of NaCl Nanoparticles at Atmospheric Relative Humidities from Molecular Dynamics Simulations. *J. Chem. Phys.* **2008**, *129*, 094508.
(70) Bahadur, R.; Russell, L. M.; Alavi, S.; Martin, S. T.; Buseck, P. R. Void-Induced Dissolution in Molecular Dynamics Simulations of NaCl and Water. *J. Chem. Phys.* **2006**, *124*, 154713.
(71) Ulman, A. *An Introduction to Ultrathin Organic Films: From Langmuir-Blodgett to Self-Assembly*; Elsevier Inc., 2013.
(72) Jadhav, S. A. Self-Assembled Monolayers (SAMs) of Carboxylic Acids: an Overview. *Cent. Eur. J. Chem.* **2011**, *9*, 369−378.
(73) Donaldson, D. J.; George, C. Sea-Surface Chemistry and Its Impact on the Marine Boundary Layer. *Environ. Sci. Technol.* **2012**, *46*, 10385−10389.
(74) Cosman, L. M.; Bertram, A. K. Reactive Uptake of N2O5 on Aqueous H2SO4 Solutions Coated with 1-Component and 2-Component Monolayers. *J. Phys. Chem. A* **2008**, *112*, 4625−4635.
(75) Stemmler, K.; Vlasenko, A.; Guimbaud, C.; Ammann, M. The Effect of Fatty Acid Surfactants on the Uptake of Nitric Acid to Deliquesced NaCl Aerosol. *Atmos. Chem. Phys.* **2008**, *8*, 5127−5141.
(76) Hammerich, A. D.; Finlayson-Pitts, B. J.; Gerber, R. B. NOx Reactions on Aqueous Surfaces with Gaseous HCl: Formation of a Potential Precursor to Atmospheric Cl Atoms. *J. Phys. Chem. Lett.* **2012**, *3*, 3405−3410.
(77) Zhang, C.; Zhang, X.; Kang, L.; Wang, N.; Wang, M.; Sun, X.; Wang, W. Adsorption and Transformation Mechanism of NO2 on NaCl(100) Surface: A Density Functional Theory Study. *Sci. Total Environ.* **2015**, *524*−*525*, 195−200.
(78) Ryder, O. S.; Campbell, N. R.; Morris, H.; Forestieri, S.; Ruppel, M. J.; Cappa, C.; Tivanski, A.; Prather, K.; Bertram, T. H. Role of Organic Coatings in Regulating N2O5 Reactive Uptake to Sea Spray Aerosol. *J. Phys. Chem. A* **2015**, *119*, 11683−11692.
(79) Tsigaridis, K.; Daskalakis, N.; Kanakidou, M.; Adams, P. J.; Artaxo, P.; Bahadur, R.; Balkanski, Y.; Bauer, S. E.; Bellouin, N.; Benedetti, A.; et al. The AeroCom Evaluation and Intercomparison of Organic Aerosol in Global Models. *Atmos. Chem. Phys.* **2014**, *14*, 10845−10895.
(80) Mann, G. W.; Carslaw, K. S.; Reddington, C. L.; Pringle, K. J.; Schulz, M.; Asmi, A.; Spracklen, D. V.; Ridley, D. A.; Woodhouse, M. T.; Lee, L. A.; et al. Intercomparison and Evaluation of Global Aerosol Microphysical Properties among AeroCom Models of a Range of Complexity. *Atmos. Chem. Phys.* **2014**, *14*, 4679−4713.

DOI: 10.1021/acs.jpca.6b07792
J. Phys. Chem. A 2016, 120, 10141−10149

Bibliography

[1] J. Seinfeld and S. Pandis. *Atmospheric Chemistry and Physics: From Air Pollution to Climate Change*. John Wiley & Sons, Ltd, 1998.

[2] J. F. Kasting. "The Rise of Atmospheric Oxygen". *Science* 293 (2001), pp. 819–820. DOI: 10.1126/science.1063811.

[3] IPCC. "Summary for Policymakers. In: Climate Change 2013: The Physical Science Basis. Contribution of Working Group I to the Fifth Assessment Report of the Intergovernmental Panel on Climate Change". *Ipcc* (2013), pp. 1–29. DOI: 10.1017/CBO9781107415324.

[4] L. May. "Atomism before Dalton". *Atoms in Chemistry: From Dalton's Predecessors to Complex Atoms and Beyond*. Chap. 3, pp. 21–33. DOI: 10.1021/bk-2010-1044.ch003.

[5] I. Lagzi, R. Mészáros, G. Gelybó, and Ádám Leelőssy. *Atmospheric Chemistry*. http://ttktamop.elte.hu/sites/ttktamop.elte.hu/files/tananyagok/athmospheric_chemistry.pdf. 2013.

[6] P. A. Smithson. "IPCC, 2001: climate change 2001: the scientific basis. Contribution of Working Group 1 to the Third Assessment Report of the Intergovernmental Panel on Climate Change, edited by J. T. Houghton, Y. Ding, D. J. Griggs, M. Noguer, P. J. van der Linden, X. Dai, K. Maskell and C. A. Johnson (eds). Cambridge University Press, Cambridge, UK, and New York, USA, 2001." *International Journal of Climatology* 22 (2002), pp. 1144–1144. DOI: 10.1002/joc.763.

[7] U. Pöschl and M. Shiraiwa. "Multiphase Chemistry at the Atmosphere-Biosphere Interface Influencing Climate and Public Health in the Anthropocene." *Chemical reviews* 115 (2015), pp. 4440–4475. DOI: 10.1021/cr500487s.

[8] K.-H. Kim, E. Kabir, and S. Kabir. "A review on the human health impact of airborne particulate matter". *Environment International* 74 (2015), pp. 136 –143. DOI: http://doi.org/10.1016/j.envint.2014.10.005.

[9] J. L. Mauderly and J. C. Chow. "Health Effects of Organic Aerosols". *Inhalation Toxicology* 20 (2008), pp. 257–288. DOI: 10.1080/08958370701866008.

[10] World Health Organization. "Health Effects of Particulate Matter: Policy implications for countries in eastern Europe, Caucasus and central Asia". *Journal of the Korean Medical Association* 50 (2013), p. 20. DOI: 10.5124/jkma.2007.50.2.175.

[11] W. C. Hinds. *Aerosol technology : properties, behavior, and measurement of airborne particles*. Wiley-VCH Verlag GmbH & Co. KGaA, 1999.

[12] B. Gantt and N. Meskhidze. "The physical and chemical characteristics of marine primary organic aerosol: a review". *Atmospheric Chemistry and Physics* 13 (2013), pp. 3979–3996. DOI: 10.5194/acp-13-3979-2013.

[13] B. Gantt, M. S. Johnson, M. Crippa, A. S. H. Prévôt, and N. Meskhidze. "Implementing marine organic aerosols into the GEOS-Chem model". *Geoscientific Model Development* 8 (2015), pp. 619–629. DOI: 10.5194/gmd-8-619-2015.

[14] N. Meskhidze, M. D. Petters, K. Tsigaridis, et al. "Production mechanisms, number concentration, size distribution, chemical composition, and optical properties of sea spray aerosols". *Atmospheric Science Letters* 14 (2013), pp. 207–213. DOI: 10.1002/asl2.441.

[15] J. H. Kroll and J. H. Seinfeld. "Chemistry of secondary organic aerosol: Formation and evolution of low-volatility organics in the atmosphere". *Atmospheric Environment* 42 (2008), pp. 3593–3624. DOI: 10.1016/j.atmosenv.2008.01.003.

[16] U. Pöschl. "Atmospheric Aerosols: Composition, Transformation, Climate and Health Effects". *Angewandte Chemie International Edition* 44 (2005), pp. 7520–7540. DOI: 10.1002/anie.200501122.

[17] H. Kohler. "The nucleus in and the growth of hygroscopic droplets". *Trans. Faraday Soc.* 32 (1936), pp. 1152–1161. DOI: 10.1039/TF9363201152.

[18] M. Kampa and E. Castanas. "Human health effects of air pollution". *Environmental Pollution* 151 (2008). Proceedings of the 4th International Workshop on Biomonitoring of Atmospheric Pollution (With Emphasis on Trace Elements), pp. 362 –367. DOI: https://doi.org/10.1016/j.envpol.2007.06.012.

[19] S. Sobanska, J. Barbillat, M. Moreau, et al. "Influence of stearic acid coating of the NaCl surface on the reactivity with NO_2 under humidity". *Physical Chemistry Chemical Physics* 17 (2015), pp. 10963–10977. DOI: 10.1039/C4CP05655H.

[20] S. L. Gong, L. A. Barrie, J.-P. Blanchet, and L. Spacek. "Modeling Size-Distributed Sea Salt Aerosols in the Atmosphere: An Application Using Canadian Climate Models". *Air Pollution Modeling and Its Application XII*. Ed. by S.-E. Gryning and N. Chaumerliac. Boston, MA: Springer US, 1998, pp. 337–345. DOI: 10.1007/978-1-4757-9128-0_35.

[21] R. Jaenicke. "Abundance of Cellular Material and Proteins in the Atmosphere". *Science* 308 (2005), pp. 73–73. DOI: 10.1126/science.1106335.

[22] K. Tsigaridis, M. Krol, F. J. Dentener, et al. "Change in global aerosol composition since preindustrial times". *Atmospheric Chemistry and Physics* 6 (2006), pp. 5143–5162. DOI: 10.5194/acp-6-5143-2006.

[23] M. Andreae and D. Rosenfeld. "Aerosol–cloud–precipitation interactions. Part 1. The nature and sources of cloud-active aerosols". *Earth-Science Reviews* 89 (2008), pp. 13 –41. DOI: http://doi.org/10.1016/j.earscirev.2008.03.001.

[24] C. S. Zender, H. Bian, and D. Newman. "Mineral Dust Entrainment and Deposition (DEAD) model: Description and 1990s dust climatology". *Journal of Geophysical Research: Atmospheres* 108 (2003). 4416. DOI: 10.1029/2002JD002775.

[25] P. V. Hobbs. *Introduction to Atmospheric Chemistry*. Cambridge University Press, Sept. 2000.

[26] J. M. C. Plane. "Cosmic dust in the earth's atmosphere". *Chemical Society Reviews*. 41 (2012), pp. 6507–6518. DOI: 10.1039/C2CS35132C.

[27] C. S. Gardner, A. Z. Liu, D. R. Marsh, W. Feng, and J. M. C. Plane. "Inferring the global cosmic dust influx to the Earth's atmosphere from lidar observations of the vertical flux of mesospheric Na". *Journal of Geophysical Research: Space Physics* 119 (2014), pp. 7870–7879. DOI: 10.1002/2014JA020383.

[28] S. H. Chung and J. H. Seinfeld. "Global distribution and climate forcing of carbonaceous aerosols". *Journal of Geophysical Research* 107 (2002), p. 4407. DOI: 10.1029/2001JD001397.

[29] H. Liao, J. H. Seinfeld, P. J. Adams, and L. J. Mickley. "Global radiative forcing of coupled tropospheric ozone and aerosols in a unified general circulation model". *Journal of Geophysical Research* 109 (2004), p. D16207. DOI: 10.1029/2003JD004456.

[30] C. Tomasi and A. Lupi. "Primary and Secondary Sources of Atmospheric Aerosol". *Atmospheric Aerosols*. Wiley-VCH Verlag GmbH & Co. KGaA, 2017, pp. 1–86. DOI: 10.1002/9783527336449.ch1.

[31] C. O'Dowd, D. Ceburnis, J. Ovadnevaite, et al. "Connecting marine productivity to sea-spray via nanoscale biological processes: Phytoplankton Dance or Death Disco?" *Scientific reports* 5 (2015), p. 14883. DOI: 10.1038/srep14883.

[32] K. A. Prather, T. H. Bertram, V. H. Grassian, et al. "Bringing the ocean into the laboratory to probe the chemical complexity of sea spray aerosol." *Proceedings of the National Academy of Sciences of the United States of America* 110 (2013), pp. 7550–7555. DOI: 10.1073/pnas.1300262110.

[33] R. E. Cochran, T. Jayarathne, E. A. Stone, and V. H. Grassian. "Selectivity Across the Interface: A Test of Surface Activity in the Composition of Organic-Enriched Aerosols from Bubble Bursting". *The Journal of Physical Chemistry Letters* 7 (2016), pp. 1692–1696. DOI: 10.1021/acs.jpclett.6b00489.

[34] L. Minambres, E. Mendez, M. N. Sanchez, F. Castano, and F. J. Basterretxea. "The effect of low solubility organic acids on the hygroscopicity of sodium halide aerosols". *Atmospheric Chemistry and Physics* 14 (2014), pp. 11409–11425. DOI: 10.5194/acp-14-11409-2014.

[35] M. Mochida, Y. Kitamori, K. Kawamura, Y. Nojiri, and K. Suzuki. "Fatty acids in the marine atmosphere: Factors governing their concentrations and evaluation of organic films on sea-salt particles". *Journal of Geophysical Research: Atmospheres* 107 (2002), AAC 1–1–AAC 1–10. DOI: 10.1029/2001JD001278.

[36] V. F. McNeill, R. L. N. Yatavelli, J. A. Thornton, C. B. Stipe, and O. Landgrebe. "The heterogeneous OH oxidation of palmitic acid in single component and internally mixed aerosol particles: vaporization, secondary chemistry, and the role of particle phase". *Atmospheric Chemistry and Physics Discussions* 8 (2008), pp. 6035–6068. DOI: 10.5194/acpd-8-6035-2008.

[37] F. Raes, R. V. Dingenen, E. Vignati, et al. "Formation and cycling of aerosols in the global troposphere". *Atmospheric Environment* 34 (2000), pp. 4215–4240. DOI: 10.1016/S1352-2310(00)00239-9.

[38] T. W. Wilson, L. A. Ladino, P. A. Alpert, et al. "A marine biogenic source of atmospheric ice-nucleating particles". *Nature* 525 (2015), pp. 234–238. DOI: 10.1038/nature14986.

[39] C. Monahan, H. Vuollekoski, M. Kulmala, and C. O'Dowd. "Simulating Marine New Particle Formation and Growth Using the M7 Modal Aerosol Dynamics Modal". *Advances in Meteorology* 2010 (2010), pp. 1–9. DOI: 10.1155/2010/689763.

[40] M. Karl, C. Leck, A. Gross, and L. Pirjola. "A study of new particle formation in the marine boundary layer over the central Arctic Ocean using a flexible multicomponent aerosol dynamic model". *Tellus B* 64 (2012).

[41] X. Ma, K. von Salzen, and J. Li. "Modelling sea salt aerosol and its direct and indirect effects on climate". *Atmospheric Chemistry and Physics* 8 (2008), pp. 1311–1327. DOI: 10.5194/acp-8-1311-2008.

[42] C. Pfrang, F. Sebastiani, C. O. M. Lucas, et al. "Ozonolysis of methyl oleate monolayers at the air–water interface: oxidation kinetics, reaction products and atmospheric implications". *Physical Chemistry Chemical Physics* 16 (2014), pp. 13220–13228. DOI: 10.1039/C4CP00775A.

[43] P. Chakraborty and M. R. Zachariah. "Sticking coefficient and processing of water vapor on organic-coated nanoaerosols". *Journal of Physical Chemistry A* 112 (2008), pp. 966–972. DOI: 10.1021/jp076442f.

[44] L. Sun, X. Li, T. Hede, et al. "Molecular Dynamics Simulations of the Surface Tension and Structure of Salt Solutions and Clusters". *Journal of Physical Chemistry B* 116 (2012), pp. 3198–3204. DOI: 10.1021/jp209178s.

[45] L. Sun, T. Hede, Y. Tu, C. Leck, and H. Ågren. "Combined E ff ect of Glycine and Sea Salt on Aerosol Cloud Droplet Activation Predicted by Molecular Dynamics Simulations". *Journal of Physical Chemistry A* 117 (2013), pp. 10746–10752. DOI: 10.1021/jp407538x.

[46] S. Takahama and L. M. Russell. "A molecular dynamics study of water mass accommodation on condensed phase water coated by fatty acid monolayers". *Journal of Geophysical Research: Atmospheres* 116 (2011), pp. 1–14. DOI: 10.1029/2010JD014842.

[47] R. Chakraborty P.and Zachariah. "On the structure of organic coated water droplets: From net water attractors to oily drops". *Journal of Geophysical Research: Atmospheres* 2 (2011), p. D21205. DOI: 10.1029/2011JD015961.

[48] C. W. Harmon, R. L. Grimm, T. M. McIntire, et al. "Hygroscopic growth and deliquescence of NaCl nanoparticles mixed with surfactant SDS." *Journal of Physical Chemistry B* 114 (2010), pp. 2435–49. DOI: 10.1021/jp909661q.

[49] X. Li, T. Hede, Y. Tu, C. Leck, and H. Ågren. "Cloud droplet activation mechanisms of amino acid aerosol particles: insight from molecular dynamics simulations". *Tellus B* 65 (2013), pp. 1–13. DOI: 10.3402/tellusb.v65i0.20476.

[50] V. Loukonen, I. F. W. Kuo, M. J. McGrath, and H. Vehkamäki. "On the stability and dynamics of (sulfuric acid) (ammonia) and (sulfuric acid) (dimethylamine) clusters: A first-principles molecular dynamics investigation". *Chemical Physics* 428 (2014), pp. 164–174. DOI: 10.1016/j.chemphys.2013.11.014.

[51] C. Zhang, Y. Wang, Y. Liu, and Y. Yang. "A molecular dynamics study of water vapor nucleation in the presence of ions". *Chemical Engineering Science* 137 (2015), pp. 308–319. DOI: 10.1016/j.ces.2015.06.006.

[52] Y. J. Feng, T. Huang, C. Wang, et al. "??-Hydrogen Bonding of Aromatics on the Surface of Aerosols: Insights from Ab Initio and Molecular Dynamics Simulation". *Journal of Physical Chemistry B* 120 (2016), pp. 6667–6673. DOI: 10.1021/acs.jpcb.6b01180.

[53] B. J. Gertner and J. T. Hynes. "Molecular dynamics simulation of hydrochloric acid ionization at the surface of stratospheric ice". *Science* 271 (1996), pp. 1563–1566. DOI: Doi10.1126/Science.271.5255.1563.

[54] C. Tong, M. Blanco, W. A. Goddard, and J. H. Seinfeld. "Thermodynamic properties of multifunctional oxygenates in atmospheric aerosols from quantum mechanics and molecular dynamics: dicarboxylic acids." *Environmental science & technology* 38 (2004), pp. 3941–3949. DOI: 10.1021/es0354216.

[55] A. Morita. "Molecular dynamics study of mass accommodation of methanol at liquid-vapor interfaces of methanol/water binary solutions of various concentrations". *Chemical Physics Letters* 375 (2003), pp. 1–8. DOI: 10.1016/S0009-2614(03)00746-2.

[56] . Akihiro Morita*, M. Sugiyama, H. K. And, S. Koda‡, and D. R. Hanson. "Mass Accommodation Coefficient of Water: Molecular Dynamics Simulation and Revised Analysis of Droplet Train/Flow Reactor Experiment" (2004). DOI: 10.1021/JP030479S.

[57] A. Morita, Y. Kanaya, and J. S. Francisco. "Uptake of the HO2 radical by water: Molecular dynamcs calculations and their implications for atmospheric modeling". *Journal of Geophysical Research D: Atmospheres* 109 (2004), p. D09201. DOI: 10.1029/2003JD004240.

[58] J. Julin and I. Riipinen. "Molecular dynamics simulations of mass accommodation and evaporation on surfaces of atmospheric interest". *AIP Conference Proceedings*. Vol. 1527. 2013, pp. 437–440. DOI: 10.1063/1.4803298.

[59] J. Julin, M. Shiraiwa, R. E. H. Miles, et al. "Mass accommodation of water: Bridging the gap between molecular dynamics simulations and kinetic condensation models". *Journal of Physical Chemistry A* 117 (2013), pp. 410–420. DOI: 10.1021/jp310594e.

[60] "Theoretical studies of enzymic reactions: Dielectric, electrostatic and steric stabilization of the carbonium ion in the reaction of lysozyme". *Journal of Molecular Biology* 103 (1976), pp. 227–249. DOI: 10.1016/0022-2836(76)90311-9.

[61] H. M. Senn and W. Thiel. *QM/MM methods for biomolecular systems*. 2009. DOI: 10.1002/anie.200802019.

[62] H. Falsig, A. Gross, J. Kongsted, et al. "Uptake of phenol on aerosol particles". *Journal of Physical Chemistry A* 110 (2006), pp. 660–670. DOI: 10.1021/jp0536201.

[63] T. Hede, N. A. Murugan, J. Kongsted, C. Leck, and H. Ågren. "Simulations of light absorption of carbon particles in nanoaerosol clusters". *Journal of Physical Chemistry A* 118 (2014), pp. 1879–1886. DOI: 10.1021/jp412384j.

[64] M. T. C. Martins-Costa, J. M. Anglada, J. S. Francisco, and M. F. Ruiz-Lopez. "Reactivity of atmospherically relevant small radicals at the air-water interface". *Angewandte Chemie - International Edition* 51 (2012), pp. 5413–5417. DOI: 10.1002/anie.201200656.

[65] B. J. Alder and T. E. Wainwright. "Studies in Molecular Dynamics. I. General Method". *Journal of Chemical Physics* 31 (1959), pp. 459–466. DOI: 10.1063/1.1730376.

[66] A. Rahman. "Correlations in the Motion of Atoms in Liquid Argon". *Physical Review* 136 (1964), pp. 405–411. DOI: 10.1103/PhysRev.136.A405.

[67] N. Metropolis and S. Ulam. "The Monte Carlo Method". *Journal of the American Statistical Association* 44 (1949), pp. 335–341.

[68] N. Metropolis, A. W. Rosenbluth, M. N. Rosenbluth, A. H. Teller, and E. Teller. "Equation of State Calculations by Fast Computing Machines". *The Journal of Chemical Physics* 21 (1953), pp. 1087–1092. DOI: 10.1063/1.1699114.

[69] D. Van Der Spoel, E. Lindahl, B. Hess, et al. "GROMACS: Fast, flexible, and free". *Journal of Computational Chemistry* 26 (Dec. 2005), pp. 1701–1718. DOI: 10.1002/jcc.20291.

[70] J. Hutter, M. Iannuzzi, F. Schiffmann, and J. VandeVondele. "cp2k: atomistic simulations of condensed matter systems". *Wiley Interdisciplinary Reviews: Computational Molecular Science* 4 (2014), pp. 15–25. DOI: 10.1002/wcms.1159.

[71] E. M. Klimko. "A Uniform Operator Ergodic Theorem". *Ann. Math. Statist.* 40 (June 1969), pp. 1126–1129. DOI: 10.1214/aoms/1177697625.

[72] *Atoms In Motion - Chapter 5 - MD*. http://atomsinmotion.com/book/chapter5/md. Accessed: 28/04/2016. 2017.

[73] R. Notman and J. Anwar. "Breaching the skin barrier — Insights from molecular simulation of model membranes". *Advanced Drug Delivery Reviews* 65 (2013). Modeling the human skin barrier - Towards a better understanding of dermal absorption, pp. 237 –250. DOI: http://doi.org/10.1016/j.addr.2012.02.011.

[74] W. L. Jorgensen, D. S. Maxwell, and J. Tirado-Rives. "Development and Testing of the OPLS All-Atom Force Field on Conformational Energetics and Properties of Organic Liquids". *Journal of the American Chemical Society* 118 (1996), pp. 11225–11236. DOI: 10.1021/ja9621760.

[75] C. Caleman, P. J. Van Maaren, M. Hong, et al. "Force field benchmark of organic liquids: Density, enthalpy of vaporization, heat capacities, surface tension, isothermal compressibility, volumetric expansion coefficient, and dielectric constant". *Journal of Chemical Theory and Computation* 8 (2012), pp. 61–74. DOI: 10.1021/ct200731v.

[76] L. Verlet. "Computer "Experiments" on Classical Fluids. I. Thermodynamical Properties of Lennard-Jones Molecules". *Physical Review* 159 (1967), pp. 98–103. DOI: 10.1103/PhysRev.159.98.

[77] J.-P. Ryckaert, G. Ciccotti, and H. J. Berendsen. "Numerical integration of the cartesian equations of motion of a system with constraints: molecular dynamics of n-alkanes". *Journal of Computational Physics* 23 (1977), pp. 327 –341. DOI: http://dx.doi.org/10.1016/0021-9991(77)90098-5.

[78] N. Mark Johnson. *The ILL VASP manual - how to use VASP at the ILL*. 2005.

[79] P. P. Ewald. "Die Berechnung optischer und elektrostatischer Gitterpotentiale". *Annalen der Physik* 369 (1921), pp. 253–287. DOI: 10.1002/andp.19213690304.

[80] D. Frenkel and B. Smit. "Chapter 12 - Long-Range Interactions". *Understanding Molecular Simulation (Second Edition)*. Ed. by D. Frenkel, and B. Smit. Second Edition. San Diego: Academic Press, 2002, pp. 291 –320. DOI: http://dx.doi.org/10.1016/B978-012267351-1/50014-6.

[81] P. Gibbon and G. Sutmann. "Long-Range Interactions in Many-Particle Simulation, Quantum Simulations of Complex Many-Body Systems: From Theory to Algorithms". *Lecture Notes, J. Grotendorst, D. Marx, A. Muramatsu (Eds.), John von Neumann Institute for Computing, Jülich, NIC Series*. 2002, pp. 467–506.

[82] T. Darden, D. York, and L. Pedersen. "Particle mesh Ewald: An Nlog(N) method for Ewald sums in large systems". *The Journal of Chemical Physics* 98 (1993), pp. 10089–10092. DOI: 10.1063/1.464397.

[83] H. J. C. Berendsen, J. P. M. Postma, W. F. van Gunsteren, A. DiNola, and J. R. Haak. "Molecular dynamics with coupling to an external bath". *The Journal of Chemical Physics* 81 (1984), p. 3684. DOI: 10.1063/1.448118.

[84] A Papoulis and U. Pillai. *Probability, random variables and stochastic processes*. 4th. McGraw-Hill, Nov. 2001.

[85] H. C. Andersen. "Molecular dynamics simulations at constant pressure and/or temperature". *The Journal of Chemical Physics* 72 (1980), pp. 2384–2393. DOI: 10.1063/1.439486.

[86] B. R. Brooks, C. L. Brooks, A. D. Mackerell, et al. "CHARMM: The biomolecular simulation program". *Journal of Computational Chemistry* 30 (2009), pp. 1545–1614. DOI: 10.1002/jcc.21287.

[87] W. R. P. Scott, P. H. Hunenberger, I. G. Tironi, et al. "The GROMOS Biomolecular Simulation Program Package". *The Journal of Physical Chemistry A* 103 (1999), pp. 3596–3607. DOI: 10.1021/jp984217f.

[88] A. Szabo and N. S. Ostlund. *Modern Quantum Chemistry: Introduction to Advanced Electronic Structure Theory*. New edition. Dover Publications, 1996.

[89] M. Born and R. Oppenheimer. "Zur Quantentheorie der Molekeln". *Annalen der Physik* 389 (1927), pp. 457–484. DOI: 10.1002/andp.19273892002.

[90] J. P. Malhado, M. J. Bearpark, and J. T. Hynes. "Non-adiabatic dynamics close to conical intersections and the surface hopping perspective". *Frontiers in Chemistry* 2 (2014), p. 97. DOI: 10.3389/fchem.2014.00097.

[91] P. Hohenberg and W. Kohn. "Inhomogeneous Electron Gas". *Physical Review* 136 (1964), B864–B871. DOI: 10.1103/PhysRev.136.B864.

[92] W. Kohn and L. J. Sham. "Self-Consistent Equations Including Exchange and Correlation Effects". *Phys. Rev.* 140 (1965), A1133–A1138. DOI: 10.1103/PhysRev.140.A1133.

[93] A. D. Becke. "Density-functional thermochemistry. III. The role of exact exchange". *The Journal of Chemical Physics* 98 (1993), pp. 5648–5652. DOI: 10.1063/1.464913.

[94] P. J. Stephens, F. J. Devlin, C. F. Chabalowski, and M. J. Frisch. "Ab Initio Calculation of Vibrational Absorption and Circular Dichroism Spectra Using Density Functional Force Fields". *The Journal of Physical Chemistry* 98 (1994), pp. 11623–11627. DOI: 10.1021/j100096a001.

[95] R. Car and M. Parrinello. "Unified approach for molecular dynamics and density-functional theory". *Physical Review Letters* 55 (1985), pp. 2471–2474. DOI: 10.1103/PhysRevLett.55.2471.

[96] Dominik Marx and Jurg Huutter. *Ab Initio Molecular Dynamics: Basic Theory and Advanced Methods*. 2009, p. 579. DOI: 10.1017/CBO9781107415324.004.

[97] T. D. Kühne. "Second generation Car–Parrinello molecular dynamics". *Wiley Interdisciplinary Reviews: Computational Molecular Science* 4 (2014), pp. 391–406. DOI: 10.1002/wcms.1176.

[98] Stewart Clark. "Complex Structure in Tetrahedral Semiconductors". PhD thesis. University of Durham, 1994.

[99] L. W. Chung, W. M. C. Sameera, R. Ramozzi, et al. "The ONIOM Method and Its Applications". *Chemical Reviews* 115 (2015), pp. 5678–5796. DOI: 10.1021/cr5004419.

[100] T. Laino, F. Mohamed, A. Laio, and M. Parrinello. "An Efficient Real Space Multigrid QM/MM Electrostatic Coupling". *Journal of Chemical Theory and Computation* 1 (2005), pp. 1176–1184. DOI: 10.1021/ct050123f.

[101] R. Ciuraru, M. Ward, M. Mendez, et al. "Experimental study of the heterogeneous reactivity between atomic chlorine and palmitic acid films". *Journal of Atmospheric Chemistry* 70 (2013), pp. 341–355. DOI: 10.1007/s10874-013-9271-8.

[102] M. Cunliffe, A. Engel, S. Frka, et al. "Sea surface microlayers: A unified physicochemical and biological perspective of the air–ocean interface". *Progress in Oceanography* 109 (2013), pp. 104 –116. DOI: http://dx.doi.org/10.1016/j.pocean.2012.08.004.

[103] J. Lovric, D. Duflot, M. Monnerville, C. Toubin, and S. Briquez. "Water Induced Organization of Palmitic Acid at the Surface of a Model Sea Salt Particle: a Molecular Dynamics Study". *The Journal of Physical Chemistry A* (2016), pp. 10141–10149. DOI: 10.1021/acs.jpca.6b07792.

[104] J. J. Gooding, F. Mearns, W. Yang, and J. Liu. "Self-Assembled Monolayers into the 21st Century: Recent Advances and Applications". *Electroanalysis* 15 (2003), pp. 81–96. DOI: 10.1002/elan.200390017.

[105] V. Kaganer, H. Möhwald, and P. Dutta. "Structure and phase transitions in Langmuir monolayers". *Reviews of Modern Physics* 71 (1999), pp. 779–819. DOI: 10.1103/RevModPhys.71.779.

[106] L. Ramin and A. Jabbarzadeh. "Odd-even effects on the structure, stability, and phase transition of alkanethiol self-assembled monolayers." *Langmuir* 27 (2011), pp. 9748–9759. DOI: 10.1021/la201467b.

[107] A Patrykiejew. "Phase transitions in adsorbed layers formed on crystals of square and rectangular surface lattice". *Surface Science Reports* 37 (2000), pp. 207–344. DOI: 10.1016/S0167-5729(99)00011-4.

[108] M. Iwamoto and Z. C. Ou-Yang. "Tilting phase transition of amphiphile monolayers at the air-water interface: Physically reasoning phase portion in a phase diagram". *Journal of Chemical Physics* 117 (2002), pp. 7705–7711. DOI: 10.1063/1.1509050.

[109] Y. Ahn, J. K. Saha, G. C. Schatz, and J. Jang. "Molecular Dynamics Study of the Formation of a Self-Assembled Monolayer on Gold". *The Journal of Physical Chemistry C* 115 (2011), pp. 10668–10674. DOI: 10.1021/jp200447k.

[110] A. Ulman. *An Introduction to Ultrathin Organic Films: From Langmuir–Blodgett to Self–Assembly*. Academic Press, 2013.

[111] B. Hess, H. Bekker, H. J. C. Berendsen, and J. G.E. M. Fraaije. "LINCS: A linear constraint solver for molecular simulations". *Journal of Computational Chemistry* 18 (1997), pp. 1463–1472. DOI: 10.1002/(SICI)1096-987X(199709)18:12<1463::AID-JCC4>3.0.CO;2-H.

[112] D. Sirdeshmukh, L. Sirdeshmukh, and K. Subhadra. "Structure-Related Parameters". English. *Alkali Halides*. Vol. 49. Springer Series in Materials Science. Springer Berlin Heidelberg, 2001, pp. 1–14. DOI: 10.1007/978-3-662-04341-7_1.

[113] G. Bussi, D. Donadio, and M. Parrinello. "Canonical sampling through velocity rescaling". *The Journal of Chemical Physics* 126, 014101 (2007). DOI: http://dx.doi.org/10.1063/1.2408420.

[114] M. Patra and M. Karttunen. "Systematic Comparison of Force Fields for Microscopic Simulations of NaCl in Aqueous Solutions: Diffusion, Free Energy of Hydration, and Structural Properties". *Journal of Computational Chemistry* 25 (2004), pp. 678–689. DOI: 10.1002/jcc.10417.

[115] D. E. Smith and L. X. Dang. "Computer simulations of NaCl association in polarizable water". *The Journal of Chemical Physics* 100 (1994), pp. 3757–3766. DOI: 10.1063/1.466363.

[116] F. Schreiber. "Structure and growth of self-assembling monolayers". *Progress in Surface Science* 65 (2000), pp. 151–256. DOI: 10.1016/S0079-6816(00)00024-1.

[117] P. Rahe, M. Nimmrich, A. Nefedov, et al. "Transition of molecule orientation during adsorption of terephthalic acid on rutile TiO_2(110)". *Journal of Physical Chemistry C* 113 (2009), pp. 17471–17478. DOI: 10.1021/jp9052117.

[118] J. L. Beare-Rogers, A. Dieffenbacher, and J. V. Holm. "pac". Vol. 73. 4. 2001. Chap. Lexicon of lipid nutrition (IUPAC Technical Report), p. 685. DOI: 10.1351/pac200173040685.

[119] Y. Wang, J. G. Solano Canchaya, W. Dong, et al. "Chain-length and temperature dependence of self-assembled monolayers of alkylthiolates on Au(111) and Ag(111) surfaces". *Journal of Physical Chemistry A* 118 (2014), pp. 4138–4146. DOI: 10.1021/jp412285v.

[120] C. Zhang, Y. Wang, and H. Wang. "Interaction between water and acetic acid-sodium halide aerosol: A molecular dynamics study". *Powder Technology* (2016), pp. –. DOI: http://doi.org/10.1016/j.powtec.2016.12.082.

[121] G. E. Ewing. "Ambient thin film water on insulator surfaces". *Chemical Reviews* 106 (2006), pp. 1511–1526. DOI: 10.1021/cr040369x.

[122] WHO. "Health Aspects of Air Pollution with Particulate Matter , Ozone and Nitrogen Dioxide". *Report on a WHO Working Group Bonn, Germany 13–15 January 2003* (2003), p. 98. DOI: 10.2105/AJPH.48.7.913.

[123] B. J. Finlayson-Pitts. "The Tropospheric Chemistry of Sea Salt: A Molecular-Level View of the Chemistry of NaCl and NaBr". *Chemical Reviews* 103 (2003), pp. 4801–4822. DOI: 10.1021/cr020653t.

[124] R. B. Gerber, D Shemesh, M. E. Varner, J. Kalinowski, and B Hirshberg. "Ab Initio and Semi-empirical Molecular Dynamics Simulations of Chemical Reactions in Isolated Molecules and in Clusters". *Physical Chemistry Chemical Physics* ASAP (2014), pp. 1–37. DOI: 10.1039/C3CP55239J.

[125] W.-G. Liu and W. A. Goddard. "First Principles Study of the Role of Interconversion Between NO_2, N_2O_4, cis $ONONO_2$, and trans $ONONO_2$ in Chemical Processes". *Journal of the American Chemical Society* 134 (2012), pp. 12970–12978. DOI: 10.1021/ja300545e.

[126] C. Zhang, X. Zhang, L. Kang, et al. "Adsorption and transformation mechanism of NO_2 on NaCl(100) surface: A density functional theory study". *Science of The Total Environment* 524-525 (2015), pp. 195–200. DOI: 10.1016/j.scitotenv.2015.04.010.

[127] M. Ahmed, C. J. Apps, R. Buesnel, et al. "Adsorption of NxOy-Based Molecules on Large Water Clusters: An Experimental and Theoretical Study". *The Journal of Physical Chemistry A* 101 (1997), pp. 1254–1259. DOI: 10.1021/jp962213+.

[128] R. Kurtenbach, K. Becker, J. Gomes, et al. "Investigations of emissions and heterogeneous formation of HONO in a road traffic tunnel". *Atmospheric Environment* 35 (2001), pp. 3385–3394. DOI: 10.1016/S1352-2310(01)00138-8.

[129] G. Luo and X. Chen. "Ground-State Intermolecular Proton Transfer of N_2O_4 and H_2O: An Important Source of Atmospheric Hydroxyl Radical?" *The journal of physical chemistry letters* 3 (2012), pp. 1147–53. DOI: 10.1021/jz300336s.

[130] R. B. Gerber, M. E. Varner, A. D. Hammerich, et al. "Computational studies of atmospherically-relevant chemical reactions in water clusters and on liquid water and ice surfaces." *Accounts of chemical research* 48 (2015), pp. 399–406. DOI: 10.1021/ar500431g.

[131] G. Rubasinghege and V. H. Grassian. "Surface-catalyzed chlorine and nitrogen activation: Mechanisms for the heterogeneous formation of $ClNO$, NO, NO_2, $HONO$, and N_2O from HNO_3 and HCl on aluminum oxide particle surfaces". *Journal of Physical Chemistry A* 116 (2012), pp. 5180–5192. DOI: 10.1021/jp301488b.

[132] R. Kurtenbach, K. Becker, J. Gomes, et al. "Investigations of emissions and heterogeneous formation of HONO in a road traffic tunnel". *Atmospheric Environment* 35 (2001), pp. 3385–3394. DOI: 10.1016/S1352-2310(01)00138-8.

[133] A. D. Hammerich, B. J. Finlayson-Pitts, and R. B. Gerber. "NO x Reactions on Aqueous Surfaces with Gaseous HCl: Formation of a Potential Precursor to Atmospheric Cl Atoms". *The Journal of Physical Chemistry Letters* 3 (2012), pp. 3405–3410. DOI: 10.1021/jz3014985.

[134] Y. Miller, B. J. Finlayson-Pitts, and R. B. Gerber. "Ionization of N2O4 in contact with water: mechanism, time scales and atmospheric implications." *Journal of the American Chemical Society* 131 (2009), pp. 12180–12185. DOI: 10.1021/ja900350g.

[135] A. D. Becke. "Density-functional exchange-energy approximation with correct asymptotic behavior". *Physical Review A* 38 (1988), pp. 3098–3100. DOI: 10.1103/PhysRevA.38.3098.

[136] C. Lee, W. Yang, and R. G. Parr. "Development of the Colle-Salvetti correlation-energy formula into a functional of the electron density". *Physical Review B* 37 (1988), pp. 785–789. DOI: 10.1103/PhysRevB.37.785.

[137] S. Grimme. "Semiempirical GGA-type density functional constructed with a long-range dispersion correction". *Journal of Computational Chemistry* 27 (2006), pp. 1787–1799. DOI: 10.1002/jcc.20495.

[138] S. Grimme, J. Antony, S. Ehrlich, and H. Krieg. "A consistent and accurate ab initio parametrization of density functional dispersion correction (DFT-D) for the 94 elements H-Pu". *The Journal of Chemical Physics* 132 (2010), p. 154104. DOI: 10.1063/1.3382344.

[139] S. Goedecker, M. Teter, and J. Hutter. "Separable dual-space Gaussian pseudopotentials". *Physical Review. B* 54 (1996), pp. 1703–1710. DOI: 10.1103/PhysRevB.54.1703.

[140] J. B. Hasted. "Liquid Water: Dielectric Properties". *The Physics and Physical Chemistry of Water*. Ed. by F. Franks. Boston, MA: Springer New York, 1972, pp. 255–309. DOI: 10.1007/978-1-4684-8334-5_7.

[141] F. Martin and H. Zipse. "Charge distribution in the water molecule—A comparison of methods". *Journal of Computational Chemistry* 26 (2005), pp. 97–105. DOI: 10.1002/jcc.20157.

[142] D. Z. Gao. "Modeling of Adsorption and Atomic Force Microscopy Imaging of Molecules on Insulating Surfaces". PhD thesis. University College London, 2014.

[143] S. Scolaro. "Effects of humidity and fatty acid surfactants on the uptake of NO_2 to NaCl. Combined study of kinetics and surface analysis." PhD thesis. Université Lille 1 – Sciences et Technologies, 2009.

[144] D. F. Zhao, A. Buchholz, B. Kortner, et al. "Cloud condensation nuclei activity, droplet growth kinetics, and hygroscopicity of biogenic and anthropogenic secondary organic aerosol (SOA)". *Atmospheric Chemistry and Physics* 16 (2016), pp. 1105–1121. DOI: 10.5194/acp-16-1105-2016.

[145] J. Julin, P. M. Winkler, N. M. Donahue, P. E. Wagner, and I. Riipinen. "Near Unity Mass Accommodation Coefficient of Organic Molecules of Varying Structure". *Environmental Science & Technology* 48 (2014), pp. 12083–12089. DOI: 10.1021/es501816h.

[146] C. E. Kolb, R. A. Cox, J. P. D. Abbatt, et al. "An overview of current issues in the uptake of atmospheric trace gases by aerosols and clouds". *Atmospheric Chemistry and Physics* 10 (2010), pp. 10561–10605. DOI: 10.5194/acp-10-10561-2010.

[147] T. Bartels Rausch, V. Bergeron, J. H. E. Cartwright, et al. "Ice structures, patterns, and processes: A view across the icefields". *Reviews of Modern Physics* 84 (2012), pp. 885–944. DOI: 10.1103/RevModPhys.84.885.

[148] P. Ball. "Water as an Active Constituent in Cell Biology". *Chemical Reviews* 108 (2008), pp. 74–108. DOI: 10.1021/cr068037a.

[149] T. Anttila, A. Kiendler-Scharr, T. F. Mentel, and R. Tillmann. "Size dependent partitioning of organic material: evidence for the formation of organic coatings on aqueous aerosols". *Journal of Atmospheric Chemistry* 57 (2007), pp. 215–237. DOI: 10.1007/s10874-007-9067-9.

[150] J. A. Thornton and J. P. D. Abbatt. "N_2O_5 Reaction on Submicron Sea Salt Aerosol: Kinetics, Products, and the Effect of Surface Active Organics". *The Journal of Physical Chemistry A* 109 (2005). PMID: 16838918, pp. 10004–10012. DOI: 10.1021/jp054183t.

[151] A. Virtanen, J. Joutsensaari, T. Koop, et al. "An amorphous solid state of biogenic secondary organic aerosol particles. SI". *Nature* 467 (2010), pp. 824–7. DOI: 10.1038/nature09455.

[152] P. Papagiannakopoulos, X. Kong, E. S. Thomson, N. Markovic, and J. B. C. Pettersson. "Surface Transformations and Water Uptake on Liquid and Solid Butanol near the Melting Temperature". *Journal of Physical Chemistry C* 117 (2013), pp. 6678–6685. DOI: 10.1021/jp4003627.

[153] H. S. Ashbaugh, L. R. Pratt, M. E. Paulaitis, J. Clohecy, and T. L. Beck. "Deblurred Observation of the Molecular Structure of an Oil Water Interface". *Journal of the American Chemical Society* 127 (2005). PMID: 15740089, pp. 2808–2809. DOI: 10.1021/ja042600u.

[154] R. Vacha, M. L. Berkowitz, and P. Jungwirth. "Molecular Model of a Cell Plasma Membrane With an Asymmetric Multicomponent Composition: Water Permeation and Ion Effects". *Biophysical Journal* 96 (2009), pp. 4493 –4501. DOI: http://dx.doi.org/10.1016/j.bpj.2009.03.010.

[155] R. L. Napoleon and P. B. Moore. "Structural characterization of interfacial n-octanol and 3-octanol using molecular dynamic simulations". *Journal of Physical Chemistry B* 110 (2006), pp. 3666–3673. DOI: 10.1021/jp054933z.

[156] X. Kong, P. U. Andersson, N. Markovic, and J. B. C. Pettersson. "Environmental molecular beam studies of ice surface processes". eng. *The 12th International Conference on the Physics and Chemistry of Ice*. Ed. by Y Furukawa, G. Sazaki, T. Uchida, and N. Watanabe. Hokkaido University Press, 2011, pp. 79–88.

[157] X. Kong, E. S. Thomson, P. Papagiannakopoulos, S. M. Johansson, and J. B. C. Pettersson. "Water Accommodation on Ice and Organic Surfaces: Insights from Environmental Molecular Beam Experiments". *The Journal of Physical Chemistry B* 118 (2014), pp. 13378–13386. DOI: 10.1021/jp5044046.

[158] P. Derollez, A. Hédoux, Y. Guinet, F. Danède, and L. Paccou. "Structure determination of the crystalline phase of n-butanol by powder X-ray diffraction and study of intermolecular associations by Raman spectroscopy". *Acta Crystallographica Section B: Structural Science, Crystal Engineering and Materials* 69 (2013), pp. 195–202. DOI: 10.1107/S2052519213004843.

[159] W. Damm, A. Frontera, J. Tirado–Rives, and W. L. Jorgensen. "OPLS all-atom force field for carbohydrates". *Journal of Computational Chemistry* 18 (1997), pp. 1955–1970. DOI: 10.1002/(sici)1096-987x(199712)18:16<1955::aid-jcc1>3.0.co;2-l.

[160] S. W. Rick. "A reoptimization of the five-site water potential (TIP5P) for use with Ewald sums". *The Journal of Chemical Physics* 120 (2004), pp. 6085–6093. DOI: 10.1063/1.1652434.

[161] A. Gilde, N. Siladke, and C. P. Lawrence. "Molecular Dynamics Simulations of Water Transport through Butanol Films". *The Journal of Physical Chemistry A* 113 (2009), pp. 8586–8590. DOI: 10.1021/jp9026699.

[162] S. Fuzzi, M. O. Andreae, B. J. Huebert, et al. "Critical assessment of the current state of scientific knowledge, terminology, and research needs concerning the role of organic aerosols in the atmosphere, climate, and global change". *Atmospheric Chemistry and Physics Discussions* 5 (2005), pp. 11729–11780. DOI: 10.5194/acpd-5-11729-2005.

[163] A. P. Ault, T. L. Guasco, O. S. Ryder, et al. "Inside versus outside: Ion redistribution in nitric acid reacted sea spray aerosol particles as determined by single particle analysis". *Journal of the American Chemical Society* 135 (2013), pp. 14528–14531. DOI: 10.1021/ja407117x.